Continental Deformation at Varying Spatial and Temporal Scales

by

Mousumi Roy

B.S., Physics (1989)
Stanford University

M.S., Physics (1992)
Boston University

Submitted to the Department of Earth, Atmospheric and Planetary Sciences
in Partial Fulfillment of the Requirements for the Degree of
Doctor of Philosophy in Geophysics

at the

Massachusetts Institute of Technology

September, 1997

Signature of Author .....
Department of Earth, Atmospheric and Planetary Sciences
August 11, 1997

Certified by .....
Leigh Royden
Professor of Geology and Geophysics
Thesis Supervisor

Accepted by .....
Thomas H. Jordan
Department Head

Continental Rheology and Deformation at Varying Spatial and Temporal Scales

by

Mousumi Roy

Submitted to the Department of Earth, Atmospheric and Planetary Sciences
in Partial Fulfillment of the Requirements for the Degree of
Doctor of Philosophy in Geophysics

ABSTRACT

This thesis investigates continental deformation at many different spatial and temporal scales and at several plate-tectonic settings. Our main purpose is to understand how the continental crust behaves under applied forces, both over geologic times and over shorter time scales such as the seismic cycle. The thesis consists of separate investigations of long-term and short-term plate boundary deformation and also a two-part study investigating the interactions between deformation at these two time scales.

In the first part of the thesis we investigate the long-term flexural elastic response of the lithosphere to vertical loads due to normal faulting and extension. Our study suggests that high topography in the Stara Planina range in Central Bulgaria is probably related to flexural footwall uplift in response to Pliocene to Quaternary normal faulting in this region. In the second part we focus on small scale deformation on an individual brittle fault in the upper crust and study how frictional properties and constitutive behavior of the fault, described by laboratory-derived rate- and state-variable friction laws, govern the nucleation of earthquakes. The last part of the thesis investigates how the average rheologic properties of the crust govern deformation at a strike-slip plate boundary. In particular, we study the growth and evolution of fault networks within the upper crust over geologic times and how this process interacts with deformation at deeper crustal levels. Short time scale deformation such as sudden brittle failure on upper crustal faults is combined with long-term elastic and viscoelastic responses in the upper crust. Our results indicate that the rheology of the lower crust places strong controls on the nature and growth of fault networks at a strike-slip plate boundary.

Thesis Supervisor: Leigh Royden

Title: Professor of Geology and Geophysics

Acknowledgments

First, my advisor Wiki Royden for her continuing support, encouragement, exacting criticism, and her insistence on understanding the essential physics of a problem using analytic models. This approach has rescued me many times after spinning my wheels helplessly in numerical details! For great discussions and for sharing her scientific insights (which generally took me clear across whatever my quandary happened to be; usually along a new, straighter path). For allowing me the freedom to explore and develop my own ideas, but providing guidance whenever I needed it. I realize the leaps of faith this must have entailed, and I will always be grateful for the freedom it gave.

Chris Marone for that first eye-opening seminar on earthquake mechanics which inspired me to delve into the fineries of friction beyond static and dynamic. For the chance to work with him on an exciting project (Chapter 3) and his continuing guidance, not just in scientific matters but also in the important realm of presenting my work. Finally, for the constant stream of journal articles and references he sends to his students (return to Room 711 or die).

Roger Buck, Brad Hager, and Maria Zuber for critical comments and great discussions on the thesis, particularly Chapters 4 and 5, and for sharing their enthusiasm and interest. Jim Rice and Renata Dmowska for stimulating discussions, fun seminars, and their always-open door to students. Clark Burchfiel, Kip Hodges and CJ Northrup for patiently guiding my introduction to the complexities of real rocks, in the field and in classes. Rob van der Hilst for the chance to lecture in his class for a week and for occasional chats about careers and families. Tom Jordan for his guidance in the early stages of my work in friction, his abiding interest, and infectious enthusiasm. Peter Molnar for taking the time to discuss my early, half-baked ideas on incorporating faulting into continuous models.

Students past and present who have shared their ideas, opinions, advice, silliness, and woes: Gretchen Eckhardt, Anke Friedrich, Carrie Friedman, Jim Gaherty, Allegra Hosford, Audrey Huerta, Yu Jin, Kelsey Jordahl, Steve Karner, Pete Kaufman, Kirsten Nicolaysen, Lana Panasyuk, Carolyn Ruppel, Gunter Siddiqi, Mark Simons, Odin Smith, Paula Waschbusch, and Helen Webb. Among them, Helen made the 8th floor feel like home and Yu Jin, with his great questions, kept me on my toes.

Across many borders, my parents for their curiosity and sense of adventure which instilled in me the nomadic urge to wander into realms unknown; in their words, *Keep Walking!* Their love is an enduring fact within everything I do. My sister Srabani for unselfishly enduring me and, most of all, for teaching me what it means to have a heart of gold. Her generosity preserved the scattered fragments of my life outside the thesis.

Finally, ineffably, Dinesh. Without whom life and learning would be an incredibly lonely journey, walking dull, and the effort to express inexpressible things, pointless.

Thank you.

Table of Contents

Chapter 1

Introduction

Patterns of deformation observed at the surface within continents are considerably more complex and variable than those in oceanic settings, due to inherent complexities of lithology and structure within the continental crust. Deformation within continents occurs on a wide range of length and time scales, but to study plate boundary deformation we focus on two classes of behavior: long spatial and temporal scale distributed deformation which occurs over geologic times (>100 km, $>10^6$ yr) and short spatio-temporal scale deformation, such as associated with the earthquake cycle. The first class of deformation includes, for example, flexural responses to plate loading and large-scale viscous flow in the lower crust, whereas the second includes localized seismic and aseismic faulting and distributed transient responses to stress accumulation between earthquakes.

The complexity of continental deformation, which involves many different length and time scales, does not allow straightforward interpretation of surface deformation patterns (e.g., topography, seismicity patterns, or strain rates observed using geodetic methods) in terms of the overall rheologic structure within continents. Using geodynamic models of the continental lithosphere, we explore the relationships between surface manifestations of deformation and the rheologic structure of the lithosphere at depth. In Chapters 2 and 3, we present separate investigations of long-term (geologic) and short-term (seismic) continental deformation which are highly simplified because we focus on a particular length and time scale.

Chapter 2 is a study of large-scale lithospheric flexure, used to model the broad features of surface deformation in the Stara Planina Range in central Bulgaria. The results of our modeling, in conjunction with geologic and geomorphologic arguments, suggest that

topography in the Stara Planina is not due to Mesozoic shortening events as previously believed, but is a result of Pliocene-Quaternary flexural uplift. We show that forces on the lithosphere due to unloading on Pliocene-Quaternary normal faults to the south of the range are sufficient to cause uplift of the Stara Planina and thus give rise to present-day topography. An extremely low effective elastic thickness of the lithosphere (≈3 km) is required in this region to match observed topography, suggesting that the lithosphere beneath the Stara Planina is significantly weaker than beneath the Moesian platform to the north.

In Chapter 3 we present a model of the onset of frictional instability on faults during the pre-seismic (nucleation) phase of an earthquake. Frictional properties of brittle faults in the upper crust control the slip distributions on them and to a large extent govern the stress accumulations adjacent to the faults. We study one aspect of the slip distribution on faults, namely the amount and duration of slip prior to an earthquake, using a simple spring-slider model of a homogeneous fault. To model the frictional constitutive behavior of faults, laboratory-derived rate and state variable friction laws are used. By solving the equations of motion of the system coupled to the constitutive laws for friction, we derive an approximate definition of the onset of unstable slip. This definition allows us to identify the pre-seismic phase of motion and determine the role of friction constitutive parameters in governing the amount of pre-seismic slip.

While these studies illuminate various aspects of each class of deformation, in order to understand how the crust evolves in time, we need to include the interactions between the two classes of deformation. For example, although the broadest features of regional scale deformation may be described using a continuum model of the crust (e.g., a viscous fluid as in *Buck*, 1991 or *Royden*, 1996), long-term deformation at plate boundaries must involve the growth and evolution of large-scale brittle fault networks within the upper crust which may represent zones of significant strain localization. In particular, the evolution of

deformation must involve interactions between continuous deformation and new and old (pre-existing) zones of weakness such as faults.

Chapters 4 and 5 address these issues in an idealized model of a strike-slip plate boundary, focusing on the complexities which arise from the interaction of brittle faulting and continuous strain, and how such interactions are related to the strength profile of the crust with depth. We study the extent to which the continuum rheologic structure of the crust governs the nature and evolution of localized deformation within fault networks in the upper crust. For example, we investigate the effects of a weak lower crustal layer (which may undergo large-scale viscous flow) on the growth and dynamics of upper crustal brittle faults. First, a simple analytic model to determine the general character of the deformation is presented (Chapter 4) and second, a more detailed, numerical (finite-difference) approach (Chapter 5). In both parts a linear viscoelastic rheology is used for the crust and primarily elastic or primarily viscous behavior is specified at different crustal levels by varying the viscosity structure with depth. We represent faulting by static elastic dislocations, which are imposed when a critical stress threshold for failure (either fracture of a new fault or sliding on a pre-existing one) is exceeded. As we are interested here in the evolution of crustal deformation, we do not model mantle motions; instead deformation in both models is driven by imposed basal mantle velocities.

The main objective in Chapter 4, the analytic model, is to simplify the problem as much as possible in order to understand the coupling between deformation in the upper and lower parts of the crust. We therefore specify a fixed depth of faulting (confined to the uppermost crust) and divide the crust into two layers with different viscosities. By varying the viscosity of each layer and also the viscosity contrast between layers, we establish general controls on the width of the deformation zone at the surface and the number and spacing of faults in the upper crust. In Chapter 5 we allow variable depth of faulting, determined by stresses within the crust itself, and include the effect of far-field plate

motions by driving the model at the edges (in addition to basal velocities at the Moho). The viscosity of the crust is allowed to vary continuously with depth so that we specify a smooth transition from primarily elastic behavior in the upper crust to either primarily elastic or primarily viscous behavior in the lower crust. We study the time-evolution of deformation within the crust and the relation between surface deformation features such as episodic faulting and complex strain-rate patterns, and the deeper rheologic structure of the crust.

REFERENCES

Buck, R. W., Modes of continental lithospheric extension, *J. Geophys. Res.*, *96*, 20161-20178, 1991.

Royden, L. H., Coupling and decoupling of crust and mantle in convergent orogens: Implications or strain partitioning in the crust , *J . Geophys. Res.*, *101*, 17679-17705, 1996.

Chapter 2

Flexural Uplift of the Stara Planina Range, Central Bulgaria[1]

ABSTRACT

The Stara Planina is an east-west-trending range within the Balkan belt in central Bulgaria. This topographically high mountain range was the site of Mesozoic through early Cenozoic thrusting and convergence, and its high topography is generally thought to have resulted from crustal shortening associated with those events. However, uplift of this belt appears to be much younger than the age of thrusting and correlates instead with the age of Pliocene-Quaternary normal faulting along the southern side of the range. Flexural modeling indicates the morphology of the range is consistent with flexural uplift of footwall rocks during Pliocene-Quaternary displacement on south-dipping normal faults bounding the south side of the mountains, provided that the effective elastic plate thickness of 12 km under the Moesian platform is reduced to about 3 km under the Stara Planina. This small value of elastic plate thickness under the Stara Planina is similar to values observed in the Basin and Range Province of the western United States, and suggests that weakening of the lithosphere is due to heating of the lithosphere during extension, perhaps to the point that large-scale flow of material is possible within the lower crust. Because weakening is observed to affect the Moesian lithosphere for approximately 10 km beyond (north of) the surface expression of extension, this study suggests that processes within the uppermost mantle, such as convection, play an active role in the extension process. The results of this study also suggest that much of the topographic relief in thrust belts where convergence is accompanied by coeval extension in the upper plate (or "back arc"), such as in the Apennines, may be a flexural

---

[1] Roy, M., L. H. Royden, B. C. Burchfiel, Tz. Tzankov, and R. Nakov, Flexural uplift of the Stara Planina range, Central Bulgaria, *Basin Research*, *8*, 143-156, 1996.

response to unloading during normal faulting, rather than a direct response to crustal shortening in the thrust belt.

INTRODUCTION

Most active and recently active orogenic belts are associated with high topography (Argand, 1924). Earth scientists have generally attributed the development of these topographically high mountain belts to isostatic compensation for crustal thickening and shortening during convergence (Figure 2.1a). However, another mechanism for the creation of linear belts of high topography was recognized as early as 1950 by Vening Meinesz (1950). He pointed out that within extensional domains, topographically high mountains could be created during normal faulting by unloading and buoyancy driven flexural uplift of the footwall (Figure 2.1b). While it seems clear that the high topography in many orogenic belts is the result of isostatic compensation for crustal thickening, such as in the Andes and the Himalaya, there are others in which crustal shortening is accompanied or overprinted by extension of the overriding plate and the relative roles of shortening and extension in the creation of high topography is unclear.

The territory of Bulgaria has been greatly deformed by Mesozoic to Early Tertiary convergence and crustal thickening as part of the Alpine orogenic system, and the topographically high mountains of Bulgaria are generally supposed to be the direct result of Alpine crustal shortening (Figure 2.2). However, recent mapping within Bulgaria has shown that Miocene and younger normal faults, some with very large displacement, are present throughout much of Bulgaria (e.g. Dinter and Royden, 1993; Zagorchev, 1992; Tzankov et al., 1995) and Miocene to Recent extensional subsidence has occurred throughout much of central eastern Bulgaria.

A good example of the superposition of extensional and compressional structures occurs in the Stara Planina range within the Balkan belt in central Bulgaria. Shortening of the Stara Planina occurred during Mesozoic to Early Tertiary time, whereas extension occurred from Pliocene to Recent time and is currently active (Figure 2.2). Like much of the rest of Bulgaria, the topography of the Stara Planina range has been thought to be due to Mesozoic thrusting, and the role of extension in controlling the topography of the Stara Planina has been largely ignored. In this

paper we test the idea that most of the topographic relief within the Stara Planina may be due to young extensional deformation by examining the geometrical relationships between topography and normal faulting in the Stara Planina and the role of isostasy in creating footwall uplift during normal faulting.

GEOLOGIC SETTING

The Stara Planina, located in central Bulgaria, is an east-west trending range of mountains that is commonly thought to have developed antithetically to north-dipping subduction of the Vardar Ocean to the south (Burchfiel, 1980). North-directed thrusting occurred episodically within the Stara Planina from Triassic to early Tertiary time, and the frontal thrust faults of the mountain belt override upper Cretaceous and, in places, lower Tertiary sedimentary rocks of the Moesian platform (Boyanov et al., 1989). The Moesian Platform north of the Stara Planina forms an intermediate foreland between the north-vergent nappes of the Stara Planina and the south-vergent nappes of the South Carpathians (Figure 2.2). Along the southern margin of the Moesian foreland there is little evidence for the development of a foredeep basin adjacent to the Stara Planina. In contrast, there is a well-developed foredeep basin of middle to late Miocene age along the northern margin of the Moesian platform adjacent to the South Carpathians. The formation of this basin (referred to as the South Carpathian foredeep in following sections) was roughly coeval with the last major episode of thrusting and shortening in the South Carpathians (Sandulescu 1975, 1980; Paraschiv 1979).

To the south of the Stara Planina lies a broad zone of Miocene to Recent extension, which is approximately 150 km in width (Tzankov et al., 1995). The northern limit of this zone is a linear east-west-trending chain of Pliocene-Quaternary half-grabens situated immediately adjacent to the topographically high Stara Planina. To the north, this chain of grabens is bounded by the Stara Planina and to the south by the Sredna Gora range. In the central part of this chain, subsidence began in latest Miocene to Pliocene time as indicated by the presence of Pliocene and some upper Miocene sediments in the lower part of the graben fill (Figure 2.3 and Tzankov et al., 1995). In the eastern and western parts of the chain subsidence began in Quaternary time and Pliocene

sediments are absent. Typical thicknesses of sedimentary fill within the grabens are approximately 500-1000 m of predominantly Pliocene and Quaternary rocks (Tzankov et al., 1995). Faulting within the graben system appears to be currently active (Tzankov et al., 1995).

Along the entire length of the graben chain, the dominant extensional structures are south-dipping normal faults that bound the northern edge of the grabens. The normal-fault surfaces are well exposed in many places along the southern margin of the Stara Planina, where some are observed to dip gently southward at about 10^{o} to 20^{o} (Tzankov et al., 1995). The fault surfaces themselves are typically planar microbrecciated surfaces that parallel the hillslope at the foot of the Stara Planina, and are reminiscent of the microbrecciated surfaces observed on low-angle normal faults within the Basin and Range Province (e.g. Wernicke and Axen, 1988). Geological relations on the south side of the Stara Planina indicate that in places south-dipping normal faults are exposed for considerable distances up the southern slope of the mountains (Figure 2.3 and Tzankov et al., 1996). This observation strongly suggests that the southern slope of the Stara Planina represents the exhumed, partially eroded footwall of the graben-forming normal faults.

If this interpretation is correct, the topographic relief associated with the Stara Planina is coeval with the initiation of normal faulting along the south side of the mountains, indicating that uplift of the Stara Planina is of Pliocene-Quaternary age. Thus, the topography in the Stara Planina would be primarily due to footwall uplift as a result of young normal faulting rather than to Mesozoic thrusting. In the following sections we examine the topographic data in the Stara Planina to determine whether the geometry of the range is consistent with the morphology of a flexurally uplifted footwall.

Topography in the Stara Planina

North-south topographic profiles through the Stara Planina show a pronounced asymmetry (Figure 2.4a). The southern slope of the mountains is relatively steep with a horizontal distance between the bottom of the slope and the peaks of about 15 km. The northern slope of the mountains is relatively gentle with a horizontal distance between the bottom of the slope and the peaks of about 100 km. This morphology is reminiscent of that produced by footwall uplift

during normal faulting (Vening-Meinesz, 1950; Wernicke and Axen, 1988) and suggests that the northern flank of the Stara Planina represents an originally horizontal to sub-horizontal surface uplifted by flexural unloading during Pliocene-Quaternary normal faulting on the southern side of the range. A coarsely contoured topographic map of the Stara Planina (Figure 2.5) shows that the northern slope of the Stara Planina is a nearly planar surface gently warped around an east-trending axis, consistent with the interpretation that this surface has been flexurally uplifted to its present position.

The northern slope of the Stara Planina consists of nappes containing folded Mesozoic and early Cenozoic sedimentary cover of the Moesian platform (Figure 2.4b). Because of the absence of late Cenozoic rocks on this slope, we do not have precise constraints on the timing of uplift of this surface. However, its grossly planar morphology, coupled with deep incision by young rivers, suggests that uplift has been very recent. In addition, the steep valley profile of the Iskar River, which flows northward across the highest part of the western Stara Planina, strongly suggests that incision of this river is of a young age. Because downcutting of the river must have kept pace with uplift of the mountains, the uplift must also be of a comparably young age.

The absence of Upper Tertiary and Quaternary rocks on the northern slope of the Stara Planina makes it difficult to constrain the pre-uplift elevation of this surface. However, north of the Stara Planina sedimentary facies of the Moesian platform indicate that this region was covered by a broad deltaic to fluvial platform in Pliocene-Quaternary time (Steininger et al., 1985). At the beginning of Pliocene time much of the region was covered by shallow waters of the Paratethys Sea, but by the end of Pliocene time the entire region became emergent and sedimentation continued with fluvial deposition. Thus the region north of the Stara Planina appears to have been a broad, sub-horizontal plain with an initial elevation near that of modern sea level throughout Pliocene-Quaternary time.

Taken together, the arguments presented in this section strongly suggest that the present topographic expression of the Stara Planina is the result of flexural unloading of footwall rocks during normal faulting on the south side of the mountains. In addition, the data indicate that the uplift of the mountains to their present topographic elevation is of Pliocene-Quaternary age. If this

interpretation is correct, then the topographic mountains of the Stara Planina have little relationship to the older Mesozoic and Early Tertiary shortening events within the orogenic belt (except insofar as older structures may have localized the position of younger normal faults). The topography of the mountain belt can therefore be almost entirely characterized as the result of extension and flexural uplift. In the following sections we test the feasibility of this hypothesis through flexural analysis of surface slopes on the north side of the Stara Planina.

TOPOGRAPHY, GRAVITY AND DEFLECTION DATA

Topographic data in Bulgaria were obtained from a 1:500,000 scale topographic map contoured at 50 m intervals for elevations less than 200 m, 100 m intervals for elevations less than 1000 m and 200 m intervals elsewhere (Stoyanova, 1986). Topographic data in Romania were obtained from the Digital Bathymetric Data Base 5 (DBDB5) topographic data set (Defense Mapping Agency). (A comparison of DBDB5 data from Bulgaria with a smoothed version of topography from Stoyanova (1986) shows good agreement.) Topographic profiles were generated by averaging data over a 40 km wide swath centered on each profile (Figure 2.6). All profiles were smoothed using a 5-point moving window average (data spacing is roughly 2 km in Bulgaria and 10 km in Romania). Gravity profiles in Bulgaria were obtained from unpublished data; no gravity data were available for Romania (Figure 2.7).

For the following analyses, quantitative estimates of deflection are needed for two different time periods. Deflection data are needed to constrain the total flexural deflection of the Moesian platform, which can be approximated as the end-Cretaceous to Recent vertical motion of the platform, and to constrain the the Quaternary deflection of the platform. Because Cretaceous sedimentary rocks consist of platformal deposits (mainly platform carbonates), the Moesian platform must have been near sea level throughout Cretaceous time. Thus the total flexural deflection of the Moesian platform can be defined as the current depth (or elevation) of the top of the Cretaceous section.

On the north side of the Moesian platform, beneath the South Carpathian foredeep, the total flexural deflection is given by the depth to the base of the Neogene, where Neogene rocks sit

unconformably on Mesozoic platform carbonates (Paraschiv, 1979). On the south side of the Moesian platform, immediately north of the thrust sheets of the Stara Planina, Upper Cretaceous platform carbonates are exposed at the surface where they are overthrust from the south by nappes of the Stara Planina (probably in Early Tertiary time, Figure 2.4b). Thus the total (end-Cretaceous to Recent) deflection at this point can be approximated as its modern elevation, approximately 100 m above sea level. (Although there is older platform subsidence of the Moesian foreland, there is no evidence for older flexural subsidence or for the development of a southward deepening foredeep basin of Cretaceous or early Cenozoic age adjacent to the Stara Planina.)

Throughout most of Pliocene-Quaternary time, the surface elevation of the Moesian platform was near and slightly above sea level, based on the depositional environment of Pliocene-Quaternary sedimentary rocks (see preceding section). Thus we assume in earliest Quaternary time this surface was horizontal to subhorizontal and slightly above sea level. Quaternary deflection can then be defined as the present elevation of the base Quaternary or, as Quaternary sediments are everywhere thin, as the present surface elevation of the platform.

On the north slope of the Stara Planina, Pliocene-Quaternary rocks are absent. In our analysis we assume that at the beginning of Quaternary time this surface was planar and horizontal, and had the same elevation as the rest of the Moesian platform to the north. Quaternary deflection of the Stara Planina is thus defined by the current elevation of the northern Stara Planina, with several possible adjustments due to minor short wavelength irregularities in topography. For example, at the northern edge of the Stara Planina river channels and associated topographic depressions trend approximately east-west, parallel to the mountains. If these east-trending topographic features primarily represent pre-existing topography with little erosion in the river channels, then the elevation of the river valleys should give the best estimate of the vertical deflection of the underlying lithosphere. Alternatively, if these east-west trending topographic features primarily represent young downcutting of the river valleys, then the elevation of the ridge tops should give the best estimate of the vertical deflection of the underlying lithosphere.

PLIOCENE-QUATERNARY FLEXURE OF A UNIFORM RIGIDITY PLATE

If the northern slope of the Stara Planina is formed by flexural uplift of an originally horizontal to sub-horizontal surface, then the modern topography of the northern slope and of regions north of the Stara Planina should be a measure of the flexural bending of the underlying lithosphere. In particular, the vertical deflection of the surface from an originally horizontal position to the warped, slightly eroded, and locally incised surface defined by modern topography should reflect the flexural response to unloading of the underlying lithosphere by normal faulting on the south side of the Stara Planina.

In our analysis we first test whether this modern topography is consistent with deflection of a uniformly strong Moesian lithosphere. We use the method of Kruse and Royden (1994) for flexure of an elastic plate to obtain the best flexural fit to specified topography and deflection (and gravity) data. We assume that the effective plate end is located at the crest of the Stara Planina and solve for the flexural rigidity of the Moesian lithosphere, the initial surface elevation of the Moesian plate (constrained to be above sea level), and the bending moment and shear stress applied to the plate end.

The flexural rigidities that provide the best fits to topography on profiles A and B from the western Stara Planina correspond to effective elastic plate thicknesses of T_e=20 and 10 km, respectively (Figure 2.8 and Table 2.1). In the rest of this paper, we will refer interchangeably to the terms "flexural rigidity", D, and "effective elastic plate thickness", T_e, where we have used the value of $E = 8.1\times10^{10}$ Pa for Young's modulus and $\nu = 0.25$ for Poisson's ratio. In our opinion, neither of these fits are acceptable because they underestimate the slope at the crest of the range and misfit the northern half of the profiles. If a subset of the topographic data is used to constrain the plate flexure (using only ridge tops or only valley bottoms), the fit does not improve substantially. Thus profiles A and B cannot be adequately fit by flexure of a uniformly strong plate. On the other hand, topographic data on profiles D and E from the eastern Stara Planina are adequately fit by flexure of a uniformly strong plate (best fitting T_e=30 km on both profiles). However, because the lithosphere appears to be only gently flexed along these profiles, the plate strength is not very well constrained and a broad range of plate strengths provide adequate fits.

The best fitting initial elevation of the pre-uplift topographic surface (or initial water depth) is between 40 and 120 m above modern sea level. Although the initial water depths for profiles A and B are quite different (40 m for profile A and 120 m for profile B), these numbers may not be meaningful estimates of the initial elevation along these profiles because of the poor fits to topographic data. Along profiles D and E however, the initial water depths obtained are approximately 100 m for both profiles. This elevation is consistent with the expected elevation of a broad, sub-horizontal deltaic platform near sea level. In addition it is also consistent with the average present-day elevation of Moesian platform (50-150 m) in the vicinity of the Danube river floodplain north of the Stara Planina.

We conclude that if the topography on the northern slope of the Stara Planina is the result of flexure of the underlying lithosphere, then the strength of the lithosphere changes from north to south, at least on profiles A and B. In particular, the best fitting models for profiles A and B in Figure 2.8 have lower curvature than indicated by the topographic data for x =0-25 km and have higher curvature than indicated by the topographic data for x =25-150 km. This suggests that the flexural strength in the southernmost parts of profiles A and B is significantly lower than the flexural strength of the rest of the Moesian platform. In the next section we examine the effect of assuming that the strength of the Moesian lithosphere may be significantly lower beneath the southernmost parts of profiles A-E than on the northern and central parts of these profiles.

FLEXURE OF A TWO-RIGIDITY PLATE

In this section we treat the Moesian lithosphere as a continuous elastic sheet with two regions of different strength. Within each region the flexural rigidity is uniform. Provided that the width of the transition zone between these two regions is narrow compared to the flexural wavelength(s) of the lithosphere, it can be approximated as a zone of zero width. In this approximation the transition zone will be a discrete point on each of profiles A-E. At the boundary between the two regions the shear stress, bending moment, slope and deflection are constrained to be continuous. Thus three variables determine the strength distribution on each profile (the flexural rigidities of the northern and southern regions, and the lateral position of the transition point).

We first make an independent estimate of the flexural rigidity of the northern zone, which probably composes most of the Moesian platform. Then, after determining the strength of the northern zone, we need to solve only for the strength of the southernmost part of the Moesian platform and the location of the transition between the regions of differing strengths from the Quaternary deflection data.

How can we estimate the flexural rigidity of the northern Moesian platform? Flexure in the central and northern regions of the Moesian platform should be determined primarily by the flexural rigidity of the underlying lithosphere. Provided that the zone of significantly weaker lithosphere is confined to the southernmost portion of the Moesian platform (x=0-25 km? on profiles A and B), then the flexural rigidity of this weak zone will not greatly influence the flexure of the central and northern parts of the Moesian platform. Although the central and northern parts of the Moesian platform were not greatly flexed during Quaternary time (Figure 2.8), they show significant Mesozoic through Quaternary flexure (Figures 2.4b and 2.7). This occurred in response to Mesozoic to Early Tertiary overthrusting along the southern margin of the platform and Miocene overthrusting along the northern margin of the platform (see section on geologic setting). (Most of the older subsidence of the Moesian platform appears to be regional, probably due to thermal cooling of the lithosphere, and not flexural in origin.) We can therefore use the total (Mesozoic to Quaternary) flexural deflection of the central and northern Moesian lithosphere to estimate the flexural rigidity of the northern part of the platform.

Total (Mesozoic to Recent) Flexure of the Moesian Platform

In the northern part of the Moesian platform, the depth to the base of the South Carpathian foredeep (base Miocene) is a measure of the total flexural deflection of the plate. In the central part of the Moesian platform, the deflection of the lithosphere can be constrained to be zero immediately north of the thrust sheets of the Stara Planina ($x \approx$60 km). In the central to southern part of the Moesian platform the flexure can be constrained by gravity data (although gravity data from the southernmost portion of the platform may be affected by the zone of weaker lithosphere).

In analyzing the total deflection of the central and northern Moesian platform, we assume that the flexural rigidity of the lithosphere is uniform in this region and that the effective plate ends are located at the topographic crest of the Stara Planina in the south and at the deepest part of the South Carpathian foredeep basin in the north (x=0 and 220 km on Figure 2.9). The flexural deflection at the southern plate end is not tightly constrained (see discussion above) but must be consistent with the deflection of the central and northern parts of the Moesian platform, and with the gravity data. The best fits to the deflection and gravity data are obtained with flexural rigidities corresponding to T_e =12 and 20 km (Figure 2.9). The flexural profiles for T_e≈20 km are unable to match the condition that the deflection be approximately zero immediately north of the thrust sheets of the Stara Planina (x ≈60 km). Thus the best fitting effective elastic thickness which is also consistent with the deflection of the central Moesian platform is T_e=12 km (parameters are listed in Table 2.2). The flexural rigidity corresponding to this fit is D =1.24×10^{22} Nm.

Pliocene-Quaternary Flexure in the Stara Planina

The total flexural deflection of a plate with position-dependent flexural rigidity is governed by the simplified equation (in one dimension)

$$\frac{d^2}{dx^2}\left[D(x)\frac{d^2 w_i(x)}{dx^2}\right] + \Delta\rho g w_i(x) = t(x)\rho_c g \qquad (2.1)$$

where D is the flexural rigidity, $w(x)$ is the deflection, $\Delta\rho$ is the density contrast responsible for the restoring force and $t(x)$ is the distributed (topographic) load on the plate. Under the assumption that the Moesian lithosphere consists of two regions of uniform rigidity, we can divide a north-south profile though the Moesian platform into a northern region corresponding to the part of the plate between x=x_t and x= ∞ and a southern region between x=0 and x=x_t where x_t is the location of the transition point. The solutions for the deflection in these two regions, $w_{south}(x)$ and $w_{north}(x)$, can be written as:

$$w_{south}(x) = a_1\cos\left(\frac{x}{\alpha_{south}}\right)\exp\left(-\frac{x}{\alpha_{south}}\right) + b_1\sin\left(\frac{x}{\alpha_{south}}\right)\exp\left(-\frac{x}{\alpha_{south}}\right) +$$

$$+c_1\cos\left(\frac{x_t-x}{\alpha_{south}}\right)\exp\left(-\frac{x_t-x}{\alpha_{south}}\right) + d_1\sin\left(\frac{x_t-x}{\alpha_{south}}\right)\exp\left(-\frac{x_t-x}{\alpha_{south}}\right) + w_o \qquad (2.2)$$

and

$$w_{north}(x) = a_2\cos\left(\frac{x-x_t}{\alpha_{north}}\right)\exp\left(-\frac{x-x_t}{\alpha_{north}}\right) + b_2\sin\left(\frac{x-x_t}{\alpha_{north}}\right)\exp\left(-\frac{x-x_t}{\alpha_{north}}\right) + w_o \qquad (2.3)$$

where w_o is the initial water depth, assumed to be uniform for the whole plate. The six coefficients a_1, a_2, b_1, b_2, c_1, and d_1 are related by matching four boundary conditions at $x = x_t$, (the continuity of deflection, slope, bending moment and vertical shear stress), leaving only two independent coefficients to determine the best fitting plate flexure. For a given value of x_t, we solve for the best fitting flexural profile using a modified version of the method outlined in Kruse and Royden (1994), where the flexural rigidity of the north-central Moesian platform is constrained to be $D_{north} = 1.24\times10^{22}$ Nm ($Te_{north} = 12$ km), and the coefficients a,b,c and d are constrained by matching boundary conditions at $x = x_t$ and solving for the bending moment and vertical shear force at $x=0$. For each profile, we consider a range of transition points to determine the best fitting value of x_t.

Fits to profiles A and B using an elastic plate with two rigidities are significantly improved over those obtained using a plate with uniform rigidity (compare Figures 2.10 and 2.11 to Figure 2.8). Topographic slopes near the highest part of the western Stara Planina are matched well using a lower flexural rigidity in the southernmost part of the Moesian platform and the fit to the topography of the flatter central and northern parts of the Moesian platform is also much improved. The best fitting flexural rigidity in the southern region of both profiles A and B is $D_{south} = 1.94\times10^{20}$ Nm (corresponding to $Te_{south} = 3$ km) and the best fitting value for x_t for both profiles is 10 km (parameters listed in Table 2.3). The flexural fits obtained for transition points x_t >20 km are not significantly better than those obtained with a uniform rigidity plate. In particular, the best fitting range of transition point locations is about 7 km < x_t < 12 km for both profiles A

and B. The initial topographic elevation obtained for both profiles is about 40 m and is in good agreement with the constraints on the pre-uplift elevation of the Moesian platform (see previous section).

In order to investigate the effects of pre-existing topography and erosion, we use a subset of the topographic data, either the tops of ridges only (Figure 2.12) or the bottoms of valleys only (Figure 2.13), to constrain the flexure of the lithosphere. The best fitting parameters using these data sets are in the range Te_{south} = 3-4 km for both profiles A and B, and $x_t \approx 10$ km for profile A and $x_t \approx 10$-12 km for profile B. These parameters are in agreement with those found using the full data sets.

In the eastern parts of the range, a two-rigidity elastic plate model does not provide significant improvements to the flexural fits to profiles D and E. For a wide range of transition points the best fitting value of the flexural rigidity in the southern part of the Moesian platform is approximately equal to that in the central and northern parts. These results suggest that the zone of lower flexural rigidity in the southernmost part of the Moesian platform underlies the western Stara Planina and does not extend significantly to the east.

Normal-Fault Geometry and Crustal Thinning

The analysis above suggests that modern topography in the Stara Planina is consistent with flexural footwall uplift due to Pliocene-Quaternary unloading on normal-faults to the south of the mountains, and that it is not the direct result of crustal shortening across the mountain belt. Using the results above, we calculate the buoyancy forces required to drive the observed flexural uplift, and therefore estimate the amount of mass removed by extension.

Figure 2.14a illustrates how crustal thinning occurs above a normal-fault as a result of material removed during normal motion on the fault. If isostatic uplift of the footwall is neglected, the resulting geometry is that shown in Figure 2.14a. When isostatic uplift of the footwall is included, the resulting geometry is that shown in Figure 2.14c, where the volume of material removed during normal faulting is indicated by the shaded region. In Figure 2.14c,b, we estimate the geometry and volume of the material removed during normal faulting in the region south of the

Stara Planina, by solving equation (2.1) in this region for an effective elastic plate thickness of T_e=3 km. The boundary conditions applied are that the deflection, $w(x)$, and the horizontal gradient of deflection, dw/dx, at the crest of the Stara Planina match those computed for the deflection on the north side of the Stara Planina in the preceding section (and that w goes to zero far south of the Stara Planina). The total material removed during normal faulting is then the difference between the deflection computed on the south side of the Stara Planina and the observed topography, as shown in Figure 2.14b,c.

The results of this computation indicate that flexural uplift of the north side of the Stara Planina is consistent with thinning of the hangingwall, during extension, over a distance of several tens of kilometers south of the Stara Planina, with a maximum thinning of approximately 5 km (and a maximum crustal thinning of about 15%). This is small compared to the large magnitudes of unroofing observed in some core complexes in the Basin and Range Province (e.g. Wernicke and Axen, 1988, Block and Royden, 1990), and agrees well with the apparently shallow levels of exposure south of the Stara Planina. It is also of note that the deflection shown in Figure 2.14c for the south side of the Stara Planina yields a vertical shear stress at the crest of the range of 1.3×10^{11} Nm^{-1}. This value agrees well with the vertical shear stresses computed at the crest of the range for flexure of the region north of the Stara Planina: 2×10^{11} Nm^{-1} for Profile A and 1×10^{11} Nm^{-1} for Profile B.

Figure 2.14b shows the reconstructed geometry of the normal-fault system on the south side of the Stara Planina prior to movement on the normal-fault. Near the surface the geometry of the incipient normal-fault can be estimated reasonable well because it is assumed to coincide with the south slope of the Stara Planina and the northern margin of the Quaternary grabens. This indicates an initial dip for this part of the fault of about 20°. Below about 5 km depth the fault geometry is unconstrained, except that it must be deeper than the base of the material removed during faulting and probably flattens with depth in a listric geometry (Tzankov et al., 1995).

DISCUSSION AND CONCLUSIONS

The modern topography of the Mesozoic to early Tertiary thrust belt of the Stara Planina in Bulgaria appears to be almost entirely due to post-Miocene extensional processes. Because shortening and extensional events are temporally separated within the Stara Planina, the role of young normal faulting in the development of high topography can be clearly distinguished from the role of older convergent deformation in this region. The flexural modelling presented in this paper suggests that much of the morphology and modern topographic relief within the Stara Planina is the result of buoyancy-driven footwall uplift in response to (Neogene-Quaternary) normal faulting to the south of the range.

The Stara Planina, Sredna Gora and the topographically low sub-Balkan graben system are the northernmost elements of a broad Neogene extensional system that comprises much of southern Bulgaria and includes the Thracian Basin. The analysis presented here suggests that the modern topographic relief of much of this region could be the result of Neogene-Quaternary extension. For example, the topographically high region of the Rhodope "massif" of southern Bulgaria and northern Greece is bounded by Neogene (and older) normal faults that dip away from Rhodope, so that the uplifted regions lie in the footwalls of these young normal-faults. We suggest that, similar to the Stara Planina, the Rhodope "massif" has been uplifted by flexural unloading during normal faulting (see also Dinter and Royden, 1993). Other morphologic features related to young normal faulting probably include the Sredna Gora, which in our interpretation represent tilted and rotated blocks contained within the hangingwall of the normal fault system present on the south side of the Stara Planina.

Heat flow measurements within the Thracian Basin and the sub-Balkan graben system show that this extended region is the site of high surface heat flow, indicating that surface extension is related to regional extension and heating within the mantle. It is interesting that surface heat flow values generally decrease northward across the Stara Planina, and that the Stara Planina separate the zone of elevated heat flow to the south from regions of lower heat flow to the north (Cermak et al., 1979; Velinov and Boyadjieva, 1981; Velinov, 1986). This suggests that the northern limit of

heating within the lithosphere is approximately coincident with the northern limit of surface extension.

The flexural rigidity of the lithosphere beneath the Stara Planina is probably also related to the thermal structure beneath the northern edge of this extensional region. In particular, the effective elastic thickness of the Moesian plate changes from Te_{north}=12 km in the central and northern parts of the Moesian platform to about Te_{south}=3 km near the topographic crest of the central Stara Planina. The 3 km value of T_e obtained for the western Stara Planina is similar to that obtained for the Basin and Range Province of the western United States, and suggests that the Moesian lithosphere beneath the Stara Planina is sufficiently hot to allow for large-scale ductile flow within the lower crust (Block and Royden, 1990, Kaufman and Royden, 1994). We propose that the part of the Moesian lithosphere underlying the Stara Planina (at least in the central part of the range) was greatly weakened during post-Miocene extension, and that the Moesian lithosphere was probably uniformly strong prior to this event.

The flexural modeling presented in this paper indicates that the northern limit of the zone of weak lithosphere lies approximately 10 km north of the crest of the Stara Planina. This is also 10 km north of the surface exposure of major normal faults and probably at least several tens of kilometers north of where the south-dipping normal faults penetrate to lower crustal or upper mantle depths (see Tzankov et al., 1995, Figure 10). This suggests that heating and weakening of mantle and lower crustal lithosphere extends significantly beyond (north of) the region of crustal extension. It is highly unlikely that this is due to lateral diffusion of heat from beneath the extended region because the characteristic time for diffusion across a distance of 30 km is about 10 my, significantly greater than the age of initiation of extension in the sub-Balkan graben system. In addition, the amount of heating needed to reduce the effective plate thickness from 12 to 3 km is probably too large to be due to lateral diffusion over these distances. One possibility that is consistent with the observations is that the lithosphere adjacent to the zone of upper crustal extension has been heated and weakened by active processes (e.g. convection) within the uppermost mantle beneath and adjacent to the region of crustal extension (see, for example, Buck,

1986). If this hypothesis is correct, then it indicates that the mantle must play a very active role in the extension process in Bulgaria.

The idea that the high topography observed within thrust belts with back-arc extension might be due primarily to extensional deformation behind the thrust belt is radically different from traditional notions about the development of high topography within thrust belts. In the Stara Planina, the temporal separation between younger extensional and older shortening events allowed us to determine the role of extension in the development of high topography in this region. However, in mountain belts in which crustal shortening is accompanied by coeval extension of the overriding plate immediately adjacent to the zone of thrusting (Figure 2.1d), the role of extension in generating high topography is more difficult to isolate. Our results suggest that in such orogenic belts extension and flexural unloading of footwall rocks during normal faulting may be responsible for a significant portion of the topographic relief.

For example, within the Apennines the spatial relationship between normal faulting and the locus of high topography is nearly identical to that observed within the Stara Planina, and significant normal faulting begins immediately behind the topographic crest of the range (Bally et al., 1986, 1988). This suggests the possibility that uplift of the topographically high regions of the Apennines may be controlled in large part by extensional unloading of the footwall of normal faults within the extensional region, rather than to crustal shortening and thickening beneath the orogen. Other regions of high topography that are commonly supposed to be due to crustal shortening, but that we believe may be partially due to footwall uplift during normal faulting, include the Olympos region of northern Greece and mountains of the East Carpathian orogen.

ACKNOWLEDGEMENTS

This work is part of a cooperative project between the Geological Institute of the Bulgarian Academy of Sciences and M. I. T. It was supported by both sides. Support was provided by the Geological Institute and by National Academy of Science, Exchange Program for Eastern Europe, and a grant from the International Division of the National Science Foundation grant INT 9216217 awarded to B. C. Burchfiel and L. H. Royden. Part of the work on this project was completed at California Institute of Technology from 1991-1992 by L. H. Royden while supported by a Visiting Fellowship for Women from the National Science Foundation.

REFERENCES

Argand, E., 1924, La tectonique de l'Asie, Proc. 13th Int. Geol. Congr. Brussels, 7, 171-372.

Bally, A. W., L. Burbi, J. C. Cooper and R. Ghelardone, 1986, La tettonica di scollamento dell'Appennino Centrale, paper presented at 73rd National Congress of Geology of Central Italy, Rome, Sept. 30 to Oct. 4, 1986.

Bally, A. W., L. Burbi, C. Cooper and R. Ghelardone, 1988, Balanced sections and seismic reflection profiles across the central Apennines, Memorie della Societa Geologica Italiana, 257-310.

Block L. and L. H. Royden, 1990, Core complex geometries and regional scale flow in the lower crust, Tectonics, 9, no. 4, 557-567.

Boyanov I., Ch. Dabovski, P. Gocev, A. Charkovske, V. Kostadinov, Tz. Tzankov, I. Zagorcev, 1989, A new view of the Alpine tectonic evolution of Bulgaria, Geol. Rhodopica, 1, 107-121.

Buck, R. W., 1986, Small-slace convection induced by passive rifting: the cause for uplift of rift shoulders, Earth and Planetary Science Letters, 77, 362-372.

Burchfiel, B. C., 1980, Geology of Romania, GSA Special Paper.

Cermak, V. and L. Rybach, 1979, (eds.) Terrestrial heat flow in Europe, Scientific report - Inter-union Commision on Geodynamics, No. 58, Springer-Verlag.

Dinter, D. A., and L. H. Royden, 1993, Late Cenozoic extension in northeastern Greece: Strymon Valley detachment and Rhodope metamorphic core complex, Geology, 21, 45-48.

Kaufman P. S. and L. H. Royden, 1994, Lower crustal flow in an extensional setting: Constraints from the Halloran Hills region, eastern Mojave Desert, California, Journal of Geophysical Research, 99, 15,723-15,739.

Kruse, S. E. and L. H. Royden, 1994, Bending and unbending of an elastic lithosphere: The Cenozoic history of the Apennine and Dinaride foredeep basins, Tectonics, 13, 278-302.

Paraschiv, D., 1979, Romanian oil and gas fields, Geophysical Prospecting and Exploration, Series A, No. 13, 1-382.

Sandulescu, M., 1975, Essai de synthese structurale des Carpathes, Bull. Dov. Géol. Fr., Parin, XVII, n.3, 299-358.

Sandulescu, M., 1980, Analyse géotectonique des chaines alpines situées autour de la Mer Noire occidentale, Ann. Inst. Geol. Geophys., Bucuresti, LVI, 5-54.

Steininger, F. F., J. Senes, K. Kleemann, F. Rögl, 1985, Neogene Mediterranean Tethys and Paratethys, Vol. 1, Institute of Paleontology, University of Vienna, Vienna, Austria.

Stoyanova, D., ed., 1986, Topographic map of the Peoples's Republic of Bulgaria, scale: 1:500000, Primary Directorate for Geodesy, Cartography and Cadastre, Bureau of Cartography, Sofia.

Tsankov, Tz., R. Angelova, R. Nakov, B.C. Burchfiel and L. Royden, 1996, Basin Research, 8.

Velinov, T., 1986, Geothermal field in Bulgaria, Reviews Bulgarian Geol. Soc., v. XLVII, part i, p. 1-18 (in Bulgarian with English abstract).

Velinov, T. and K. Boyadjieva, 1981, Geotermichni izsledvania v Bulgaria (Geothermal studies in Bulgaria), Tehnika, Sofia (in Bulgarian).

Vening-Meinesz, F. A., 1950, Les "grabens" africains, resultat de compression ou de tension dans la croute terrestre?, Bulletin of the Royal Colonial Institute of Belgium, 21, 539-552.

Wernicke, B. and Axen, G. J., 1988, On the role of isostasy in the evolution of normal fault systems, Geology, 16, p. 848-851.

Zagorchev, I., 1992, Neotectonic development of the Struma (Kraistid) Lineament, southwest Bulgaria and northern Greece, Geological Magazine, 129, 197-222.

Table 2.1. Best Fitting Flexural Rigidities and Flexural Coefficients for Loading on One Side of a Plate of Uniform Rigidity, Quaternary Flexure.

	a(km)	b(km)	c(km)	d(km)	w_o(km)[a]	D(Nm)[b]	T_e(km)[c]	rms misfit
Profile A	0.9666	-2.3665	0	0	0.1200	7.67e22	22	0.0635
Profile B	1.5185	-0.9046	0	0	0.0408	5.76e22	5	0.1417
Profile D	0.5441	-1.8712	0	0	0.1042	1.94e23	30	0.0698
Profile E	0.4523	-1.7228	0	0	0.1001	1.94e23	30	0.0683

[a] w_o is the initial water depth obtained in the inversions.
[b] Flexural rigidity
[c] Effective elastic plate thickness.

Table 2.2. Best Fitting Flexural Rigidities and Flexural Coefficients for Loading on Both Sides of a Plate of Uniform Rigidity, Pliocene Flexure in the Carpathian Foredeep, Profile D

a(km)	b(km)	c(km)	d(km)	w_o(km)[a]	D(Nm)[b]	T_e(km)[c]	rms misfit
1.32320	0.34482	-1.15183	3.64516	-0.03277	5.76e22	20	46.5321
-2.47400	7.07581	-0.89128	3.50566	-0.13625	1.244e22	12	41.0083

[a] w_o is the initial water depth obtained in the inversions.
[b] Flexural rigidity
[c] Effective elastic plate thickness

Table 2.3. Best Fitting Flexural Rigidities and Flexural Coefficients for Loading on One Side of a Plate of Changing Rigidity[a], Quaternary Flexure.

	a(km)	b(km)	c(km)	d(km)	w_o (km)[b]	xt (km)[c]	D (Nm)[d]	T_{e1} (km)[e]	rms misfit
Profile A	0.8659	-0.3470	0	0	0.0373	10	1.94e20	3	0.1218
Profile B	0.7754	-0.4877	0	0	0.0364	10	1.94e21	3	0.0758
Profile D[f]	-	-	-	-	-	-	-	-	-
Profile E[f]	-	-	-	-	-	-	-	-	-

[a] Flexural rigidity for x > xt is fixed at D=5.76e22Nm, but can vary for 0 <x <xt.
[b] w_o is the initial water depth obtained in the inversions.
[c] xt is the x-coordinate of the point at which the plate changes rigidity.
[d] D1 here is for the region 0 < x < xt.
[e] Effective elastic plate thickness Te1 here is for the region 0 < x < xt.
[f] Profiles D and E did not give significantly better fits with a two-rigidity model than a uniform rigidity one.

FIGURE CAPTIONS

Figure 2.1. Mechanisms for generating high topography via shortening and extension. (a) At convergent boundaries high topography is formed by crustal thickening; (b) In extensional settings high topography is formed by uplift and rotation of footwall due isostatic compensation during normal faulting; (c) Mechanisms (a) and (b) operating in the same orogenic belt where thrusting and extension are widely separated in time, such as in the Stara Planina range, where thrusting is Mesozoic-Early Tertiary and the extension is Quaternary; (d) Mechanisms (a) and (b) operating together during coeval thrusting and "back-arc" extension.

Figure 2.2. (a) Major tectonic elements of central-eastern Europe, with the territory of Bulgaria indicated by a heavy line; (b) Major topographic features of Bulgaria with the location of the Sub-Balkan graben system shown in black. Other Middle Miocene and younger extensional basins are shown with closely spaced dots and late Neogene deposition along the Moesian plain is shown with widely spaced dots. SB = Sofia graben, M = Mesta graben, S = Struma graben. (Figure modified from Tzankov et al.,1996.)

Figure 2.3. Simplified north-south cross-sections across the sub-Balkan graben system and corresponding approximately to profiles A (top) and B (bottom) on Figure 2.5. Graben fill is shown by dotted and cross-hatched areas and arrows show sense of motion on graben-bounding normal faults.

Figure 2.4(a) North-south topographic profile across the Stara Planina along Profile C. Arrows show the position of the Quaternary grabens on the south side of the range and the position of the frontal thrust fault of the Stara Planina. (b) Cross-section along profile C constructed from surface geological data and unpublished seismic and drilling data. pP = pre-Permian metamorphic rocks; Tr1u = base Triassic unconformity; J3K1a,b = Upper Jurassic - Lower Cretaceous sedimentary

rocks in surface outcrop; K1a,b = Lower Cretaceous sedimentary rocks exposed at the surface; K2 = Upper Cretaceous sedimentary rocks. Details of hanging wall structure above the Mesozoic foreland sequence cannot be resolved on the seismic section. No vertical exaggeration.

Figure 2.5. Smoothed topographic map of the central Stara Planina, after Stoyanova (1986), and locations of profiles A-E. The east-trending dark solid line indicates the locations of the highest topographic points along the range. Stippled regions to the south of the range are extensional grabens bounded on the south side by the Sredna Gora mountains. Thick barbed lines indicate south dipping normal faults (barbs on the hanging wall).

Figure 2.6. Topographic data for profiles A-E. Profile C contains data with no lateral average; other profiles contain data averaged across a 40 km wide swath. All data was smoothed using a five-point moving window average. By definition, x=0 corresponds to the crest of the Stara Planina. The thick solid line shows Quaternary grabens on the south side of the Stara Planina.

Figure 2.7.(a) Deflection data used to constrain the flexure of the Moesian platform along profile C. Smaller dots indicate the depth to base Neogene beneath the South Carpathian foredeep. Larger dot is the location of the frontal thrusts of the Stara Planina. (b) Bouguer gravity data along Profile C.

Figure 2.8. Best fitting flexural solutions for profiles A, B, D and E as described in the text for a uniformly strong plate with T_e=10 km (solid line) and T_e=20 km (dashed line). Profiles D and E are reasonably well fit by flexure of a uniformly strong plate while Profiles A and B are not.

Figure 2.9. Best-fitting flexural solutions for profile C using a uniformly strong plate with T_e=12 and 20 km, using a simultaneous joint solution for deflection and gravity data. (a) Fit to deflection data. Star indicates the toe of Mesozoic-Early Tertiary thrust sheets. (b) Fit to gravity data. (c) RMS-misfit as a function of T_e. Stars show T_e=12 and 20 km.

Figure 2.10. Best flexural solutions for profile A using a two-rigidity plate as described in the text. Dots show the transition between effective elastic plate strength T_{e1} (small values of x) and effective elastic plate strength T_{e2} (large values of x). Dark line shows topographic data, lighter line shows flexural solution. Right-hand panels (ii) show rms-misfit as a function of T_e. Transition point is defined to be x=10 km (a), x=15 km (b) and x=5 km (c).

Figure 2.11. Best flexural solutions for profile B using a two-rigidity plate as described in the text. Dots show the transition between effective elastic plate strength T_{e1} (small values of x) and effective elastic plate strength T_{e2} (large values of x). Dark line shows topographic data, lighter line shows flexural solution. Right-hand panels (ii) show rms-misfit as a function of T_e. Transition point is defined to be x=10 km (a), x=15 km (b) and x=5 km (c).

Figure 2.12. Best flexural solutions for profile B using a two-rigidity plate as described in the text, and using topographic data from ridges only. Dots show the transition between effective elastic plate strength T_{e1} (small values of x) and effective elastic plate strength T_{e2} (large values of x). Dark line shows topographic data, lighter line shows flexural solution. Right-hand panels (ii) show rms-misfit as a function of T_e. Transition point is defined to be x=10 km (a), x=15 km (b) and x=5 km (c).

Figure 2.13. Best flexural solutions for profile B using a two-rigidity plate as described in the text, and using topographic data from valleys only. Dots show the transition between effective elastic plate strength T_{e1} (small values of x) and effective elastic plate strength T_{e2} (large values of x). Dark line shows topographic data, lighter line shows flexural solution. Right-hand panels (ii) show rms-misfit as a function of T_e. Transition point is defined to be x=10 km (a), x=15 km (b) and x=20 km (c).

Figure 2.14. (a) Schematic representation of crustal thinning as a result of displacement on a normal fault, neglecting isostatic uplift of the footwall. Shaded area indicates the material removed during extension. (b) Material removed from above the south-dipping normal faults that bound the Stara Planina and the Sub-Balkan graben system, computed as described in text. Reconstruction neglects isostatic response to unloading, giving pre-faulting geometry. Shaded and cross-hatched areas indicate material to be removed during extension, cross-hatched area shows region of graben sediments. (c) Same as (b) but with the inclusion of isostatic response to unloading.

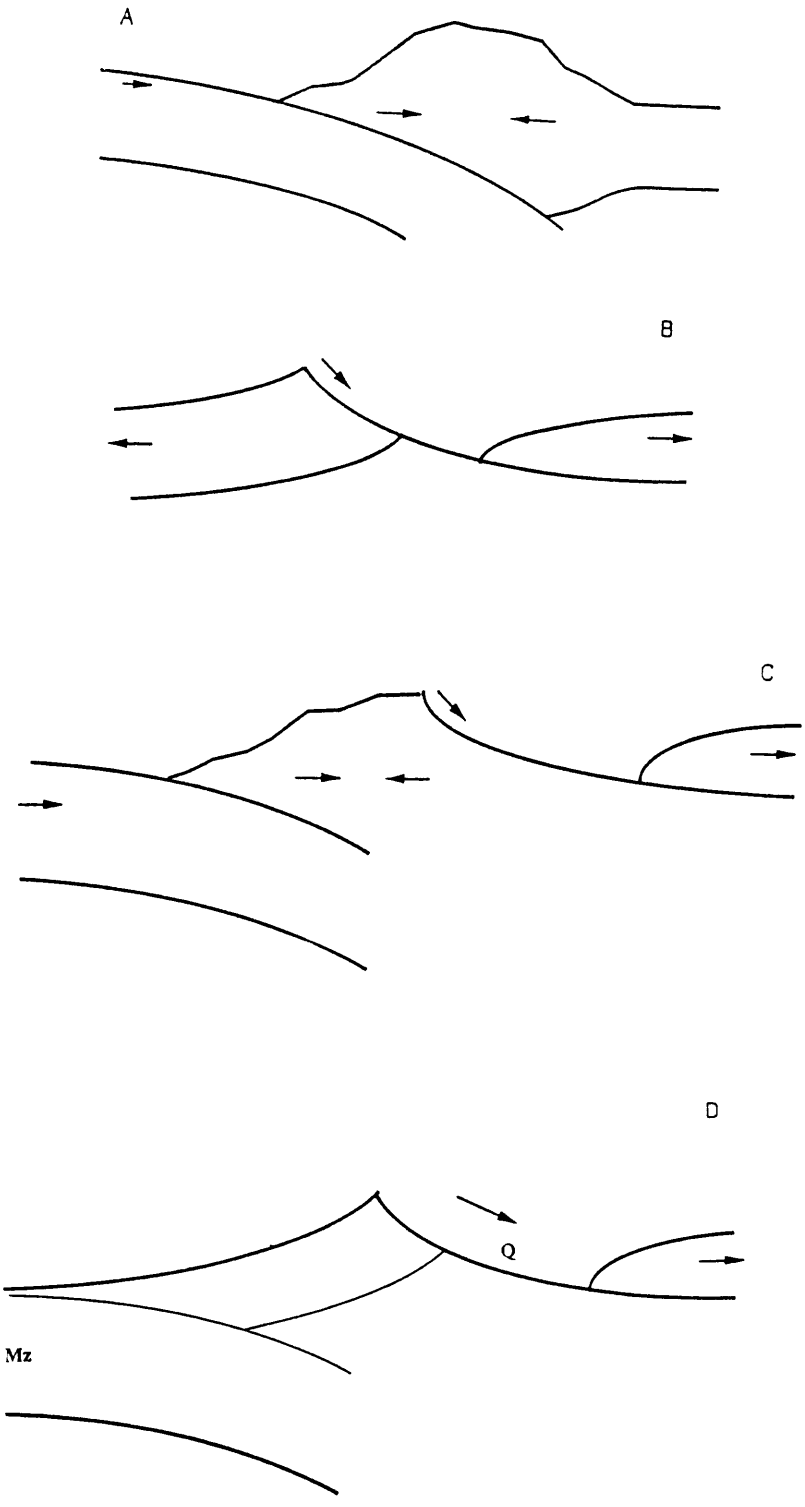

Figure 2.1

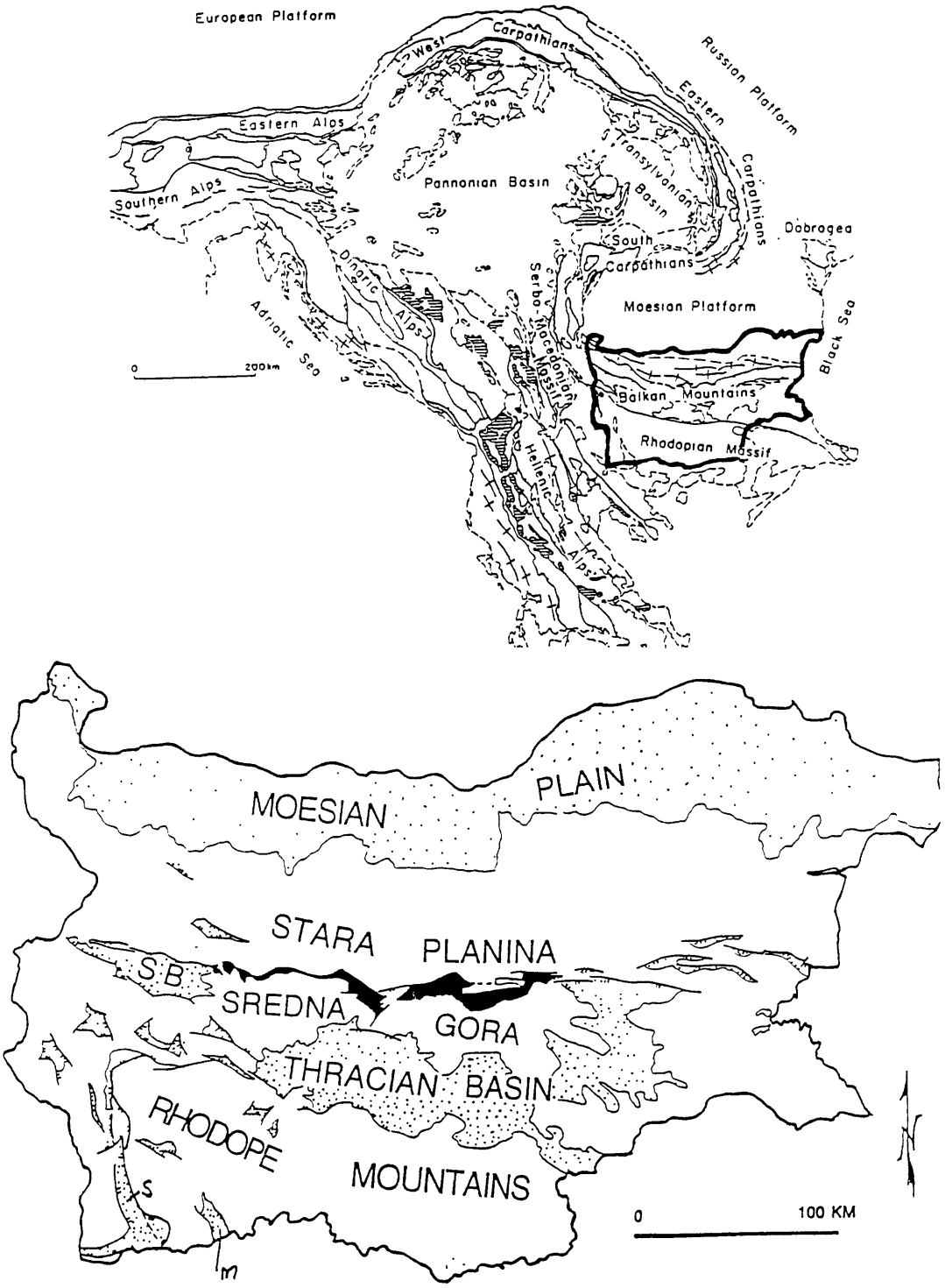
European Platform
West
Carpathians
Russian Platform
Eastern
Eastern Alps
Transylvanian
Basin
Carpathians
Pannonian Basin
Southern Alps
Dobrogea
South
Carpathians
Dinaric Alps
Serbo-Macedonian Massif
Moesian Platform
Black Sea
Adriatic Sea
0
200km
Balkan Mountains
Rhodopian Massif
Hellenic Alps
MOESIAN PLAIN
STARA PLANINA
S B
SREDNA GORA
THRACIAN BASIN
RHODOPE MOUNTAINS
N
0
100 KM

Figure 2.2

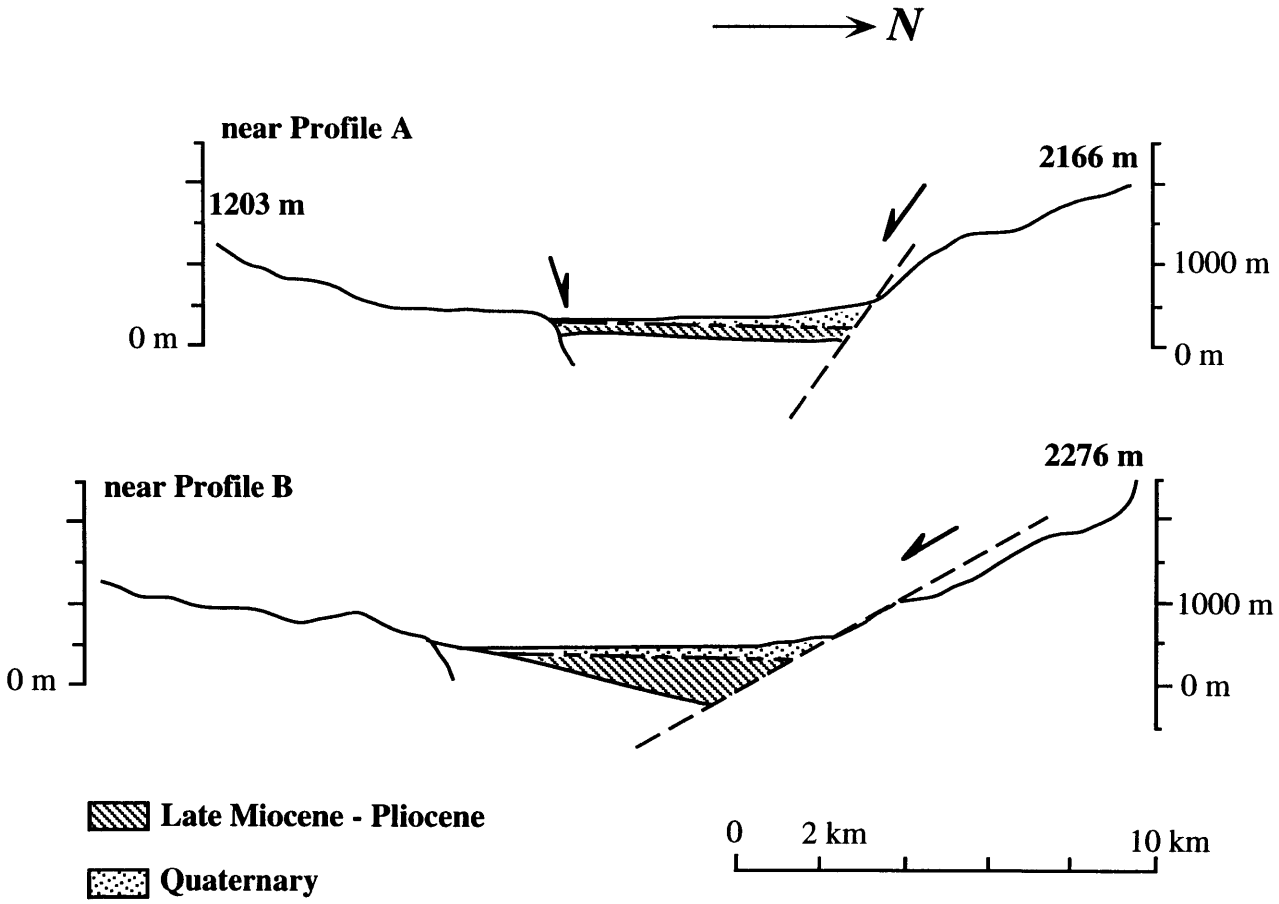
N
near Profile A
1203 m
0 m
2166 m
1000 m
0 m
near Profile B
0 m
2276 m
1000 m
0 m
Late Miocene - Pliocene
Quaternary
0
2 km
10 km

Figure 2.3

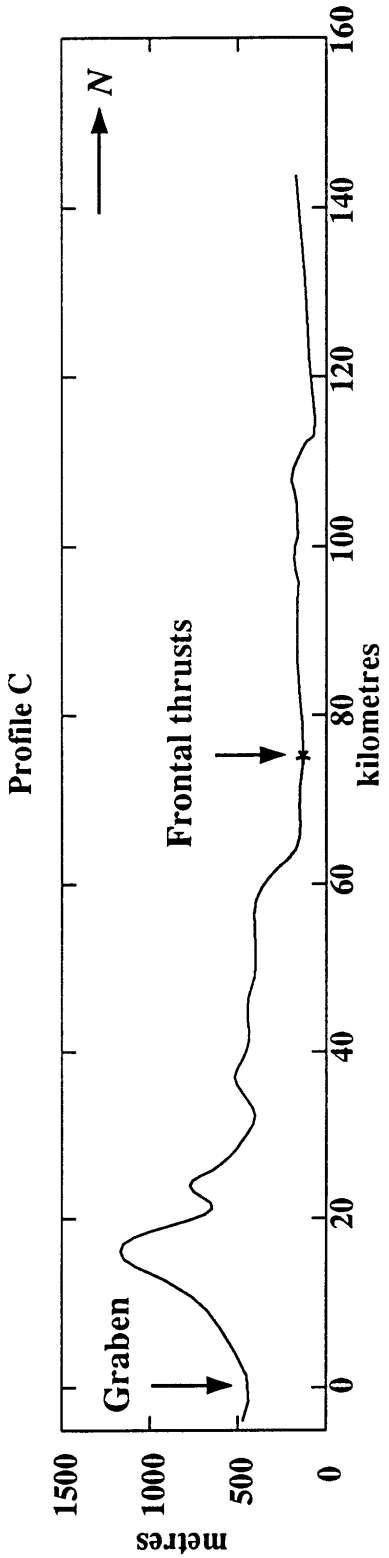
Profile C
Graben
Frontal thrusts
N
metres
1500
1000
500
0
0
20
40
60
80
100
120
140
160
kilometres

Figure 2.4a

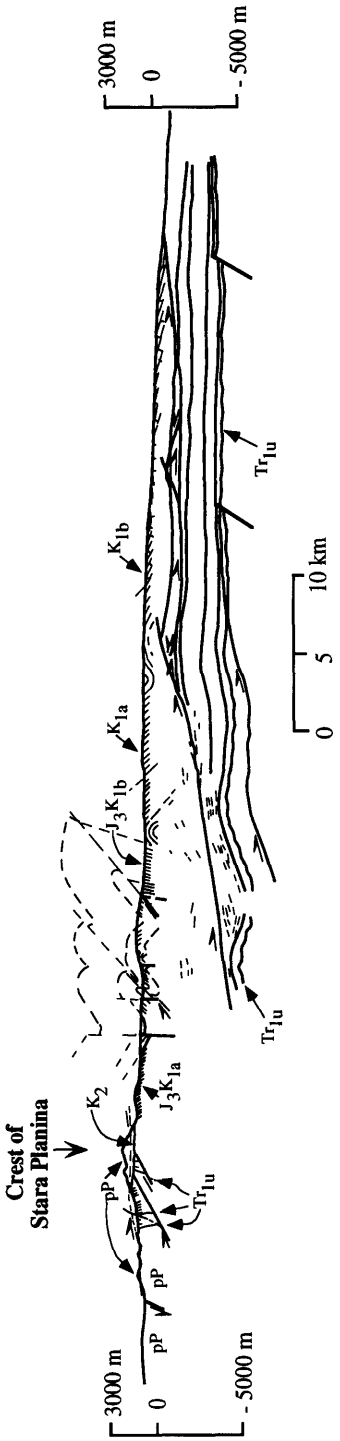
3000 m
0
- 5000 m
Tr_{1u}
K_{1b}
10 km
0 5
K_{1a}
J_3K_{1b}
Tr_{1u}
K_2
J_3K_{1a}
Crest of
Stara Planina
pP
Tr_{1u}
pP
pP
3000 m
0
- 5000 m

Figure 2.4b

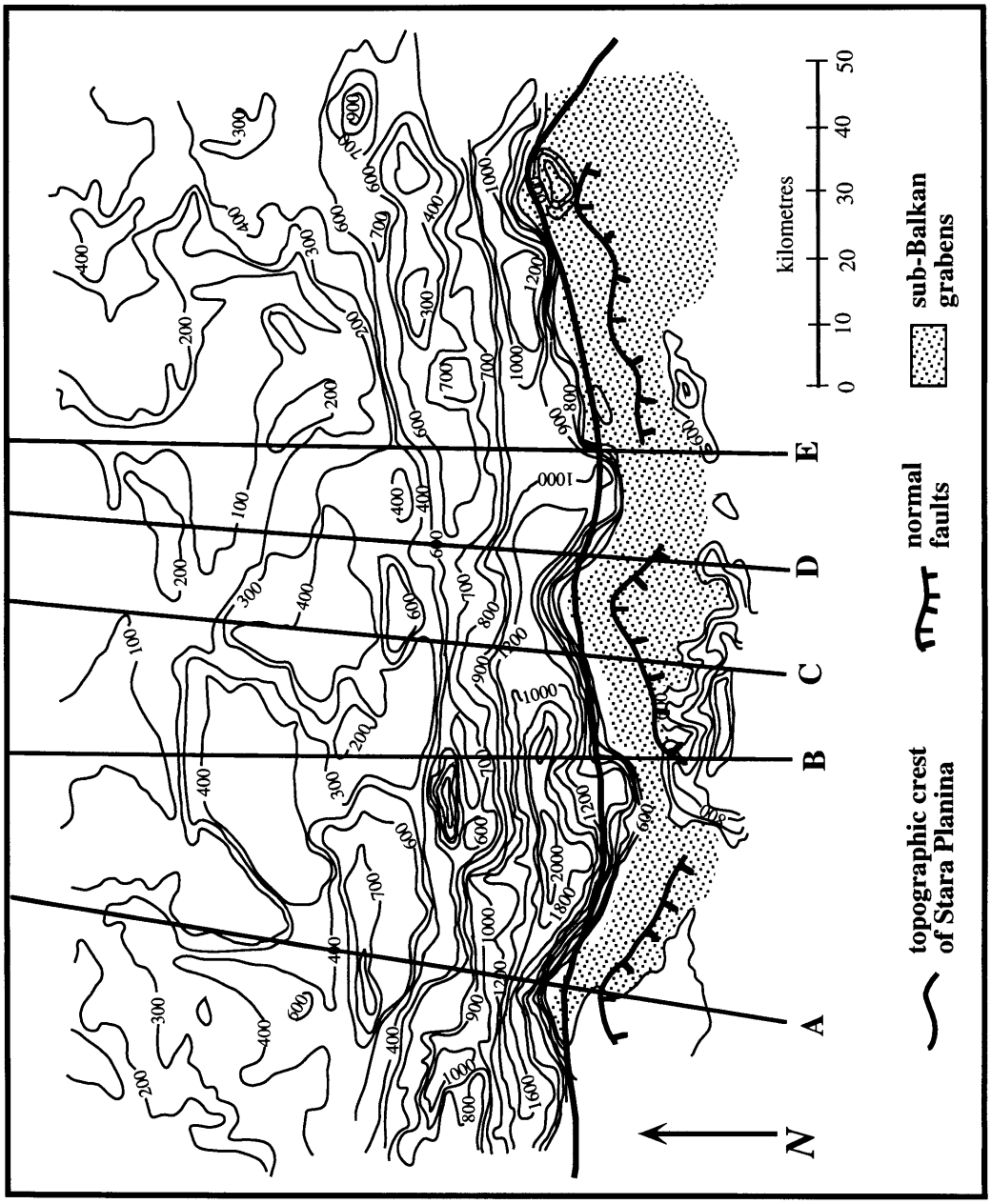
N
A
B
C
D
E
kilometres
0 10 20 30 40 50
topographic crest of Stara Planina
normal faults
sub-Balkan grabens

Figure 2.5

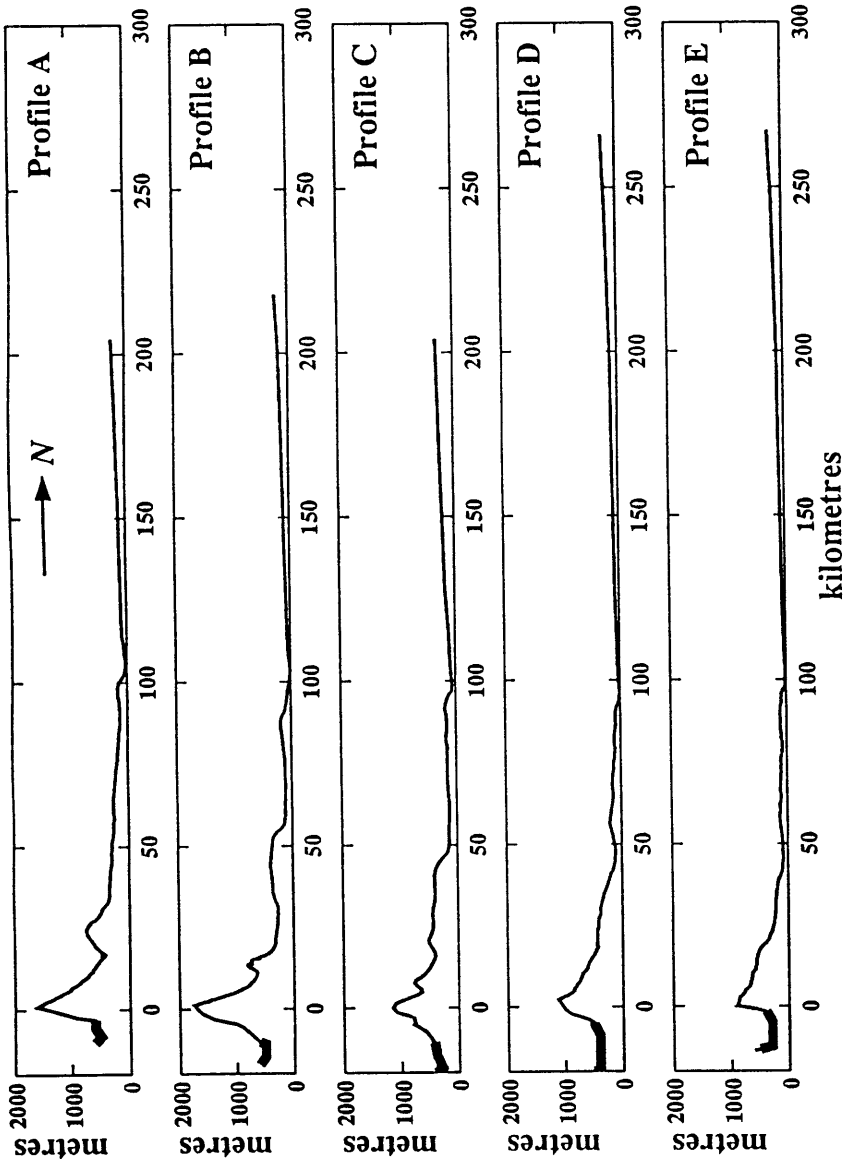
Profile A
Profile B
Profile C
Profile D
Profile E
N
metres
2000
1000
0
0
50
100
150
200
250
300
kilometres

Figure 2.6

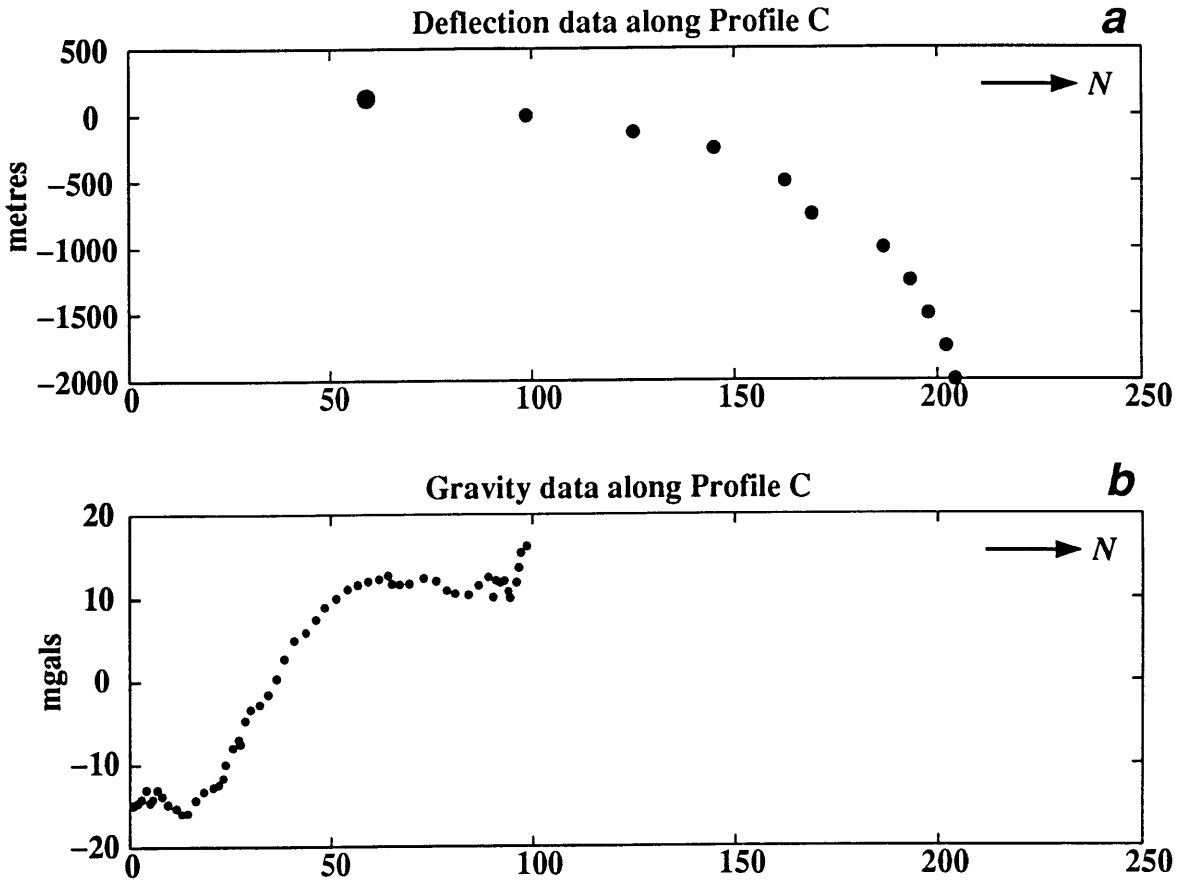
Deflection data along Profile C
a
500
0
−500
−1000
−1500
−2000
metres
N
0
50
100
150
200
250
Gravity data along Profile C
b
20
10
0
−10
−20
mgals
N
0
50
100
150
200
250

Figure 2.7

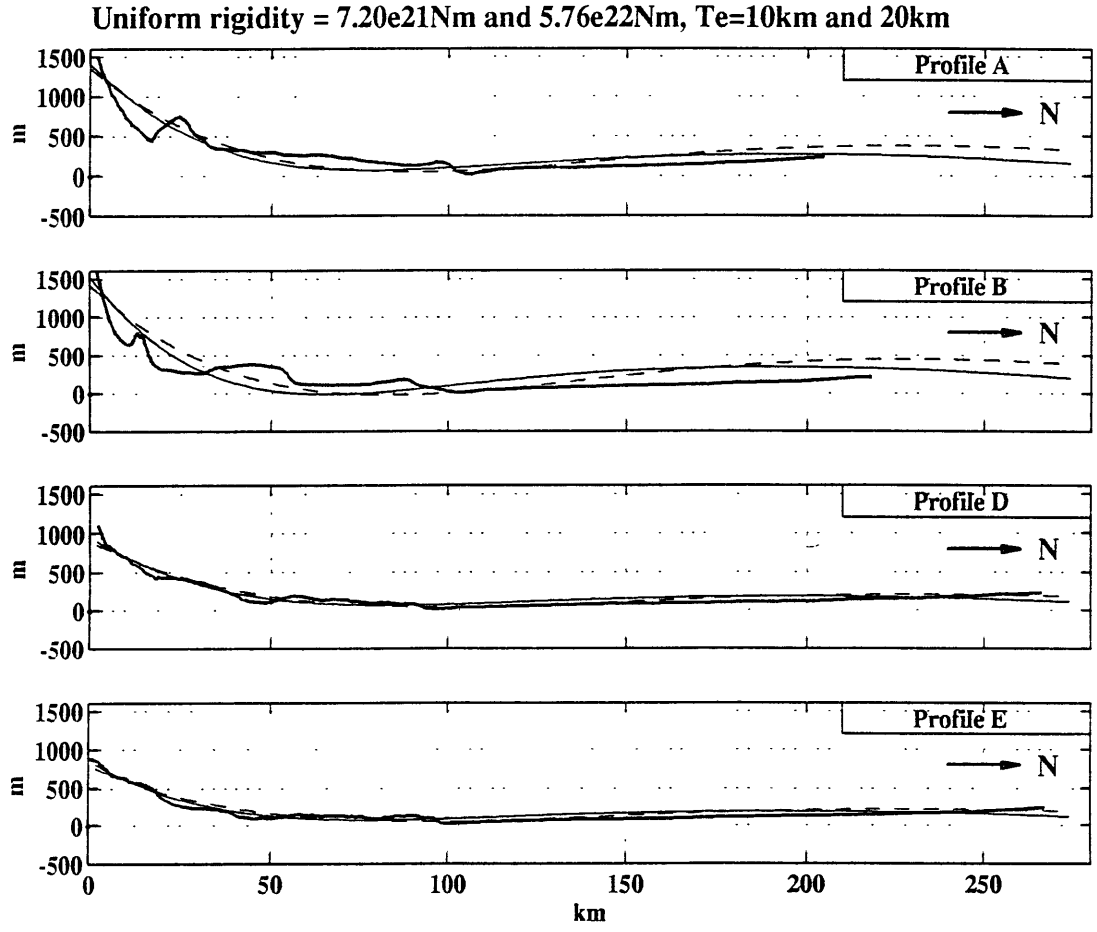
Uniform rigidity = 7.20e21Nm and 5.76e22Nm, Te=10km and 20km
Profile A
Profile B
Profile D
Profile E
N
m
1500
1000
500
0
-500
0
50
100
150
200
250
km

Figure 2.8

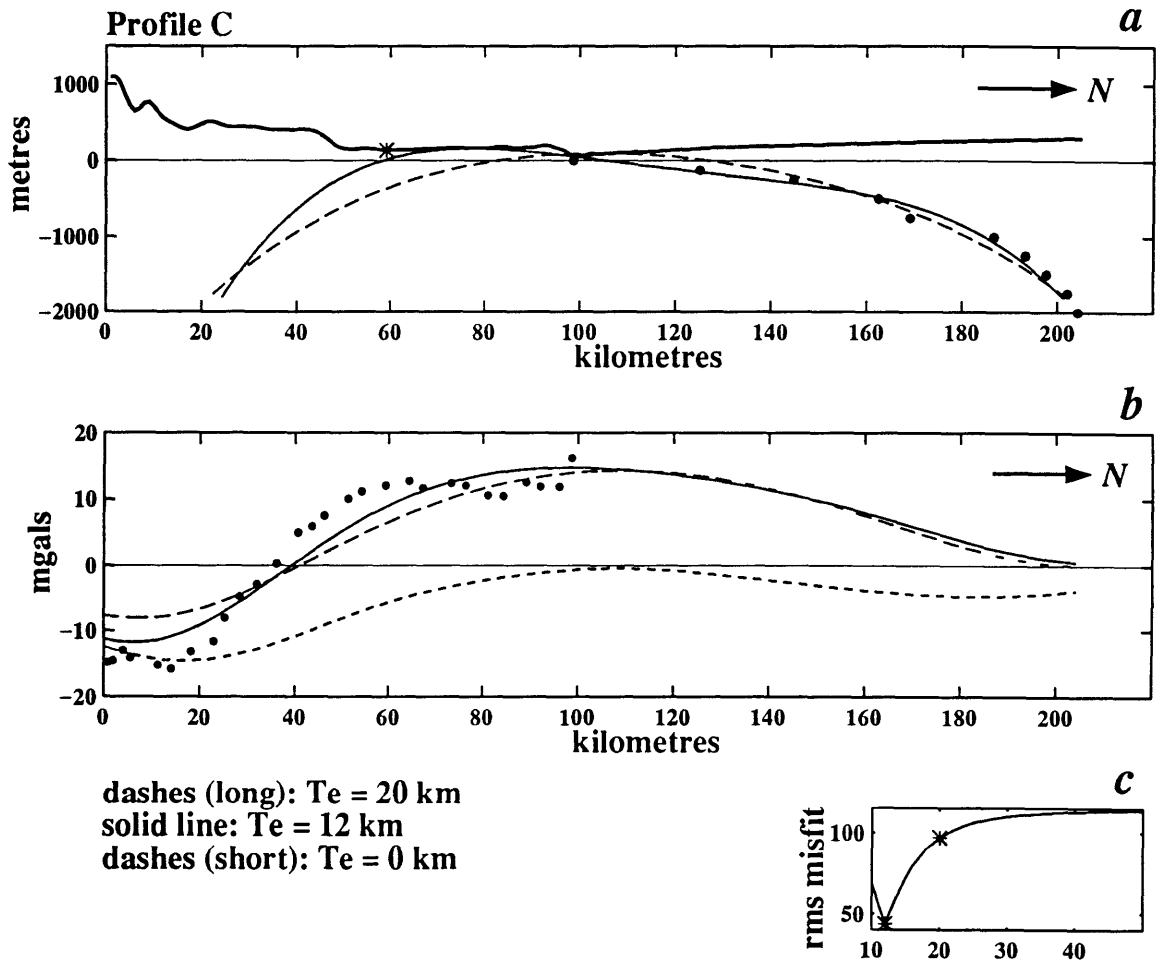
Profile C
a
1000
0
-1000
-2000
metres
N
0
20
40
60
80
100
120
140
160
180
200
kilometres
b
20
10
0
-10
-20
mgals
N
kilometres
dashes (long): Te = 20 km
solid line: Te = 12 km
dashes (short): Te = 0 km
c
rms misfit
100
50
10
20
30
40

Figure 2.9

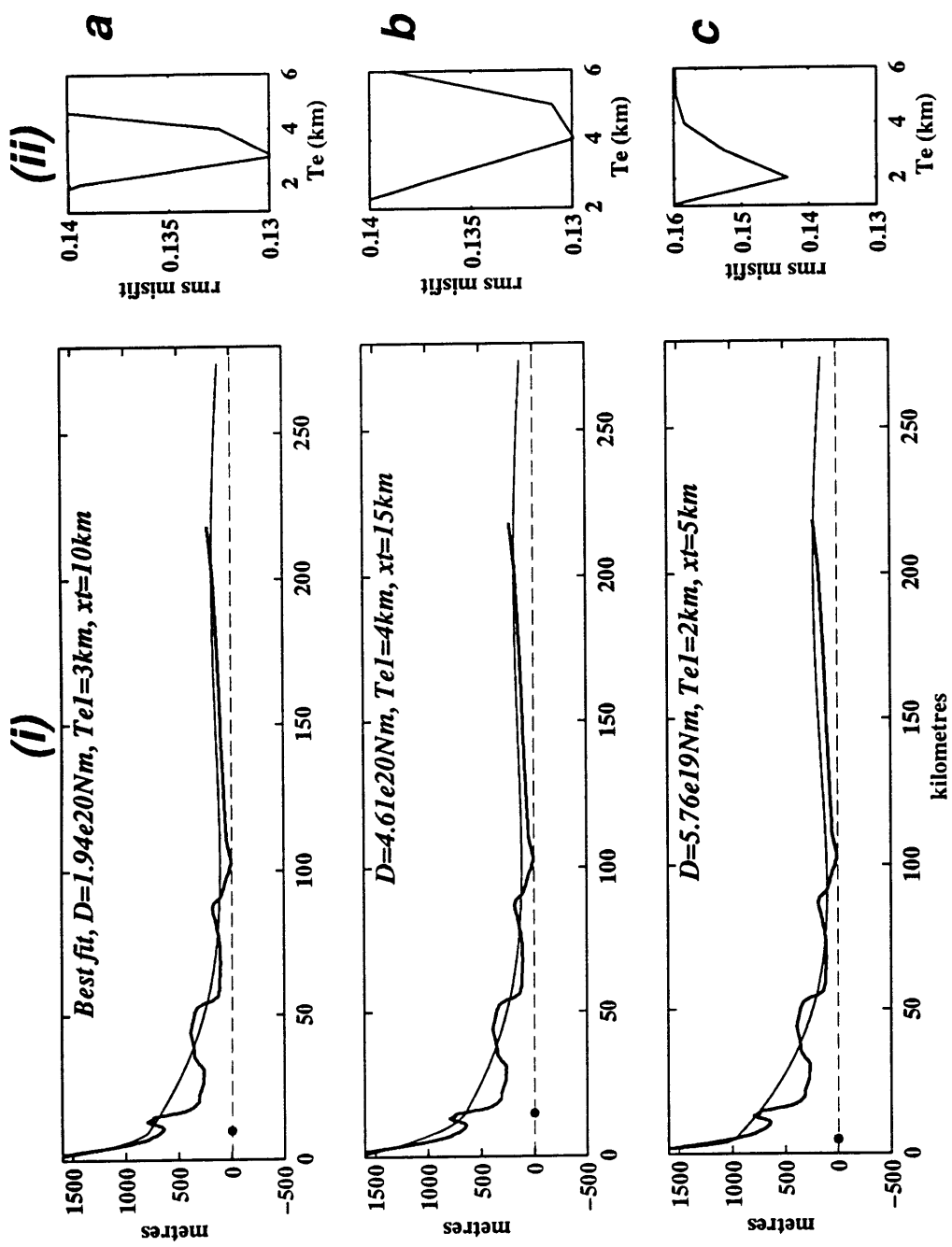
(i)
Best fit, D=1.94e20Nm, Te1=3km, xt=10km
D=4.61e20Nm, Te1=4km, xt=15km
D=5.76e19Nm, Te1=2km, xt=5km
metres
kilometres
(ii)
a
b
c
rms misfit
Te (km)

Figure 2.10

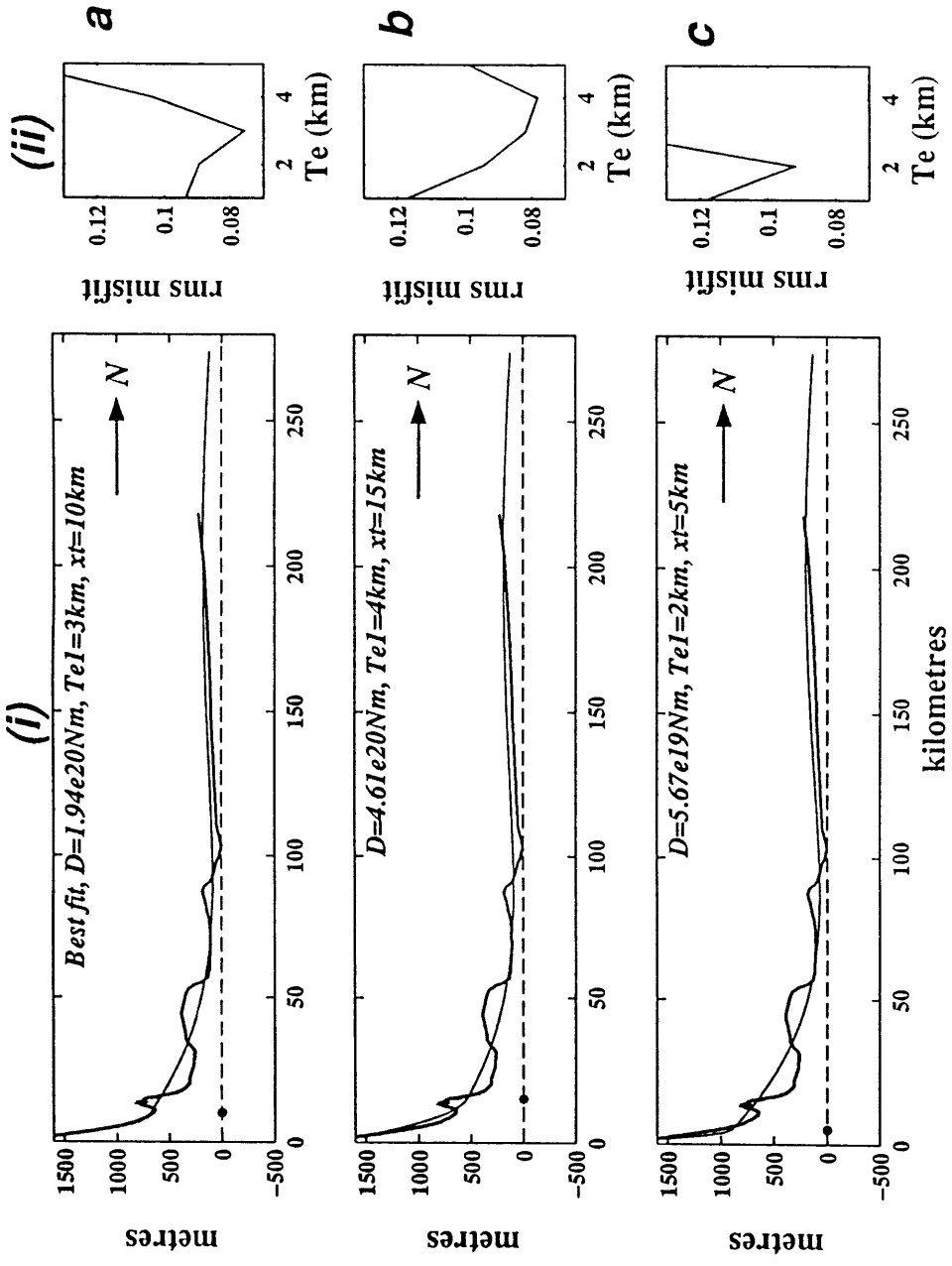
(i)
Best fit, D=1.94e20Nm, Te1=3km, xt=10km
D=4.61e20Nm, Te1=4km, xt=15km
D=5.67e19Nm, Te1=2km, xt=5km
N
metres
kilometres
(ii)
a
b
c
rms misfit
Te (km)

Figure 2.11

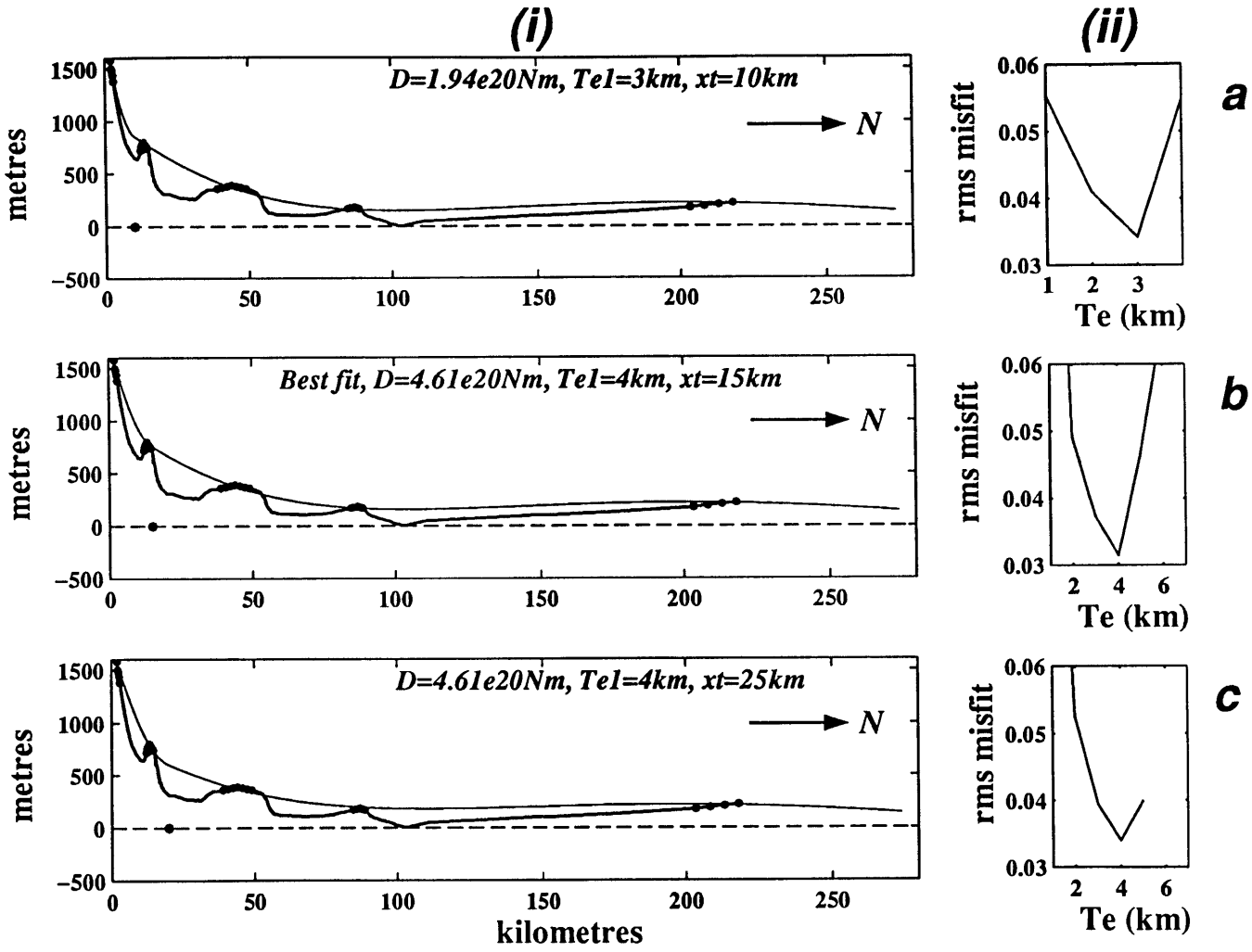
(i)
(ii)
D=1.94e20Nm, Te1=3km, xt=10km
Best fit, D=4.61e20Nm, Te1=4km, xt=15km
D=4.61e20Nm, Te1=4km, xt=25km
N
metres
kilometres
rms misfit
Te (km)
a
b
c

Figure 2.12

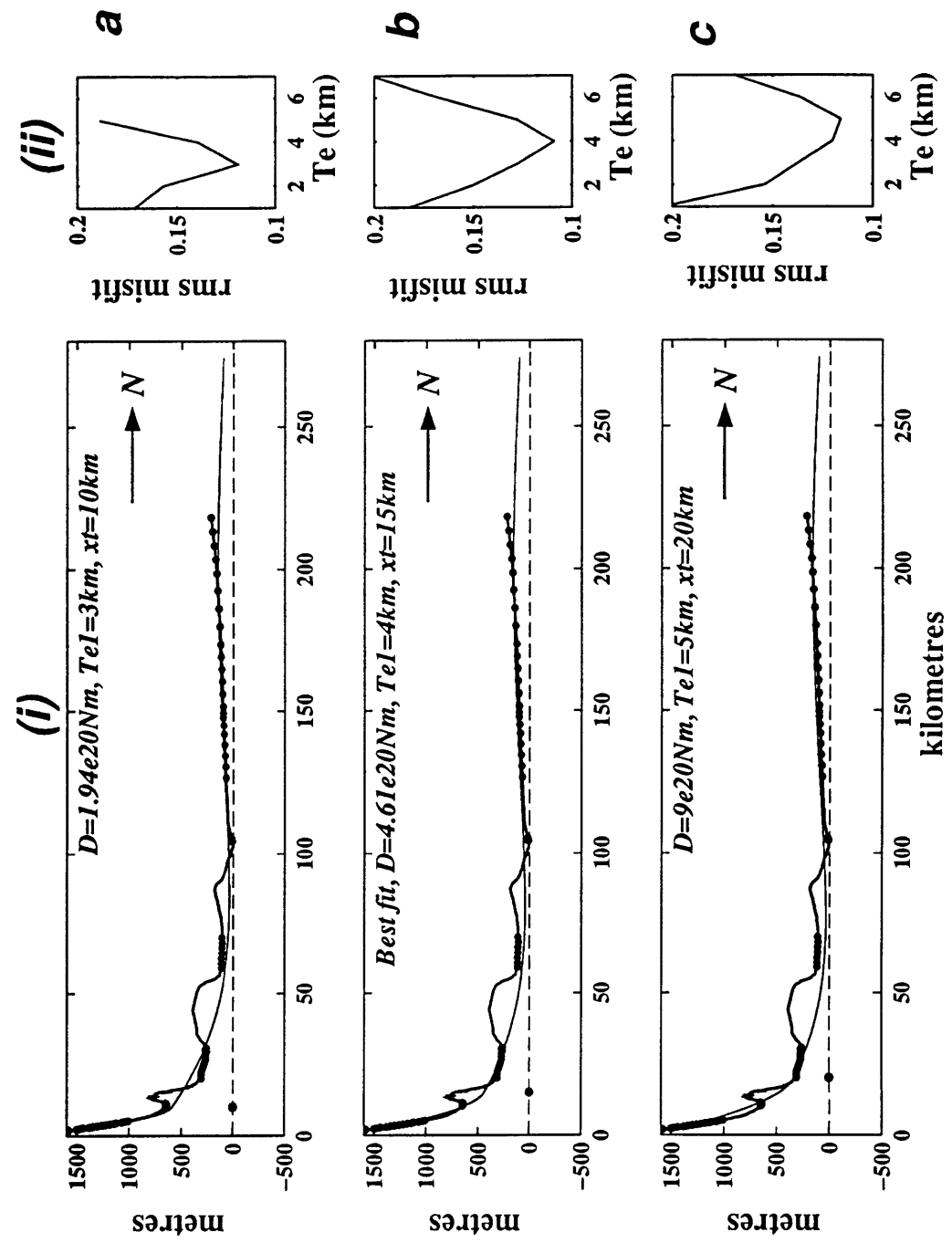
(i)
(ii)
a
b
c
D=1.94e20Nm, Te1=3km, xf=10km
Best fit, D=4.61e20Nm, Te1=4km, xf=15km
D=9e20Nm, Te1=5km, xf=20km
N
metres
kilometres
rms misfit
Te (km)

Figure 2.13

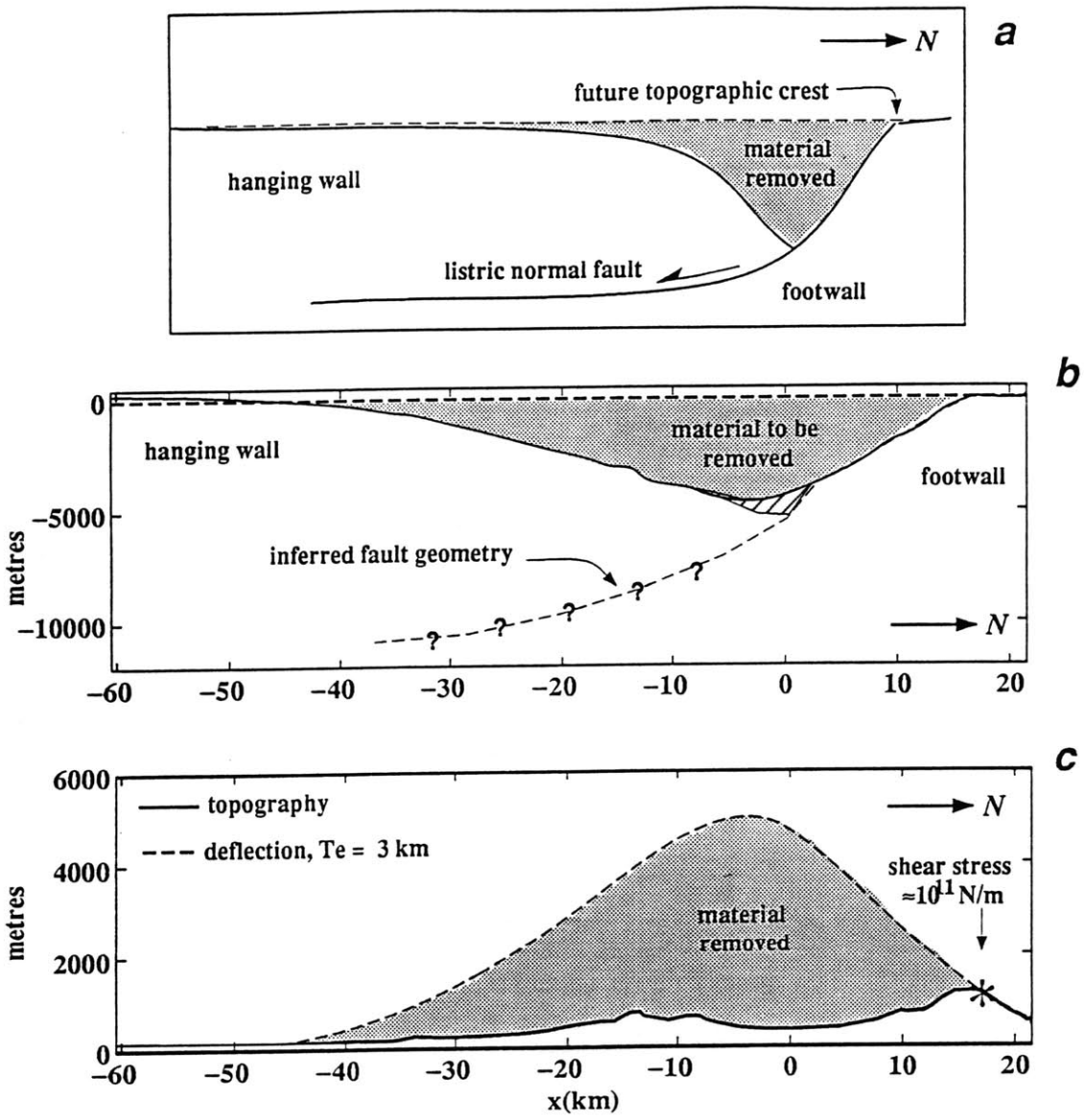
a
N
future topographic crest
material removed
hanging wall
listric normal fault
footwall
b
0
-5000
-10000
metres
hanging wall
material to be removed
footwall
inferred fault geometry
N
-60
-50
-40
-30
-20
-10
0
10
20
c
6000
4000
2000
0
metres
topography
deflection, Te = 3 km
N
shear stress
≈10^11 N/m
material removed
x(km)

Figure 2.14

Chapter 3

Earthquake Nucleation on Model Faults With Rate and State-Dependent Friction: The Effects of Inertia[1]

ABSTRACT

Laboratory studies suggest that earthquake nucleation involves a transition from quasi-static slip when inertial effects are negligible, to inertia-driven, dynamic motion. This transition occurs via quasi-dynamic motion, during which the effects of inertia become increasingly important. The characteristics of this transition, which depend on frictional properties of the fault, determine the observability of earthquake nucleation by seismic, geodetic, or other means. By investigating the role of inertia during nucleation, we obtain a quantitative definition of the limiting velocity V_{in}, which marks the end of quasi-dynamic motion and the onset of instability. For reasonable friction parameters and fault widths, we obtain estimates of V_{in} for crustal faults. To study the roles of inertia, stiffness, and friction parameters on preseismic motion, we simulate triggered instabilities in a 1-D model of a homogeneous fault, with rate and state variable friction. In most of our simulations, triggering is achieved by applying a stress perturbation to an initially creeping fault under steady-state friction. We also investigate triggering on faults which are initially locked and over-stressed compared to their nominal frictional strength, due to time-dependent healing. We study the amount, U_p, and duration, T_p, of preseismic slip as a function of system mass m, and other model parameters. For crustal faults, we interpret the relevant mass as a

---

[1] Roy, M. and C. Marone, Earthquake nucleation on model faults with rate- and state-dependent friction: Effects of inertia, *J. Geophys. Res.*, *101*, 13,919-13,932, 1996.

product of density and fault width, and find that wider fault zones result in smaller U_p and larger T_p. Both U_p and T_p are proportional to the system stiffness K, the characteristic slip distance D_c, and the friction constitutive parameter a, and inversely proportional to the size of the triggering event. We find greater U_p and T_p for constitutive laws which allow strengthening at zero velocity, compared to laws that require slip or a combination of slip and aging for state evolution. In contrast to quasi-static modeling, our simulations suggest a minimum stress perturbation criterion for instability, which may be interpreted in terms of a strain threshold for triggered seismicity.

INTRODUCTION

There is growing evidence from laboratory data, seismic observations, and theoretical modeling that earthquake nucleation involves an identifiable transition from quasi-static creep to dynamically driven motion [*Scholz et al.*, 1972; *Dieterich*, 1978, 1981a, 1986, 1992; *Okubo and Dieterich*, 1984; *Ohnaka and Kuwahara*, 1990; *Shibazaki and Matsu'ura*, 1992, 1995; *Iio*, 1992, 1995; *Ohnaka*, 1993; *Abercrombie and Mori*, 1994; *Baumberger et al.*, 1994, *Kato et al.*, 1994; *Ellsworth and Beroza*, 1995]. This transition involves the accumulation of finite fault slip, suggesting that time- and state-dependent frictional behavior play a key role in the nucleation process. Laboratory friction experiments show that pre-instability motion consists of an initial, steady creep phase during which motion is quasi-static, followed by slow but self-driven acceleration [*Scholz et al.*, 1972; *Dieterich*, 1981a; *Ohnaka and Yamashita*, 1989; *Kato et al*, 1994]. Such quasi-dynamic motion may produce distinct seismic and geodetic signatures, however, these signatures and the extent to which crustal faults reproduce laboratory behavior depends on details of the frictional properties. Thus a central problem in identifying and interpreting characteristics of

earthquake nucleation is that of understanding the effect of friction parameters on the transition from quasi-static to dynamic slip.

Previous theoretical studies of earthquake nucleation use arbitrary velocity cut-offs to denote the onset of the onset of instability and assume that the nucleation process is purely quasi-static [*Dieterich*, 1986, 1992; *Rice and Tse*, 1986], but see *Gu and Wong* [1991] and *Weeks* [1993]. As a result, these studies do not fully model quasi-dynamic acceleration prior to the onset of instability. Other studies, which have included the effects of inertia [e.g., *Sleep*, 1995a,b; *Segall and Rice*, 1995], have focused primarily on shear heating, compaction, and dilation as they relate to instability. These studies do not define the transition from quasi-static to dynamic slip, nor do they address the role of friction in determining characteristics of preseismic slip and earthquake nucleation.

In this study, we investigate the effect of friction parameters, friction laws, and inertia on preseismic slip and quasi-dynamic motion preceding earthquake-like instability. We derive, via the equations of motion, a quantitative definition of the transition from quasi-static to dynamic slip. To focus on the friction parameters and constitutive formulations and avoid the complicating effects of geometry, we use a single-degree-of-freedom elastic model of a homogeneous fault (Figure 3.1). Friction is assumed to obey rate and state variable constitutive laws and fault normal stress is constant. We do not consider effects of rupture growth or dynamic rupture propagation, nor do we account for dilation, compaction, or shear heating. We investigate the amount, U_p, and duration, T_p, of preseismic slip as a function of mass per unit fault area m, stiffness K, stress perturbation η, and the friction parameters and constitutive formulation. In the majority of our simulations, we trigger instability by applying a stress perturbation to a fault undergoing slow creep under steady-state friction. In addition, we also consider cases in which the fault is initially locked and over-stressed due to time-dependent frictional strengthening.

We define two distinct phases of motion during preseismic nucleation: a quasi-static phase, with a limiting slip velocity of V_{qs}, and a quasi-dynamic phase, which involves slow acceleration to a limiting velocity V_{in}. The velocity V_{in} defines the point at which motion becomes inertia-dominated. We find that this definition is consistent with unstable motion as predicted by a linear stability analysis. In the limit of negligible system mass, the duration of quasi-dynamic motion approaches zero, and we recover the purely quasi-static nucleation process assumed by *Dieterich* [1986, 1992].

In the following section, we describe the rate and state variable constitutive laws used in the simulations and derive the limiting velocities V_{qs} and V_{in}. Next, we present the results of our simulations to illuminate the effects of inertia and constitutive parameters on preseismic nucleation. By varying mass with all other parameters fixed, we determine its role during preseismic nucleation.

RATE AND STATE VARIABLE CONSTITUTIVE LAWS

Laboratory studies indicate that rock friction is a function of both instantaneous sliding velocity ("rate") and sliding history ("state") [*Dieterich* 1979, 1981b; *Ruina*, 1980, 1983; *Scholz*, 1990]. Two types of rate/state friction laws have been proposed to account for different types of state evolution [e.g., *Beeler et al.*, 1994; *Perrin et al.*, 1995]. In this paper we explore three specific rate/state constitutive laws, however, we focus primarily on the type of law proposed by *Dieterich* [1979]:

$$\mu = \mu_o + a\ln\left(\frac{V}{V_o}\right) + b\ln\left(\frac{V_o\psi}{D_c}\right) \tag{3.1}$$

$$\frac{d\psi}{dt} = 1 - \frac{V\psi}{D_c}. \tag{3.2}$$

Here, μ is the coefficient of friction, V is the instantaneous sliding velocity, V_o is a constant reference velocity for which steady-state friction is μ_o, ψ is the state variable, and D_c is a characteristic slip distance. The terms a, b, and D_c are constitutive parameters determined experimentally [e.g., *Dieterich*, 1979; *Tullis and Weeks*, 1988; *Marone et al.*, 1990; *Reinen and Weeks*, 1994]. The second and third terms in equation (3.1) represent the instantaneous velocity and state dependence of friction, respectively. Equation (3.2) describes friction state evolution and indicates that state cannot change instantaneously, but rather evolves with time t and characteristic displacement D_c. This relation allows for friction evolution during stationary contact, in contrast to another law we use and describe more fully below, in which friction evolution requires finite slip [*Ruina*, 1983].

Because rate/state friction laws have been discussed in detail [e.g., *Rice and Gu*, 1983; *Tullis*, 1988; *Scholz*, 1990; *Linker and Dieterich*, 1992] we restrict attention here to a few key points. Figure 3.2 shows the friction response described by (3.1) and (3.2) to a step change in velocity. The parameter a scales the instantaneous friction increase at constant state and b scales friction evolution over characteristic slip distance D_c. The change in steady-state friction scales with $(a\text{-}b)$ and from (3.2) the steady-state value of the state parameter ψ is D_c/V. If $a<b$, the evolution effect outweighs the direct effect and friction exhibits so-called velocity weakening (Figure 3.2). For $b<a$, steady-state friction increases with velocity (so-called velocity strengthening).

Velocity weakening frictional behavior is a necessary condition for instability [*Rice and Ruina,* 1983], and from numerous seismic observations, such as the depth-frequency distribution of seismicity [e.g., *Marone and Scholz,* 1988; *Blanpied et al.*, 1991], we infer $(a\text{-}b)< 0$ for the seismogenic region of crustal faults. Thus, in our simulations we set $(a-b)<0$ and use parameter ranges consistent with laboratory results [*Dieterich*, 1979; *Marone and Cox*, 1994; *Reinen et al.*, 1994; *Blanpied et al.*, 1995].

TRANSITION FROM QUASI-STATIC TO DYNAMIC SLIP

In the context of our model, fault slip and rupture nucleation is determined by the equation of motion of the mass coupled to the constitutive formulation for fault friction. We begin by defining a limiting velocity for quasi-static motion, using solutions to the linearized equations of motion, and then consider the transition from quasi-static to dynamic motion.

Following *Rice and Ruina* [1983], the equation of motion of a spring-slider system, initially at steady-state, but subjected to an arbitrary perturbing stress $q(t)$ may be written:

$$m\ddot{x}(t) = \tau_o - Kx(t) - \tau(t) + q(t), \tag{3.3}$$

where m is the mass per unit area, τ is shear stress given by $\mu\sigma$ where σ is normal stress, τ_0 is steady-state shear stress, K is stiffness, $x(t)$ is the change in slider position, and dots indicate time derivatives. From a linear stability analysis of this equation coupled to the constitutive law (3.1) and (3.2) [*Rice and Ruina*, 1983], the critical stiffness for unstable motion is:

$$K_c = \frac{\sigma(b-a)}{D_c}\left[1 + \frac{mV_o^2}{\sigma a D_c}\right]. \tag{3.4}$$

Linearized Equations of Motion

Assuming that the perturbing force is a Heaviside function, $q(t)=q_o\Theta(t)$, the position and velocity of the slider for $t>0$ are: $s(t) = V_o t + x(t)$ and $V(t) = V_o + \dot{x}(t)$, respectively. In addition, the state variable is perturbed from its steady-state value, $\Psi(t)= D_c/V_o + \xi(t)$. Substituting these expressions into equation (3.3) and writing $k=K/\sigma$ we obtain linearized

equations for the perturbed quantities valid for $t>0$ (neglecting all terms that are of second or higher order in the perturbations),

$$m\ddot{x}(t) = \sigma\left(-kx(t) - \frac{a\dot{x}(t)}{V_O} - \frac{bV_O\xi(t)}{D_C}\right) + q_O \tag{3.5}$$

$$\dot{\xi}(t) = -\left(\frac{V_O\xi(t)}{D_C} + \frac{\dot{x}(t)}{V_O}\right). \tag{3.6}$$

Quasi-static Limit

In the limit of quasi-static motion the acceleration term in equation (3.5) is negligible so that $0 = Kx(t) + (\sigma a\dot{x}(t)/V_o) + (\sigma bV_o\xi(t)/D_c) - q_o$. The critical stiffness is then $K_C = \sigma(b-a)/D_C$ [*Ruina*, 1980; *Gu et al.*, 1984], which is equivalent to equation (3.4) when $mV_O^2/\sigma aD_C \ll 1$, i.e. at small steady-state velocities. As steady-state velocity increases, when $mV_O^2/\sigma aD_C \approx 1$, motion is no longer quasi-static. Thus, we define the limiting velocity for quasi-static motion V_{qs} as

$$V_{qs} = \sqrt{\frac{\sigma aD_C}{m}}. \tag{3.7}$$

Equation (3.7) indicates that for initial, steady-state velocity $V<V_{qs}$, motion will begin quasi-statically. The velocity V_{qs} is defined in terms of steady-state velocities, and we use it as an upper bound for the quasi-static phase of motion. For σ, a and D_C values consistent with field and laboratory estimates, and taking $m=\rho r$, where ρ is density and r is a relevant fault dimension –such as the nucleation patch radius, V_{qs} is much greater than creep velocities on geologic faults ($<10^{-9}$ m/s). Thus, a fault undergoing interseismic, creep-type motion driven by plate tectonic loading satisfies our condition for quasi-static motion.

Inertia-Dominated Limit

At the onset of inertia dominated motion the friction terms in equation (3.5) are negligible compared to the applied stress and acceleration terms. In this case, the equation for the slip perturbation x, is approximately that of a simple harmonic oscillator, $m\ddot{x}(t) = -Kx(t)$, where $x(t) = x_o \exp(i\omega t)$ with frequency $\omega = \sqrt{K/m}$. We do not consider full dynamic oscillations of the system, but instead are concerned with the velocity at which the frictional terms in equation (3.5) are negligible compared to the inertial ones. Setting the sum of the friction terms in (3.5) to zero, we have $-a\dot{x}(t) / V_O = b\xi(t)V_O / D_C$. Substituting this into equation (3.6) yields the state variable evolution when motion is inertia-dominated:

$$\dot{\xi}(t) = \left(\frac{V_O \xi(t)}{D_C}\right)\left(\frac{b-a}{a}\right). \tag{3.8}$$

From (8), the time scale over which the state variable changes is $T_\xi = a\, D_c/V_o(b\text{-}a)$. On the other hand, the time scale over which velocity changes is $T_m \approx \sqrt{\mathrm{K/m}}$. When the motion is inertia dominated, $T_\xi << T_m$ or, $V_o >> aD_c \sqrt{\mathrm{K/m}}\ (b\text{-}a)^{-1}$. Thus, we define V_{in} as the limiting velocity at which motion first becomes inertia-dominated:

$$V_{in} = \frac{aD_c}{(b-a)}\sqrt{\frac{K}{m}}. \tag{3.9}$$

Note that this relation differs from estimates based on comparison of the natural period of vibration $T \approx \sqrt{m/K}$ with the characteristic friction evolution time D_c/V [e.g., *Rice and Tse*, 1986]. In that case, $V_{in} \approx D_c \sqrt{K/m}$. Since laboratory data generally show $a \approx 2(b\text{-}a)$ the two estimates do not differ greatly. However, equation (3.9) has the feature that for a given stiffness, mass, and characteristic friction distance, inertia-dominated motion is reached earlier when friction exhibits greater velocity weakening and later for cases in which friction increases more strongly upon an increase in velocity (larger a). Thus, our estimate has the advantage that it relates V_{in}, which is closely related to seismic or geodetic

thresholds of observability of earthquake nucleation, with the friction parameters controlling pre-instability behavior and earthquake nucleation.

Preseismic Motion and Validity of the Definition of V_{in}

Figure 3.3 illustrates the development of unstable slip in our model. For $V<V_{in}$, slip is either quasi-static ($V<V_{qs}$) or quasi-dynamic ($V_{qs}<V<V_{in}$). The time at which $V=V_{in}$ marks the end of preseismic slip. To trigger instability, we apply a stress perturbation defined as the ratio of the perturbed stress to the initial stress $\eta=q_o/\tau_o$. The perturbation is applied at $t=0$ after which the load-point velocity is fixed at V_o. Initially, frictional and applied stresses are approximately equal, acceleration is negligible and motion is quasi-static (quasi-static region in Figure 3.3). The onset of quasi-dynamic motion begins when velocity weakening causes friction to fall below the applied stress. In this paper, we refer to inertia-dominated motion ($V>V_{in}$) as seismic or dynamic motion.

To verify our definition of the limiting velocity V_{in}, we check whether our numerical simulations exhibit instability when $V>V_{in}$. Velocity should exceed V_{in} only for simulations in which $K/K_c<1$, i.e. when the conditions for instability are satisfied. Our numerical simulations do not use the linearized equations, but rather solve the full non-linear equations of motion. We vary the ratio K/K_c by varying K for constant values of K_c and its parameters (equation 3.4).

Figure 3.4 shows slip and velocity as a function of time during a set of simulations with varying K/K_c. Here and in the figures that follow, we use non-dimensional slip, time and velocity, $U' = U/D_c$, $T' = tV_o/D_c$, $V' = V/V_o$, respectively, with primes indicating dimensionless variables. In each case, velocity increases at about the same rate until $T'=4\cdot10^{-6}$, after which it increases sharply for $K<K_c$ (Figure 3.4b). For $K>K_c$, V never exceeds V_{in} and slip never becomes dynamic. Note that V_{in} increases with K and thus V_{in} is lowest in the most unstable case. For $K/K_c<1$, V eventually exceeds V_{in} and thus cases

that satisfy the criteria for unstable slip also exhibit dynamic motion according to our definition.

SIMULATIONS

We first present simulations of triggered instabilities on faults undergoing steady, creep-type motion with steady-state friction according to (3.1) and (3.2). In these cases, the question addressed is: under what conditions will a stress change, for example due to a nearby earthquake, trigger instability on a fault driven at steady state. On the other hand, faults may be locked and over-stressed due to time-dependent frictional strengthening. On such faults, triggering may involve speeding an instability that is already slowly growing. To investigate these cases, we also present simulations in which the initial friction is higher than the steady-state value at the initial loading rate.

Parameter ranges

The initial velocity and normal stress for all simulations is $V_o=10^{-9}$ m/s and σ=100 MPa, respectively, chosen to be comparable to geologic slip rates and a nominal effective stress value in the seismogenic region of crustal faults. We use a range of stiffnesses from 1 to 5 GPa/m, corresponding to K/K_c values of 0.2 to 0.9. Mass per unit area m is varied from 10^1 to 10^7 kg/m^2. As we discuss more fully below, the range of m values may be considered to represent either a range of rupture nucleation dimensions r (taking $m=\rho r$ and noting that $K \approx G/r$, where ρ is density and G is shear modulus) or a range of fault zone widths w (taking $m=\rho w$). We use values of the friction constitutive parameters consistent with laboratory data and fault zone modeling estimates: a=0.005 to 0.007, b=0.006 to 0.008 and D_c from $2\cdot10^{-5}$ to $2\cdot10^{-3}$ m. Higher field-based estimates of D_c exist, based on its mechanical interpretation and scaling properties [e.g., *Marone and Kilgore*, 1993], however, our upper limit is fixed by computational time constraints.

Definition of η_{min} and η_{max}

Although the instability criteria $K<K_c$, $(a-b)<0$ must be satisfied in order to achieve dynamic motion (e.g., Figure 3.4), inertia and the initial frictional state also play a role in determining whether slip velocity exceeds V_{in}. Stress perturbations smaller than a critical size $\eta<\eta_{min}$ will not result in dynamic motion because $V_{max}<V_{in}$ and, hence, the transition from preseismic to seismic slip is undefined (case C of Figure 3.5). Case B of Figure 3.5 shows $\eta\approx\eta_{min}$ for which V_{max} just exceeds V_{in}. Larger stress perturbations result in higher maximum velocities and shorter preseismic durations (case A, Figure 3.5). For stress perturbations larger than an upper limit $\eta>\eta_{max}$, the system is immediately unstable with $V>V_{in}$. This occurs when the applied stress jump exceeds the instantaneous friction direct effect, and in this case preseismic slip and duration are zero. Thus, in our simulations we limit the range of stress perturbations to $\eta_{min}<\eta<\eta_{max}$.

RESULTS

System Mass and Stiffness

Figure 3.6 shows normalized velocity and slip vs. time for simulations with the same perturbation η but different masses. A dot marks the point at which motion changes from quasi-dynamic to inertia dominated and thus denotes the end of preseismic slip. Larger m causes longer preseismic duration and smaller preseismic slip (Figure 3.6). This is because for fixed η, acceleration is inversely proportional to mass, and thus for larger masses the velocity is lower during preseismic slip (Figure 3.6b). As a result, slip-dependent evolution of the state variable requires a longer time, leading to slower velocity weakening and a longer preseismic duration T_p (Figures 3.6 and 3.7). In addition, V_{in} decreases as $m^{-1/2}$, so larger m yields dynamic motion at lower velocities (Figure 3.6b and inset to 3.6a), leading to smaller preseismic slip U_p (Figures 3.6a and 3.7). Note that both V_{qs} and

V_{in} are proportional to $m^{-1/2}$, so as mass approaches zero V_{qs} and V_{in} approach infinity, consistent with fully quasi-static motion in this limit.

Preseismic behavior is also a function of stiffness and the degree of instability, via K/K_c. For a range of m, η and K values, Figure 3.7 shows the preseismic duration and slip determined from curves such as in Figure 3.6. At a fixed η, higher stiffnesses yield longer preseismic durations and larger preseismic slips. The parameter η_{min} increases with K/K_c (Figure 3.7), indicating that larger stress perturbations are required to trigger instability when the system is inherently more stable. In addition, η_{min} decreases with increasing mass, which indicates that larger masses require smaller perturbations to trigger instability (Figures 3.6 and 3.7).

Perturbation Size

The size of the stress perturbation controls the initial acceleration and average preseismic velocity, and thus both preseismic slip and duration decrease with increasing η (Figure 3.7). For fixed K/K_c and m, we find a log-linear relationship between T_p and η (Figure 3.7a). As m increases the range of stress perturbations producing preseismic slip decreases (Figure 3.7). This is due to both a decrease in η_{min}, and a faster decrease in η_{max}. The maximum allowed perturbation decreases with higher m, since the instantaneous increase in friction decreases with mass (e.g., Figure 3.2).

Characteristic Slip, D_c

For fixed η, preseismic slip and duration increase with increasing D_c (Figure 3.8). Note that both V_{qs} and V_{in} increase with D_c and that as D_c goes to zero, V_{in} becomes small, and thus motion becomes unstable instantaneously, i.e. U_p and T_p are negligible. The normalized preseismic duration T' is independent of D_c (Figure 3.8a), indicating linear increase in T_p with D_c. Preseismic slip increases more rapidly than linearly with D_c (Figure 3.8b). The effect of D_c on U_p varies with the size of the stress perturbation.

Friction Parameter a (Direct Effect)

We explore the role of the friction direct effect in simulations where we vary a for fixed values of the other parameters, $(a-b)$, σ, η, D_c, K/K_c, and m. Increasing a leads to an increase in the duration and amount of preseismic slip (Figures 3.9 and 3.10). The net stress immediately following the perturbation decreases with increasing a and thus average preseismic velocity decreases (Figure 3.9b). This effect leads to an increase in the preseismic duration (Figure 3.9b), whereas the fact that V_{in} scales as a leads to an increase in preseismic slip (Figure 3.9a). For fixed a, U_p and T_p decrease with η (Figure 3.10). Note that by definition the maximum allowed stress perturbation η_{max} increases with a.

Rate and State Constitutive Formulation

The above simulations use the constitutive formulation in equations (3.1) and (3.2), which we refer to as the Dieterich law. We also consider two other rate and state variable formulations, which we refer to as the Ruina law, [*Ruina*, 1983], and the Perrin-Rice-Zheng law, [*Perrin et al.*, 1995]:

1. Ruina Law

$$\mu = \mu_O + a\ln\left(\frac{V}{V_O}\right) + b\ln\left(\frac{V_O\psi}{D_c}\right) \tag{3.10}$$

$$\dot{\psi} = \left(\frac{V\psi}{D_c}\right)\left(\psi + b\ln\left(\frac{V}{V_O}\right)\right) \tag{3.11}$$

2. Perrin-Rice-Zhang (PRZ) law:

$$\mu = \mu_o + a\ln\left(\frac{V}{V_o}\right) + b\ln\left(\frac{V\psi}{2D_c}\right) \tag{3.12}$$

$$\dot{\psi} = 1 - \left(\frac{V\psi^2}{2D_c}\right). \tag{3.13}$$

These formulations have the same structure as the Dieterich law, but differ in the evolution of the state variable. In the Ruina law the state variable does not evolve at zero velocity, but instead slip is required for the state to evolve. The PRZ law retains Dieterich-type state aging, but uses a modified evolution relation resulting in symmetric friction responses to velocity increases and decreases, as observed in some laboratory experiments. In all three cases, the state variable exponentially approaches steady-state over a characteristic distance D_c (Figure 3.11a). The critical stiffness and limiting velocities for all three laws are identical to those derived above.

For fixed constitutive parameters the PRZ law evolves the fastest, followed by the Ruina and Dieterich laws (Figure 3.11a). Preseismic slip and duration are smallest for the PRZ law, followed by the Ruina and Dieterich laws (Figure 3.11b and c). An approximately log-linear relation between T' and stress perturbation is observed for each law below an upper limit in η that is lowest for the PRZ law (Figure 3.11b). Preseismic slip is largest for the Dieterich law although U_p decreases more rapidly with increasing η in this case.

Locked and Over-stressed Faults

The simulations above start with the fault creeping steadily under steady-state friction. To investigate the effects of over-stressing, such as for a partially- or fully-locked fault that has undergone frictional healing, we start with a higher frictional strength than the steady-state value for a given creep rate. For these simulations, we use the Dieterich friction law. In this case, $d\psi/dt=1$ when the fault is stationary and thus over-stressing corresponds to increasing the initial value of ψ by the interseismic locking time. We studied interseismic times of 10^7s and $3\cdot10^9$s ($\approx$100 years). All other aspects of the simulations were identical to the cases described above, including the initial velocity V_o. For the over-stressed cases, we find lower preseismic duration and slip compared to faults with steady state friction

(Figure 3.12). However, the effect is not large, for example, 100 years of over-stressing results in a reduction in preseismic duration of ≈ 130s for a nucleation patch roughly 4km in radius (m=10^7kg/m^2) with D_c=10^{-2}m and V_o=10^{-9}m/s (Figure 3.12). Over-stressed faults have lower η_{min}, but the minimum stress perturbation capable of triggering seismic slip is still appreciable (Figure 3.12), in contrast to results that do not include inertia [Dieterich, 1986].

DISCUSSION

Our numerical simulations show that the preseismic duration and time to instability decreases with increasing perturbation size. In particular, $log(T_p)$ decreases linearly with the size of the triggering stress perturbation (Figures 3.7, 3.8, 3.10, 3.11 and 3.12). The slope of this decay is fairly constant, $(\Delta\log(T_p)/\Delta\eta)\approx-50$, varying somewhat with friction parameter a (Figure 3.10) and with constitutive formulation (Figure 3.11).

Scaling of Preseismic Duration with Perturbation Size and Aftershock Occurrence Rate

Our model simulates a fault with homogeneous frictional properties and stress conditions. Therefore, for a given set of parameters, it yields a single time to failure for a given stress perturbation. However, our results can be applied to more complex faults if the initial stress is heterogeneous. In that case, a given triggering event will produce a range of stress perturbation sizes and potential nucleation sites. Assuming a uniform distribution of stress perturbations, the number of nucleation sites N triggered by a perturbation $\leq\eta$ is proportional to η, hence $N\propto-\log(T_p)$. This indicates that the rate of triggered events varies inversely with time, $dN/dt\propto 1/T_p$ and thus our relationship between T_p and η is consistent with the well-known inverse relationship between aftershock occurrence rate and time from the mainshock (Omori's law). Our results indicate that over-

stressed regions of the fault may fail earlier than regions driven at the steady-state creep rate and that instability will be delayed in regions for which the friction parameters a and/or D_c are larger, such as those of higher roughness or that contain granular fault gouge [*Marone and Kilgore*, 1993; *Marone and Cox*, 1994].

Our modeling results are also consistent with observations showing that the rate of foreshocks increases rapidly in the days preceding a mainshock [*Jones and Molnar*, 1979; *Jones*, 1984, 1994]. *Jones and Molnar* [1979] presented a model in which foreshocks are generated by static fatigue of contact asperities. They assume that static fatigue is a random process, so that the rate of failure, dN/dt, is proportional to the number of intact asperities, N, and inversely proportional to the average time to failure, T_f. For static fatigue, the time to failure decreases exponentially with differential stress τ: $T_f \propto \exp(-\tau)$ [*Scholz* , 1972]. This is consistent with our relation between preseismic duration and stress perturbation size $-\log(T_p) \propto \eta$ and $dN/dt \propto 1/T_p$, since η determines the differential stress on a given fault patch. Therefore our modeling indicates that cumulative failure of asperities within the nucleation region of an impending earthquake would result in larger stress perturbations and thus progressively higher rates of seismicity. Thus, it appears that the relationship between the time to instability and the size of the perturbation is a general feature of triggered instabilities.

A Model of Nucleation Incorporating Mass

From our numerical simulations, preseismic duration increases with m and both preseismic slip and average velocity decrease with m. In addition, the limiting velocities V_{qs} and V_{in} vary with m. If one takes m as the product of density and a spatial dimension, then the problem of applying these results to faults reduces to a problem of identifying the spatial dimension. For a slipping fault patch, this dimension is the width w perpendicular to the fault plane, $m=\rho w$. Thus, the range of m values considered in our simulations, 10^1

to 10^7 kg/m^2, corresponds to nominal widths of 4 mm to 4 km. This would indicate a simple scaling between w and preseismic duration, however, w is not independent of nucleation dimension. From continuity considerations, w must scale with rupture size $w=r^n$, so that $m=\rho r^n$ where r is fault radius and n is a constant depending on factors such as gouge zone width and microstructure or fault roughness. For example, a scaling between w and r is predicted by the fractal character of fault roughness, since the maximum topographic variation on a slipping patch is proportional to the patch radius [*Brown and Scholz*, 1985; *Power and Tullis*, 1992]. These studies would indicate n=1 to 1.5. Thus, the inertial parameter in our model scales with nucleation zone size.

Nucleation Zone Size. Although our simulations do not explicitly incorporate growth of the nucleation patch, such growth may be considered in the context of stiffness variations, taking $K \approx G/r$. A requirement for instability and seismic slip is $K<K_c$, and since K_c is defined in terms of the constitutive parameters (equation 3.4), the instability condition is assumed to be met by a reduction in the local stiffness surrounding an expanding nucleation patch. Following *Dieterich* [1986], and ignoring for the moment inertial effects, the critical nucleation patch size r_c can be defined in terms of the friction parameters as follows. For a circular patch of radius r, the relationship between the stress drop $\Delta\tau$ and the maximum offset U at the center is, $\Delta\tau=(7\pi/24)(UG/r)$ [*Chinnery*, 1969], where G is the shear modulus. Interpreting $\Delta\tau/U$ as a local stiffness, K varies as r^{-1} $K=(7\pi/24)(G/r)$ [*Dieterich*, 1986]. Therefore, growth of the slipping patch reduces K until the onset of instability, when $K=K_c$, and the minimum patch radius for instability is [*Dieterich*, 1986]:

$$r_c = \frac{7\pi}{24}\frac{G}{K_c}. \tag{3.14}$$

For a quasi-static analysis, without inertia, (3.14) provides a functional relationship between nucleation size and friction parameters. When inertia is included, K_c also depends on m, which from the above discussion, is related to r. However, for reasonable values of

initial fault creep-rates, K_c is approximately independent of m, that is, the inertial term in equation (3.4) is << 1 (of order 10^{-15}). Making this approximation, $K_c \approx 0.1/D_c$ (in units of MPa/m) for σ=100 MPa, V_o=10^{-9} m/s , and $(b-a)$=10^{-3} (equation 3.4), where we note that the scaling between D_c and w suggested by *Marone and Kilgore* [1993] is not included. For a circular fault patch and G=30 GPa, this indicates a range of r_c values from 5 m to 0.5 km for D_c from $2 \cdot 10^{-5}$ m to $2 \cdot 10^{-3}$ m, which is consistent with seismic estimates of nucleation source dimensions.

Quasi-Dynamic Motion

In the context of our model, preseismic slip and duration are determined by both the quasi-static and quasi-dynamic phases of motion (Figure 3.3). However, in nature, quasi-dynamic processes are likely to be much more important for the identification of earthquake nucleation. Seismic and geodetic detectability of nucleation will scale with slip velocity, and thus the limiting velocity V_{in} is a key factor in the interpretation of our results. From equation (3.9), as the patch radius grows, the local stiffness decreases as r^{-1} and the effective mass per unit area increases as r. Thus, V_{in} varies as r^{-1} and as slip progresses toward instability the limiting velocity for dynamic motion decreases.

We can use our above estimates of r_c to estimate V_{in} for a large-scale fault. At the onset of instability when r=r_c, we assume that the width of the fault zone, w, is approximately r_c. Therefore, the effective mass per unit area ranges from 10^4 to 10^6 kg/m^2 for w=r_c of 5 m to 0.5 km. Using these values for m, and setting K=K_c in equation (3.9), V_{in} ranges from $9 \cdot 10^{-3}$ to $8 \cdot 10^{-1}$ m/s. These velocities are reasonable since they are significantly higher than background creep rates on geologic faults (about 10^{-9} m/s) and slightly lower than typical earthquake particle velocities, which involve V>V_{in}.

Minimum Perturbation Size

The parameter η_{min} sets the lowest perturbation for which sliding velocity reaches V_{in}; smaller stress perturbations result in model creep events. In our numerical simulations, η_{min} was determined empirically, however, an analytic solution would allow one to relate fault zone frictional properties to observations of triggered seismicity thresholds [e.g., *Hill et al.*, 1993; *Gomberg and Bodin,* 1994; *Gomberg and Davis*, 1995; *Beresnev and Wen*, 1995]. We derive here an approximate analytic form for η_{min}.

By definition, $V_{max}=V_{in}$ for $\eta=\eta_{min}$. When $V=V_{max}$, state variable evolution is fast relative to velocity changes, and thus Ψ is approximately constant and equal to the steady-state value $\Psi=D_c/V_{in}$. Using this approximation in the constitutive law (equation 3.1), and combining with the equation of motion (3.3), we have (setting $m\ddot{x} = 0$ in equation 3.3),

$$(\eta_{min} - 1)\mu_o \approx -k\left(V_o T_p - U_p\right) + (a-b)\ln\left(\frac{V_{in}}{V_o}\right). \tag{3.15}$$

Taking an initial fault slip rate of $V_o=10^{-9}$ m/s and noting the magnitude of T_p from our simulations: $V_o T_p << U_p$. Thus η_{min} can be written:

$$\eta_{min} \approx 1 + \frac{1}{\mu_o}\left[kU_p + (a-b)\ln\left(\frac{V_{in}}{V_o}\right)\right]. \tag{3.16}$$

This can be simplified further by noting that in the numerical simulations, when $\eta=\eta_{min}$, $U_p/D_c\approx 100$, thus:

$$\eta_{min} \approx 1 + \frac{1}{\mu_o}\left[100kD_c + (a-b)\ln\left(\frac{V_{in}}{V_o}\right)\right]. \tag{3.17}$$

The utility of equation (3.17) is that given a value of η_{min}, for example from estimates of co-seismic static stress changes, one can estimate the fault zone friction parameters and V_{in}. Comparison of the analytic approximations for η_{min} with empirically-derived values from our numerical simulations indicates reasonable agreement (Figure 3.13). The predicted

η_{min} values are given for a range of constitutive parameters, using the numerical preseismic slip values.

Interpretation of η_{min} in Terms of Triggered Seismicity

In the context of slip on large-scale faults, our stress perturbation represents loading by a neighboring earthquake. Observations of triggered seismicity can be used to evaluate η_{min} if η_{min} is interpreted as a static stress (strain) threshold required for nucleation: $\Delta\tau=(\eta_{min}-1)\tau_o=G\varepsilon$ where $\Delta\tau$ is the change in shear stress on the fault, and ε is the elastic strain. Taking τ_o= 60 MPa as a nominal frictional strength at seismogenic depths, nominal η_{min} values from our modeling (1.01-1.05) give stress thresholds of 0.6 to 3 MPa and a strain threshold of $\varepsilon\approx(\eta_{min}-1)(2\cdot10^{-3})$. These stress changes are higher than field estimates ≈0.05 to 0.1 MPa [*Reasenberg and Simpson*, 1992; *Stein et al.*, 1992; *King et al.*, 1994]. This indicates either that our estimate of fault strength is too high, although τ_o would have to be reduced by an order of magnitude, or that η_{min} for crustal faults is significantly lower than the nominal values we obtained, perhaps due to lower effective stiffness than used in the numerical simulations (Figure 3.13d and e).

This comparison is based on static stress perturbations, however recent observations indicate a frequency-dependent strain threshold for seismic triggering [*Gomberg and Davis*, 1995]. We may also compare our results to these observations. In the frequency domain our Heaviside stress perturbation applied at t=0 has a $1/f$ spectrum. Using the above shear stress estimate, the corresponding frequency-dependent strain perturbation is:

$$\varepsilon(f) = \frac{2\cdot10^{-3}(\eta_{min}-1)}{2\pi f} . \qquad (3.18)$$

Although the specific form of (18) is dictated by our assumption of an instantaneous stress perturbation, it has the feature that the threshold triggering strain ε_T is inversely related to perturbation frequency. Equation (3.18) is compared to the observations of Gomberg and

Davis [1995] by assuming that our η_{min} value from static loading applies for all f (Figure 3.14). The static and total strain thresholds of Gomberg and Davis [1995] are derived from observations of triggered seismicity and by a lack of tidal triggering. Their thresholds are inversely proportional to f, with a proportionality constant equivalent to $\eta_{min} \approx 1.0003$. We note that the inverse scaling between ε_T and f is consistent with higher η_{min} for lower f. This may indicate higher effective D_c and/or lower m for lower f.

Using equation (3.17) with $\eta_{min} \approx 1.0003$, we can calculate the ranges of K, $a-b$ and D_c values which would give rise to a threshold close to that of *Gomberg and Davis* [1995] (Figure 3.14). To obtain an η_{min} value consistent with field estimates for D_c and $(b-a)$ (1 mm to 10 cm and $1\text{-}5 \cdot 10^{-3}$), respectively, stiffnesses must be in the range 10^{-1} to 10^{-2} MPa/m (Figure 3.13d and e), which is consistent with geologic faults having low effective stiffness [e.g., Walsh, 1971].

CONCLUSIONS

We investigate the effect of friction parameters, constitutive laws, and inertia on earthquake nucleation through simulations of instabilities in a 1-D model of a homogeneous fault. To trigger instabilities, we use a stress perturbation which corresponds to static stress changes due to nearby earthquakes. Preseismic motion consists of two distinct phases: quasi-static slip when velocity is less than a limiting value, V_{qs}, and quasi-dynamic slip as inertial effects become more important. During dynamic motion, velocity exceeds the limiting velocity for inertia-driven motion, V_{in}. From the equations of motion of the system, we obtain quantitative definitions and estimates of these velocities for crustal faults: $V_{qs} > 10^{-9}$ m/s and $V_{in} \approx 10^{-3}$ to 10^{-1} m/s. In the context of our modeling, the amount and duration of preseismic slip are governed by fault frictional properties, stiffness and inertia. The preseismic duration scales directly with mass, and the amount of preseismic slip

decreases with mass. Both the amount and duration of preseismic slip increase with the ratio of system stiffness to a critical stiffness and the friction constitutive parameters a and D_c. For a wide range of parameters, we find a log-linear relationship between preseismic duration and the stress perturbation. This result is consistent with empirically observed relationships between the rate of aftershock (or foreshock) occurrence and time since (or prior to) the mainshock [*Jones and Molnar*, 1979], and with simulations of instabilities in systems without inertia [*Dieterich*, 1986]. In contrast to purely quasi-static analysis, our modeling indicates that triggered instabilities require a minimum static stress threshold, which depends on the system stiffness and constitutive parameters. We find that the stress threshold decreases, and preseismic slip and duration are longer for an initially locked and over-stressed fault. In order to match field-based observations of stress thresholds for triggered seismicity, we require fault stiffnesses of order 10^{-1} to 10^{-2} MPa/m.

ACKNOWLEDGMENTS

We are grateful to R. Abercrombie, J. Gomberg and N. Sleep for thorough reviews and suggestions. We also thank T. Jordan and J. R. Rice for discussions during the early stages of this study. This work was supported by NSF grant EAR-9316082.

REFERENCES

Abercrombie, R. and J. Mori, Local observations of the onset of a large-earthquake: 28 June 1992 Landers, California, *Bull. Seism. Soc. Am.*, 84, 725-734, 1994.

Baumberger, T., Heslot, F., and B. Perrin, Crossover from creep to inertial motion in friction dynamics, Nature, 367, 544-546, 1994.

Beeler, N. M. and T. E. Tullis, Implications of Coulomb plasticity for the velocity dependence of experimental faults, submitted to *Pure Appl. Geophys.* 1994.

Beresnev, I. A. and K. L. Wen, Remotely triggered seismicity inferred from Taiwan regional catalog, *Geophys. Res. Let., 22,* 3155-3158, 1995.

Blanpied, M. L., Lockner, D. A., and J. D. Byerlee, Fault stability inferred from granite sliding experiments at hydrothermal conditions, *Geophys. Res. Let., 18,* 609-612, 1991.

Blanpied, M. L., Lockner, D. A, and J. D. Byerlee, Frictional slip of granite at hydrothermal conditions, *J. Geophys. Res., 100*, 13,045-13,064, 1995.

Brown, S. R. and C. H. Scholz, Broad bandwidth study of the topography of natural rock surfaces, *J. Geophys. Res. 90*, 12,575-12,582, 1985.

Chinnery, M., Theoretical fault models, *Pub. Dom.Obs., 37*, Ottawa, 211-223, 1969.

Dieterich, J. H., Time dependent friction in rocks, *J. Geophys. Res., 77*, 3690-3697, 1972.

Dieterich, J. H., Time-dependent friction and the mechanics of stick-slip. *Pure Appl. Geophys.116*, 790-806, 1978.

Dieterich, J. H., Modeling of rock friction: 1. Experimental results and constitutive equations, *J. Geophys. Res.*, *84*, 2161-2168, 1979.

Dieterich, J. H., Potential for geophysical experiments in large scale tests, *Geophys. Res. Lett.*, *8*, 653-656, 1981a.

Dieterich, J. H., Constitutive properties of faults with simulated gouge, in *Mechanical Behavior of Crustal Rocks, Geophysical Monograph 24*, pp. 103-120, Am. Geophys. Union Washington, D. C., 1981b.

Dieterich, J. H., A model for the nucleation of earthquake slip, in *Earthquake Source Mechanics*. AGU Geophysics. mono., *37*, ed. S. Das, J. Boatwright, and C. Scholz, 37-49, 1986.

Dieterich, J. H., Earthquake nucleation on faults with rate and state-dependent friction, *Tectonophys., 211*, 149-178, 1992.

Ellsworth, W. L. and Beroza G. C., Seismic evidence for an earthquake nucleation phase, *Science* , *268*, 851-855, 1995.

Gomberg, J. and P. Bodin, Triggering of the M_S = 5.4 Little Skull Mountain, Nevada, earthquake with dynamic strains, *Bull. Seism. Soc. Am.*, *84,* 844-853, 1994.

Gomberg, J. and Davis, S., Triggered Seismicity in the Geysers Geothermal Area, submitted to *J. Geophys. Res.,* 1995.

Gu, J. C., Rice, J. R., Ruina, A. L. and S. T. Tse, Slip motion and stability of a single degree of freedom elastic system with rate and state dependent friction. *J. Mech. Phys. Sol. 32,* 167-196, 1984.

Gu, Y. and T.-f. Wong, Effects of loading velocity, stiffness, and inertia on the dynamics of a single degree of freedom spring-slider system, *J. Geophys. Res., 96*, 21677-21691, 1991.

Hill, D. P. and others, Seismicity remotely triggered by the magnitude 7.3 Landers, California earthquake, *Science, 260*, 1617-1623, 1993.

Iio, Y., Slow initial phase of the P-wave velocity pulse generated by microearthquakes, *Geophys. Res. Lett., 19*, 477-480, 1992.

Iio, Y., Observations of the slow initial phase generated by microearthquakes: Implications for earthquake nucleation and propagation, *J. Geophys. Res., 100*, 15333-15350, 1995.

Jones, L. M. and P. Molnar, Some characteristics of foreshocks and their relationship to earthquake prediction and premonitory slip on faults, *J. Geophys. Res., 84*, 3596-3608, 1979.

Jones, L. M., Foreshocks (1966-1980) in the San Andreas system, California, *Bull. Seism. Soc. Am., 74,* 1361-1380, 1984.

Jones, L. M., Foreshocks, aftershocks, and earthquake probabilities: accounting for the Landers earthquake, *Bull. Seism. Soc. Am., 84,* 892-899, 1994.

Kato, N., Yamamoto, K. and T. Hirasawa, Microfracture processes in the breakdown zone during dynamic shear rupture inferred from laboratory observation of near-fault high frequency strong motion, *Pure Appl.Geophys.*, *142*, 713-734, 1994.

King, G.C.P., Stein, R.S. and J. Lin, Static stress changes and the triggering of earthquakes, *Bull. Seism. Soc. Am.*, *84,* 935-953, 1994.

Linker, M. F. and J. H. Dieterich, Effects of variable normal stress on rock friction: observations and constitutive equations, *J. Geophys. Res*, *97*, 4923-4940, 1992.

Marone, C. and C. H. Scholz, The depth of seismic faulting and the upper transition from stable to unstable slip regimes, *Geophys. Res. Lett., 15*, 621-624, 1988.

Marone, C., C. B. Raleigh, and C. H. Scholz, Frictional behavior and constitutive modeling of simulated fault gouge, *J. Geophys. Res.*, *95*, 7007-7025, 1990.

Marone, C. and B. Kilgore, Scaling of the critical slip distance for seismic faulting with shear strain in fault zones, *Nature, 362*, 618-621, 1993.

Marone, C. and S. J. D. Cox, Scaling of rock friction constitutive parameters: the effects of surface roughness and cumulative offset on friction of gabbro, *Pure Appl. Geophys., 143,* 359-386, 1994.

Ohnaka, M., and Kuwahara, Y., Characteristic features of local breakdown near a crack-tip in the transition zone from nucleation to dynamic rupture during stick-slip shear failure, *Tectonophys.*, *175*, 197-220, 1990.

Ohnaka, M. and Yamashita, A cohesive zone model for dynamic shear faulting based on experimentally inferred constitutive relation and strong motion source parameters, *J. Geophys. Res.*, *94*, 4089-4104, 1989.

Ohnaka, M., Critical size of the nucleation zone of earthquake rupture inferred from immediate foreshock activity, *J. Phys. Earth, 41*, 45-36, 1993.

Okubo, P. G., and J. H. Dieterich, Effects of physical fault properties on frictional instabilities produced on simulated faults, *J. Geophys. Res., 89*, 5871-5827, 1984.

Perrin, G., Rice J. R., and G. Zheng, Self-healing slip pulse on a frictional surface, submitted to *J. Mech. Phys. Sol.*, 1995.

Power, W. L, and T. E. Tullis, The contact between opposing fault surfaces at Dixie Valley, Nevada, and implications for fault mechanics, *J. Geophys. Res., 97*, 15,425-15,436, 1992.

Reasenberg and Simpson, Response of regional seismicity to the static stress change produced by the Loma Prieta earthquake, *Science, 255*, 1687-1690, 1992.

Reinen, L. A., and J. D. Weeks, Determination of rock friction constitutive parameters using an iterative least-squares inversion method, *J. Geophys. Res. 98*, 15,937-15,950, 1993.

Reinen, L., et. al, The frictional behavior of lizardite and antigorite serpentinites: Experiments, constitutive models and implications for natural faults, *Pure Appl. Geophys*, *143*, 317-358, 1994.

Rice, J. R. and A. L. Ruina, Stability of steady frictional slipping, *J. Appl. Mech., 105*, 343-349, 1983.

Rice, J. R., and J.-C. Gu, Earthquake aftereffects and triggered seismic phenomena, *Pure Appl. Geophys., 121*, 187-219, 1983.

Rice, J. R., and S. T. Tse, Dynamic motion of a single degree of freedom system following a rate and state dependent friction law. *J. Geophys. Res., 91*, 521-530, 1986.

Ruina, A. L., Friction laws and instabilities: A quasistatic analysis of some dry frictional behavior, Ph.D. Thesis, Brown University, 1980.

Ruina, A. L., Slip instability and state variable friction laws, *J. Geophys. Res., 88*, 10359-10370, 1983.

Scholz, C. H., P. Molnar, and T. Johnson, Detailed studies of frictional sliding of granite and implications for the earthquake mechanism, *J. Geophys. Res., 77*, 6392-6406, 1972.

Scholz, C. H., The Mechanics of Earthquakes and Faulting, Cambridge University Press, 1990.

Segall, P. and Rice, J. R., Dilatancy, compaction and slip instability of a fluid infiltrated fault, submitted to *J. Geophys. Res.,100*, 22155-22172, 1995.

Shibazaki, B. and M. Matsu'ura, Spontaneous processes for nucleation, dynamic propagation, and stop of earthquake rupture, *Geophys. Res. Let., 19*, 1189-1192, 1992.

Shibazaki, B. and M. Matsu'ura, Foreshocks and pre-events associated with the nucleation of large earthquakes, *Geophys. Res. Let., 22*, 1305-1308, 1995.

Sleep, N. H., Frictional heating and the stability of rate and state dependent frictional sliding, submitted to *Geophys. Res. Let., 22*, 2785-2788,1995a.

Sleep, N. H., Ductile creep, compaction, and rate and state dependent friction within major fault zones, *J. Geophys. Res., 100,* 13065-13080, 1995b.

Stein R.S., G.C.P. King, and J. Lin, Change in failure stress on the southern San Andreas fault system caused by the 1992 Magnitude = 7.4 Landers earthquake, *Science, 258,* 1328-1332, 1992.

Tse, S. and J. R. Rice, Crustal earthquake instabilities in relation to the depth variation of frictional slip properties, *J. Geophys. Res., 91,* 9452-9572, 1986.

Tullis, T. E., and J. D. Weeks, Constitutive behavior and stability of frictional sliding of granite, *Pure Appl. Geophys., 124,* 383-414, 1986.

Tullis, T. E., Rock friction constitutive behavior from laboratory experiments and its implications for an earthquake prediction field monitoring program, *Pure Appl. Geophys., 126,* 555-588, 1988.

Walsh, J. B., Stiffness in faulting and friction experiments, *J. Geophys. Res., 76,* 8597-8598, 1971.

Weeks, J. D. Constitutive laws for high-velocity frictional sliding and their influence on stress drop during unstable slip, *J. Geophys. Res, 98,* 17637-17648, 1993.

FIGURE CAPTIONS

Figure 3.1. Simple model of a homogeneous fault. An external load is applied to the mass by imposing motion of the load point with velocity V_{load}. The shear stress at the base of the slider τ, is determined by rate and state variable friction laws. At steady-state, the shear stress matches the applied load, and the slider velocity V and the load-point velocity V_{load} are constant and equal. The normal stress σ, is fixed for all simulations at 100 MPa.

Figure 3.2. Friction response for a step increase in slider velocity at time t_1. At times $t<t_1$ friction is at steady-state, $\mu=\mu_o$. The "direct effect" is the immediate jump in μ following the velocity step, and the "evolving effect" is the decay in μ over a slip distance D_c. Velocity weakening frictional behavior, $(a-b)<0$, is shown.

Figure 3.3. Friction (a) and velocity (b) response of the system to a sudden stress perturbation applied at $t=0$.

(a). Friction as a function of slip (solid curve). The dashed line shows the corresponding change in normalized applied force, and the hatchured area shows the resultant normalized force on the slider. The perturbation is followed by an immediate rise in μ and a period of negligible acceleration (quasi-static slip). With further slip, friction decays due to velocity weakening and acceleration begins, (quasi-dynamic slip). We define the onset of dynamic motion when $V=V_{in}$. Acceleration continues until the friction and the applied stress are equal at point X. The absence of non-frictional dissipation, (such as the emission of seismic radiation) means that the energy lost during deceleration is equal to that gained during acceleration (i.e. the shaded areas are equal).

(b). The velocity-time function shows a period of low acceleration at low velocities (quasi-static), before appreciable acceleration occurs (quasi-dynamic). Dashed lines denote

the limiting velocities V_{qs} and V_{in} used to define quasi-static ($V<V_{qs}$), quasi-dynamic ($<V_{qs}<V<V_{in}$), and dynamic motion ($V>V_{in}$). Preseismic slip is defined as slip occurring prior to ($V=V_{in}$).

Figure 3.4. (a). Slip vs. time curves for numerical simulations using identical initial velocities, constitutive parameters and slider masses, hence identical K_c, but differing values of system stiffness, i.e. differing K/K_c. All simulations use η=1.120 and m=10^7 kg/m^2. Inset: The same data at larger scale to illustrate the unstable slip vs. time function when $K/K_c<1$, and stable motion when $K/K_c>1$.

(b). Velocity vs. time curves for the simulations in (a). Dashed lines show V_{in}/V_o. Note that velocity exceeds V_{in} only in cases where $K/K_c<1$, i.e.. when unstable motion is predicted by a linear stability analysis of the equation of motion. Thus, our definition of $V=V_{in}$ as the onset of dynamic motion is consistent with these results.

Figure 3.5. Illustration of minimum and maximum stress perturbations used in simulations. The smallest value of the perturbation, η_{min} is defined as the minimum value required to produce seismic slip, case B. At the maximum value, η_{max}, the applied stress immediately exceeds the friction direct effect, and thus the preseismic slip and duration are zero (case A). Normalized velocity vs. time for three cases illustrate the definition of η_{min}. The maximum velocity for case B just reaches V_{in} and thus the stress perturbation is just large enough to cause dynamic slip. In case A, V_{in} is exceeded, and in case C, V_{in} is never reached. The friction parameters for each case are identical, but the stress perturbations vary, $\eta_A>\eta_B>\eta_C$.

Figure 3.6. Variation of the preseismic phase with mass. These simulations use a=0.006, b=0.007, D_c=$2\cdot10^{-5}$ m, η=1.120 and K/K_c=0.2.

(a). Slip vs. time curves for two different slider masses (in kg/m^2). The dots mark the times at which $V=V_{in}$, and thus motion becomes dynamic. Preseismic slip is lower for larger masses. Inset: Variation of the limiting velocities as a function of mass. Dashed line: V_{qs}/V_o, Solid line: V_{in}/V_o.

(b). Velocity vs. time curves for the simulations in (a). The limiting velocity V_{in} decreases with mass, leading to smaller preseismic slip (a), and longer per-seismic durations.

Figure 3.7. Variation of preseismic slip and duration with mass m, stiffness K, and stress perturbation ratio η. The data are shown for the full range of perturbations, η_{min} to η_{max}. For the parameters used in these simulations, σ=100 MPa, a=0.006, b=0.007, D_c=2·10^{-5} m and initial velocity of 10^{-9} m/s, the critical stiffness is $K_c\cong$5 GPa/m.

(a) *Left panels*: Normalized preseismic duration vs. η. Simulations for a given slider mass are plotted on the same panel. Note that there is a log-linear relation between the duration T_p and η. The slope of this line is roughly independent of mass, $\approx$−50. Duration scales directly with K/K_c, because the degree of instability decreases with increasing K/K_c.

(b) *Right panels*: Normalized preseismic slip vs. η. Preseismic slip scales inversely with η and mass and increases with increasing K/K_c.

Figure 3.8. Preseismic duration (left panels) and preseismic slip (right panels) vs. η for a range of D_c values. (K/K_c is fixed at 0.6 in each case by varying the system stiffness K with other parameters fixed). The normalized duration is independent of D_c, implying that the duration T_p scales with D_c. Preseismic slip U_p increases faster than linearly with D_c.

Figure 3.9. Slip vs. time (a) and velocity vs. time (b) curves for simulations with varying a. The parameters used are D_c=2·10^{-5} m, η=1.080, m=10^7 kg/m^2 and K/K_c=0.6. We use three different values of the parameter a (and change b to keep a–b constant). The dots in (a) indicate the times at which velocity exceeds V_{in} and dynamic motion begins. The dashed lines in (b) indicate V_{in}/V_o. The limiting velocity for dynamic motion, V_{in}, increases with a, as do preseismic slip and duration.

Figure 3.10. Preseismic duration (a) and preseismic slip (b) vs. η for different values of parameter a. For a given stress perturbation, both U_p and T_p increase with a. Note that by definition, η_{max} increases with a because of the increase in the friction direct effect.

Figure 3.11. Comparison among different rate/state variable friction laws. The friction response to a step change in velocity for the laws is determined by the rate of state variable evolution (a). Here the initial steady-state μ and the instantaneous direct effect, are chosen to be the same for all laws. Normalized preseismic duration (b) and normalized preseismic slip (c) are greatest for the Dieterich Law, which has the slowest state evolution, followed by the Ruina and the Perrin-Rice-Zheng laws.

Figure 3.12. Comparison of preseismic slip and duration for faults which are initially creeping under steady-state friction with faults that are initially locked and over-stressed. The simulations use σ=100 MPa, a=0.006, b=0.007, D_c=2·10^{-5} m K/K_c=0.2, m=10^7 kg/m^2 and initial velocity of 10^{-9} m/s. We consider two degrees of over-stressing, corresponding to two intervals over which the fault is locked, 10^7 s and 3·10^{-9} s ≈ 100 y. For fixed perturbation size, normalized preseismic duration (a) and normalized preseismic slip (b) decrease with over-stressing, and are largest for the steady-state case. The

minimum perturbation required for instability, η_{min} decreases with degree of over-stressing, although it remains finite.

Figure 3.13. (a)-(c) Comparison of predicted η_{min} values from equation (3.16) (open circles), with empirically determined values from simulations (solid circles). The solid circles in (a) correspond to η_{min} with fixed stiffness and constitutive parameters but changing mass (data for K/K_c=0.9 in Figure 3.7). In (b) all parameters except the friction parameter a are fixed (data in Figure 3.10). In (c) all parameters except the critical slip distance D_c are fixed (data in Figure 3.8). The friction parameters and preseismic slip U_p used in equation (3.16) to obtain predicted η_{min} correspond to those in the simulations.

(d) and (e) Predicted values of η_{min} from equation (3.17) for a range of stiffnesses K (in MPa/m), with varying friction parameter a (d) and characteristic slip distance D_c (e). The parameter values in (d) are: D_c=0.2 m, b=0.01, σ=100 MPa, m=10^7 kg/m^2. The parameter values in (e) are: a=0.006, b=0.007, σ=100 MPa, m=10^7 kg/m^2. The hatchured lines show field estimates of a co-seismic static stress threshold for triggered seismicity [*Reasenberg and Simpson*, 1992]. Note that to obtain η_{min} values comparable to the field estimates, we would require low effective stiffnesses for a wide range of a and D_c values.

Figure 3.14. (Modified from [*Gomberg and Davis*, 1995]). Comparison of field estimates of earthquake triggering thresholds [*Reasenberg and Simpson,* 1992; *Gomberg and Davis*, 1995], and the spectrum of the lowest threshold obtained from this study ($\eta_{min}\approx$1.01). The frequency dependence of our threshold derives from our assumption of a Heaviside stress perturbation. Our threshold corresponds to a static stress change of ≈0.6 MPa. This is greater than field estimates [*Reasenberg and Simpson,* 1992]), which is consistent with

natural fault zones being more compliant and/or having larger D_c values than in our model calculations.

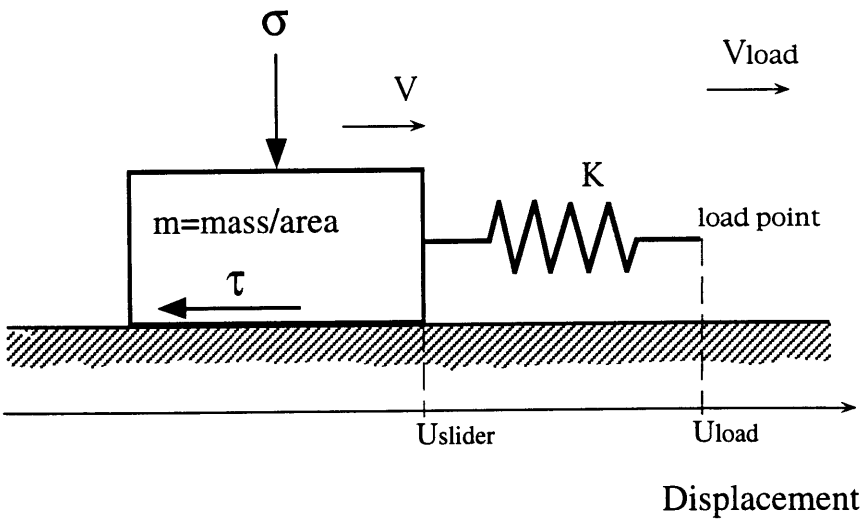
σ
V
Vload
K
m=mass/area
load point
τ
Uslider
Uload
Displacement

Figure 3.1

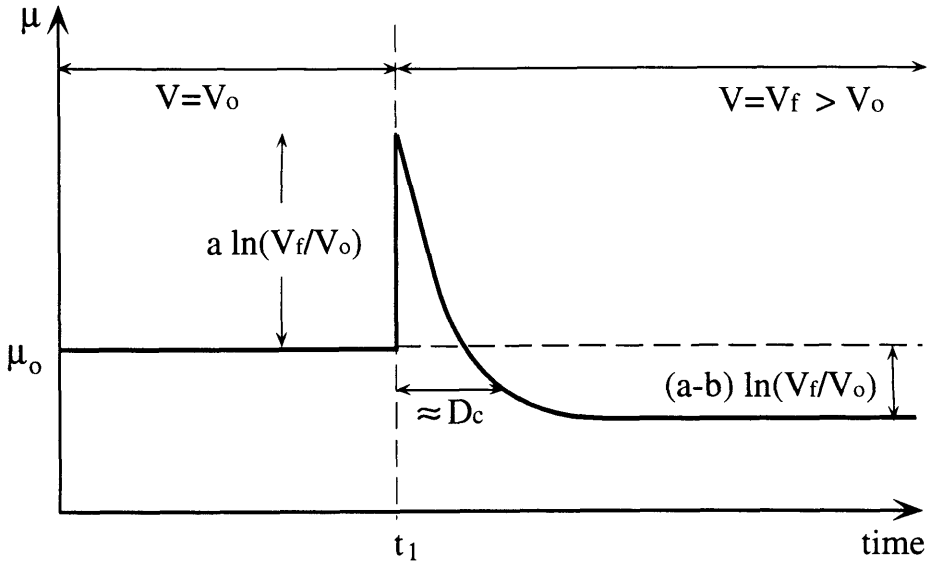

Figure 3.2

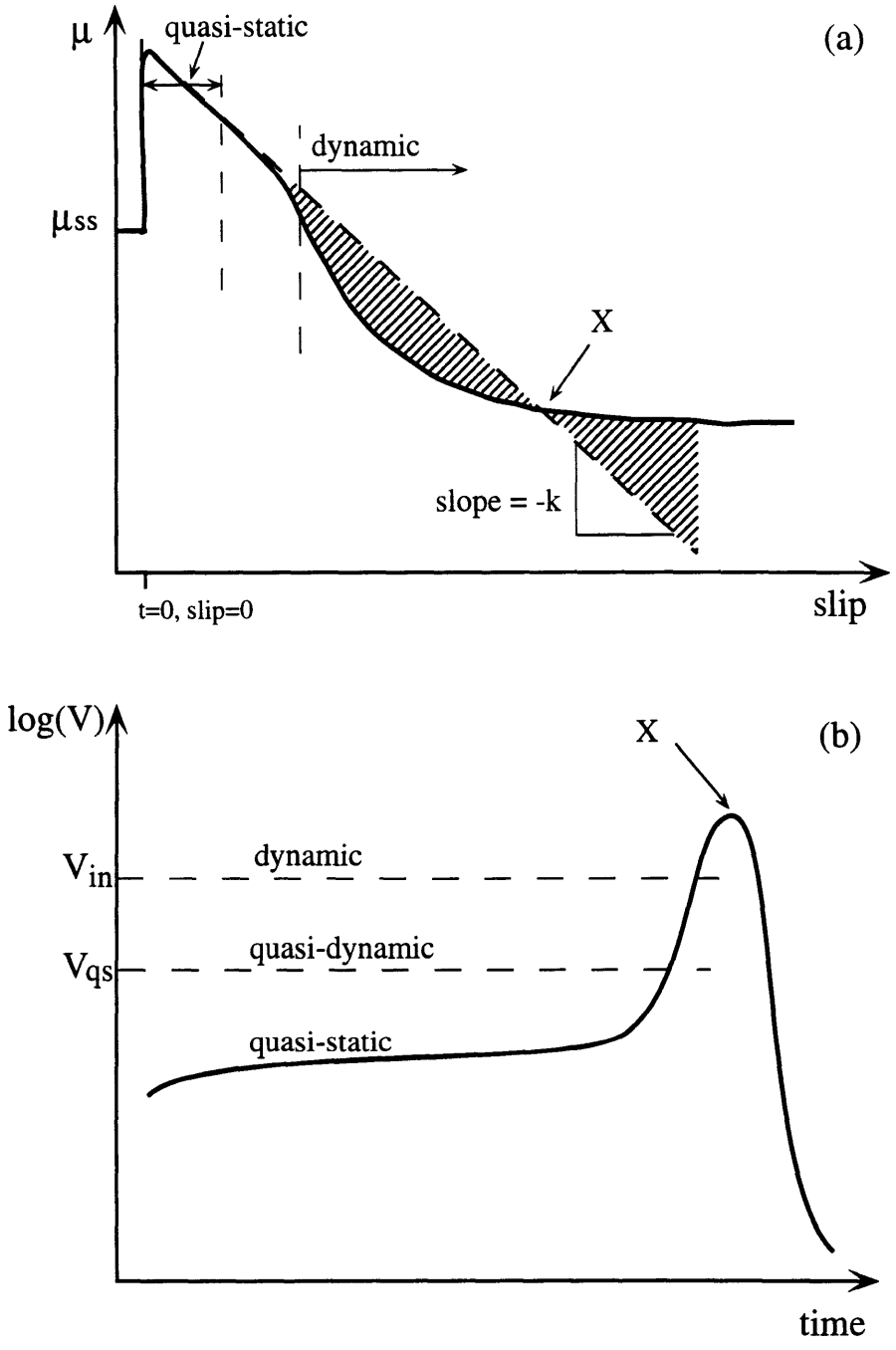
μ
quasi-static
(a)
dynamic
μss
X
slope = -k
t=0, slip=0
slip
log(V)
X
(b)
dynamic
Vin
quasi-dynamic
Vqs
quasi-static
time

Figure 3.3

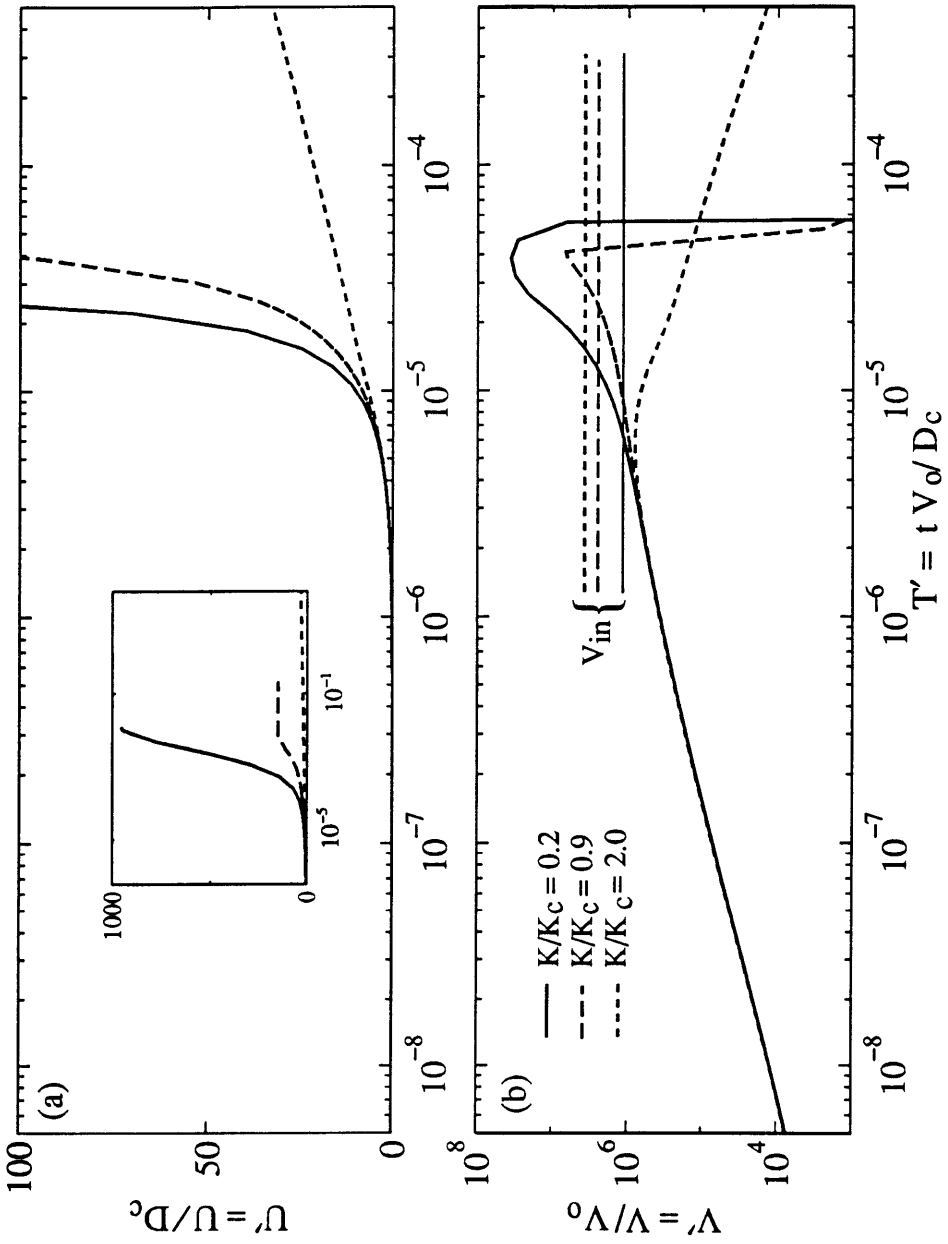
(a)
(b)
U' = U/Dc
V' = V/Vo
T' = t Vo/ Dc
Vin
K/Kc = 0.2
K/Kc = 0.9
K/Kc = 2.0
100
50
0
1000
0
10^-8
10^-7
10^-6
10^-5
10^-4
10^-3
10^-2
10^-1
10^8
10^6
10^4

Figure 3.4

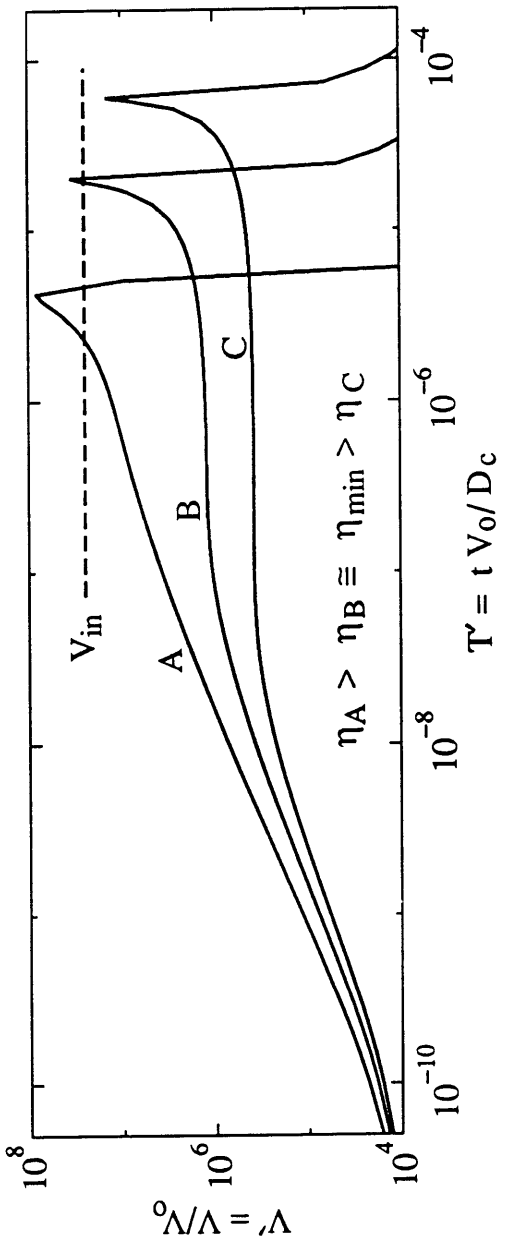
V' = V/V$_o$
10^8
10^6
10^4
10^{-10}
10^{-8}
10^{-6}
10^{-4}
T' = t V$_o$/ D$_c$
$\eta_A > \eta_B \equiv \eta_{min} > \eta_C$
A
B
C
V$_{in}$

Figure 3.5

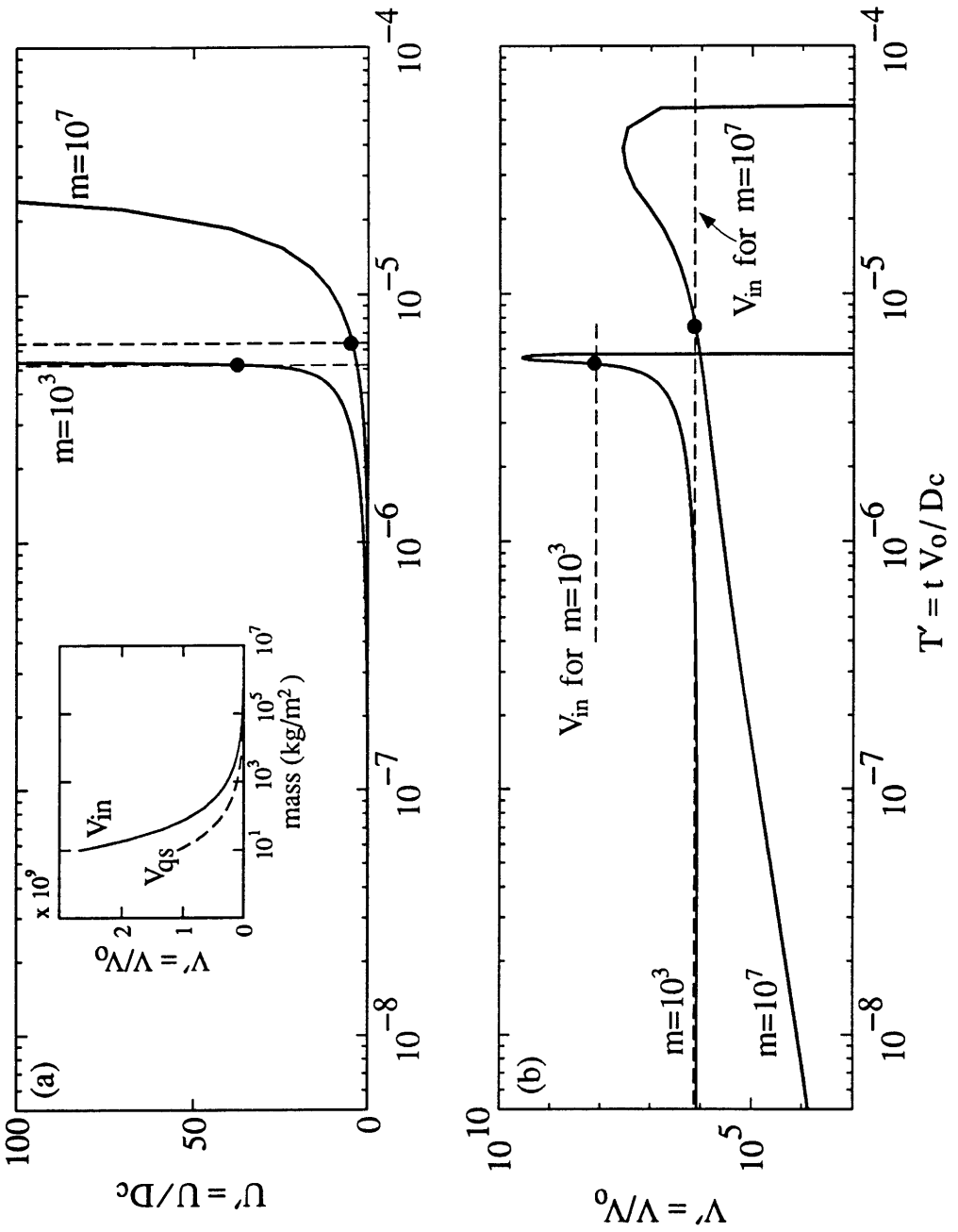
(a)
(b)
m=10^3
m=10^7
V_in for m=10^3
V_in for m=10^7
V_in
V_qs
x 10^9
mass (kg/m^2)
U' = U/Dc
V' = V/Vo
T' = t Vo/Dc

Figure 3.6

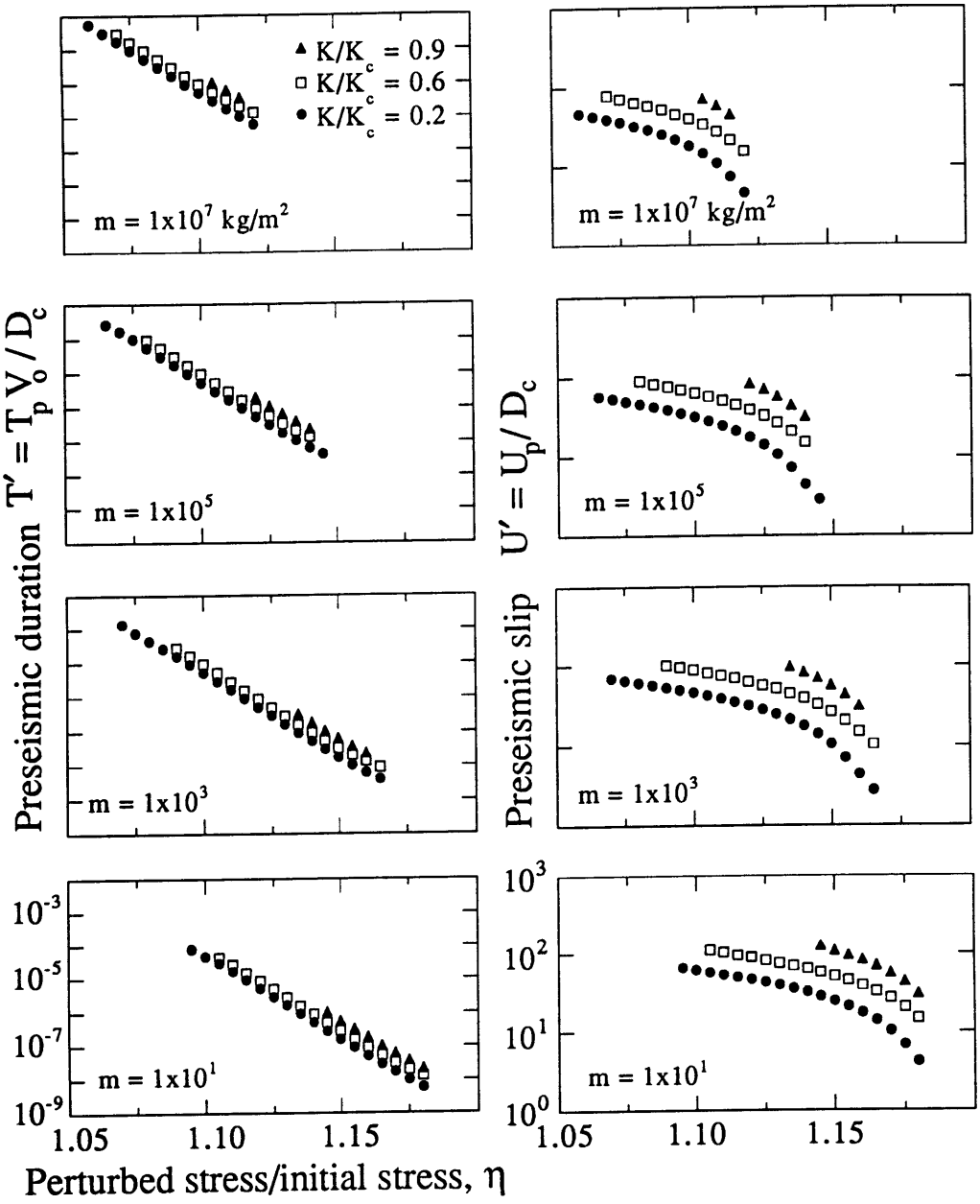
▲ K/K_c = 0.9
□ K/K_c = 0.6
• K/K_c = 0.2
m = 1x10^7 kg/m^2
m = 1x10^7 kg/m^2
m = 1x10^5
m = 1x10^5
m = 1x10^3
m = 1x10^3
m = 1x10^1
m = 1x10^1
Preseismic duration T' = T_p V_o / D_c
Preseismic slip U' = U_p / D_c
10^-3
10^-5
10^-7
10^-9
10^3
10^2
10^1
10^0
1.05
1.10
1.15
1.05
1.10
1.15
Perturbed stress/initial stress, η

Figure 3.7

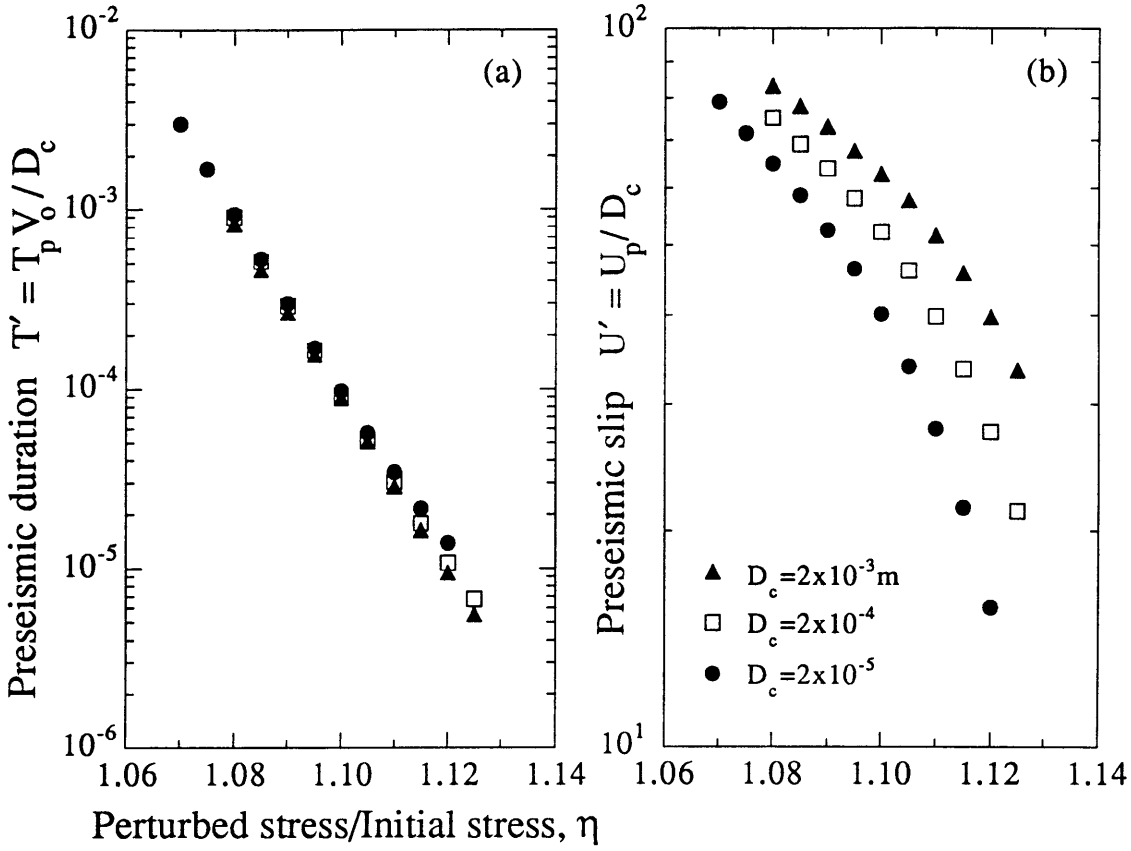
(a)
(b)
Preseismic duration $T' = T_p V_o / D_c$
Preseismic slip $U' = U_p / D_c$
Perturbed stress/Initial stress, η
D_c=2x10^{-3}m
D_c=2x10^{-4}
D_c=2x10^{-5}

Figure 3.8

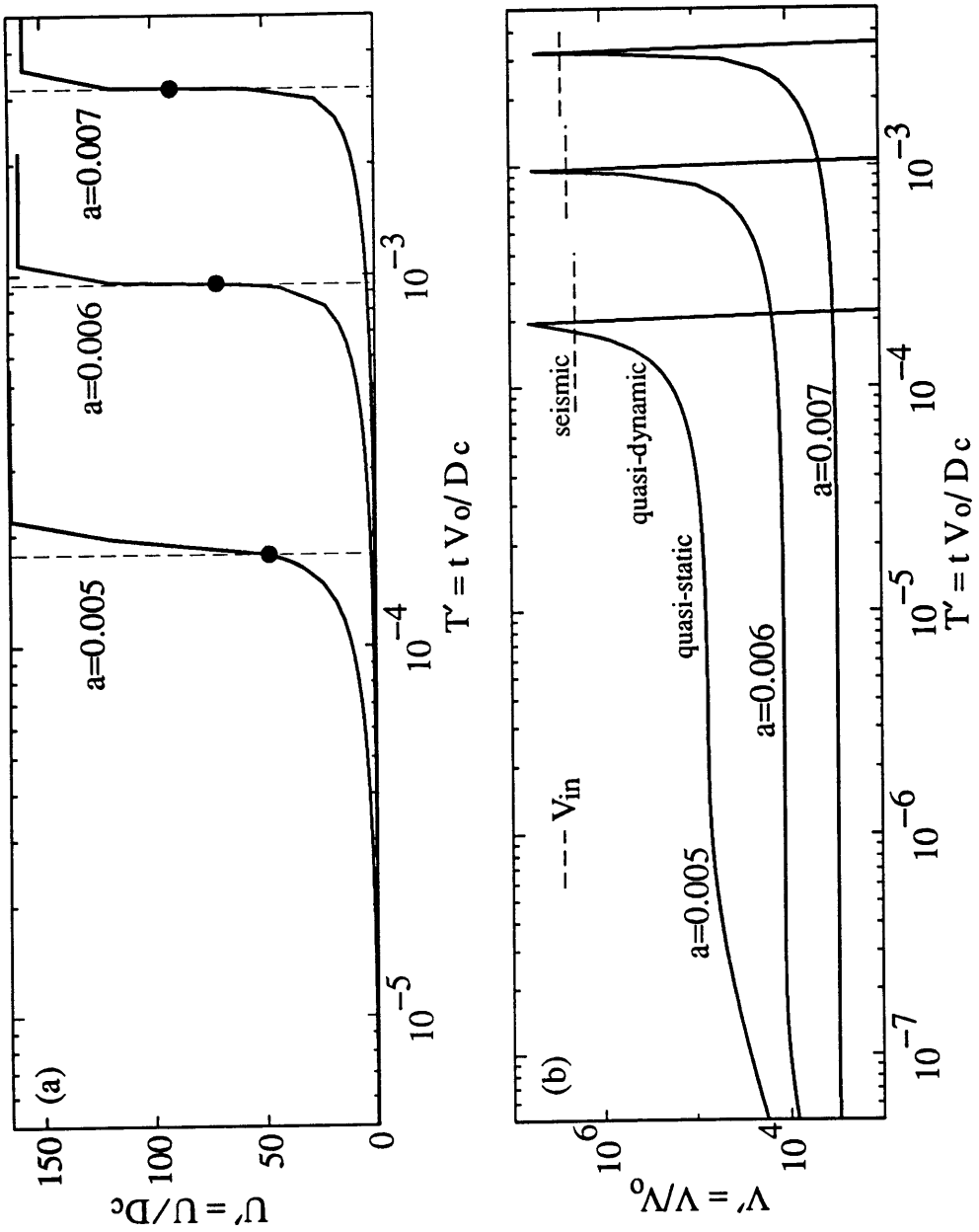
(a)
a=0.005
a=0.006
a=0.007
U' = U/Dc
T' = t Vo/ Dc
(b)
--- Vin
seismic
quasi-dynamic
quasi-static
a=0.005
a=0.006
a=0.007
V' = V/Vo
T' = t Vo/ Dc

Figure 3.9

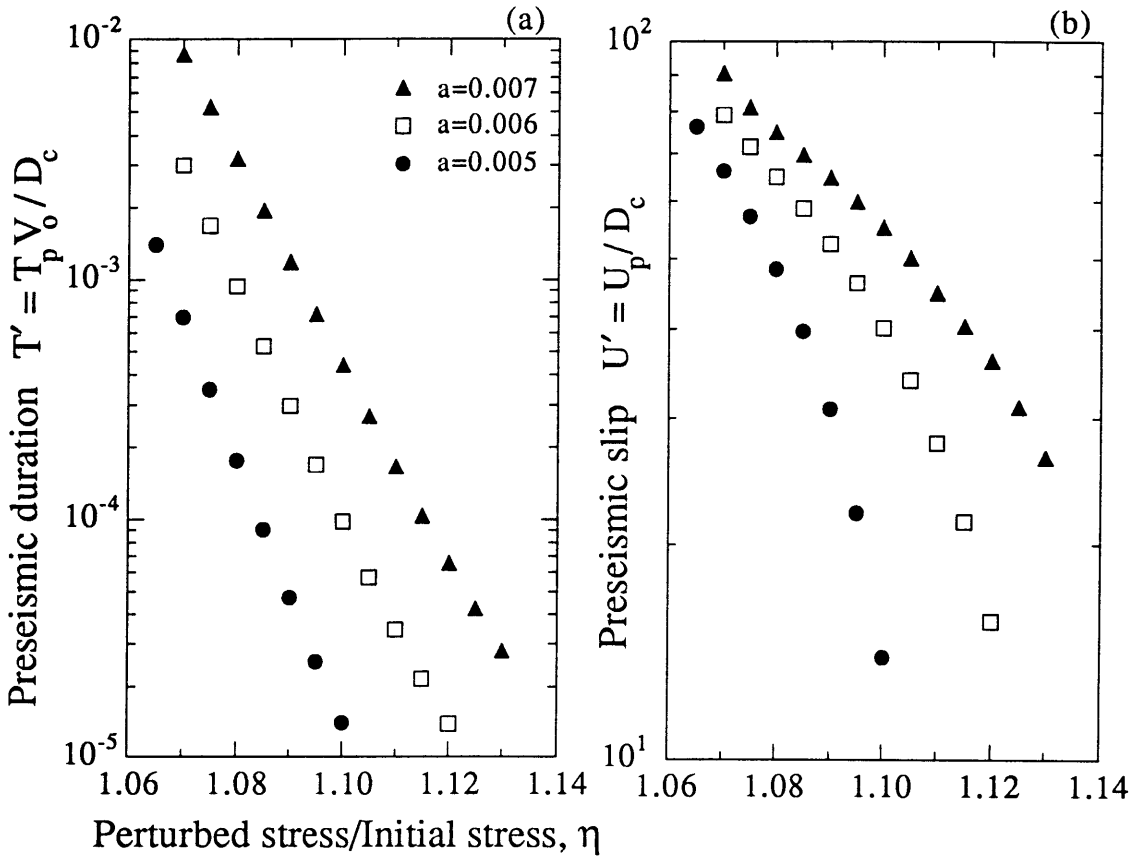
(a)
(b)
a=0.007
a=0.006
a=0.005
Preseismic duration T′ = T_p V_o / D_c
Preseismic slip U′ = U_p / D_c
Perturbed stress/Initial stress, η
10^-2
10^-3
10^-4
10^-5
10^2
10^1
1.06
1.08
1.10
1.12
1.14

Figure 3.10

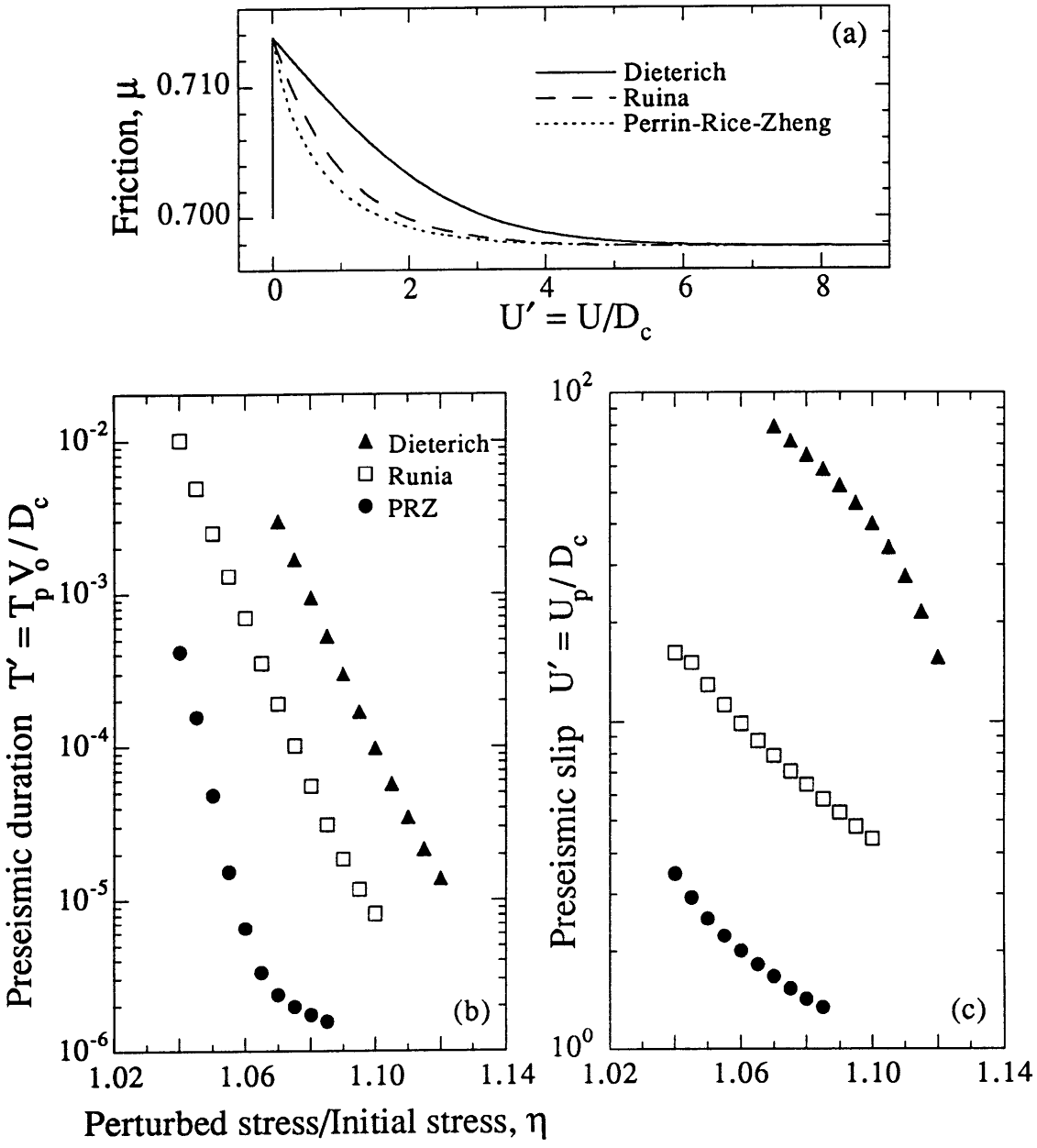
(a)
Dieterich
Ruina
Perrin-Rice-Zheng
Friction, μ
0.710
0.700
0
2
4
6
8
U′ = U/D_c
(b)
Dieterich
Runia
PRZ
Preseismic duration T′ = T_p V_o / D_c
10^-2
10^-3
10^-4
10^-5
10^-6
(c)
Preseismic slip U′ = U_p / D_c
10^2
10^0
1.02
1.06
1.10
1.14
Perturbed stress/Initial stress, η

Figure 3.11

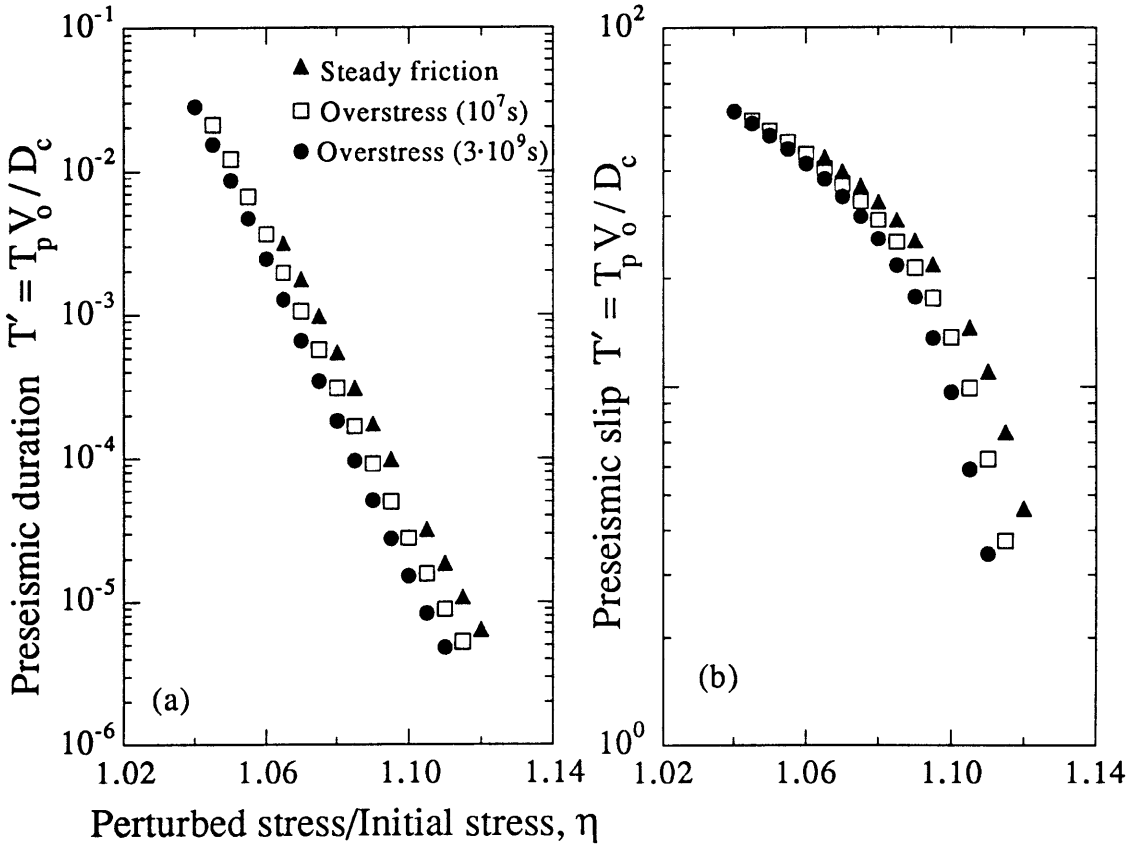
Steady friction
Overstress (10^7s)
Overstress ($3\cdot10^9$s)
Preseismic duration $T' = T_p V_o / D_c$
Preseismic slip $T' = T_p V_o / D_c$
(a)
(b)
10^{-1}
10^{-2}
10^{-3}
10^{-4}
10^{-5}
10^{-6}
10^{2}
10^{0}
1.02
1.06
1.10
1.14
Perturbed stress/Initial stress, η

Figure 3.12

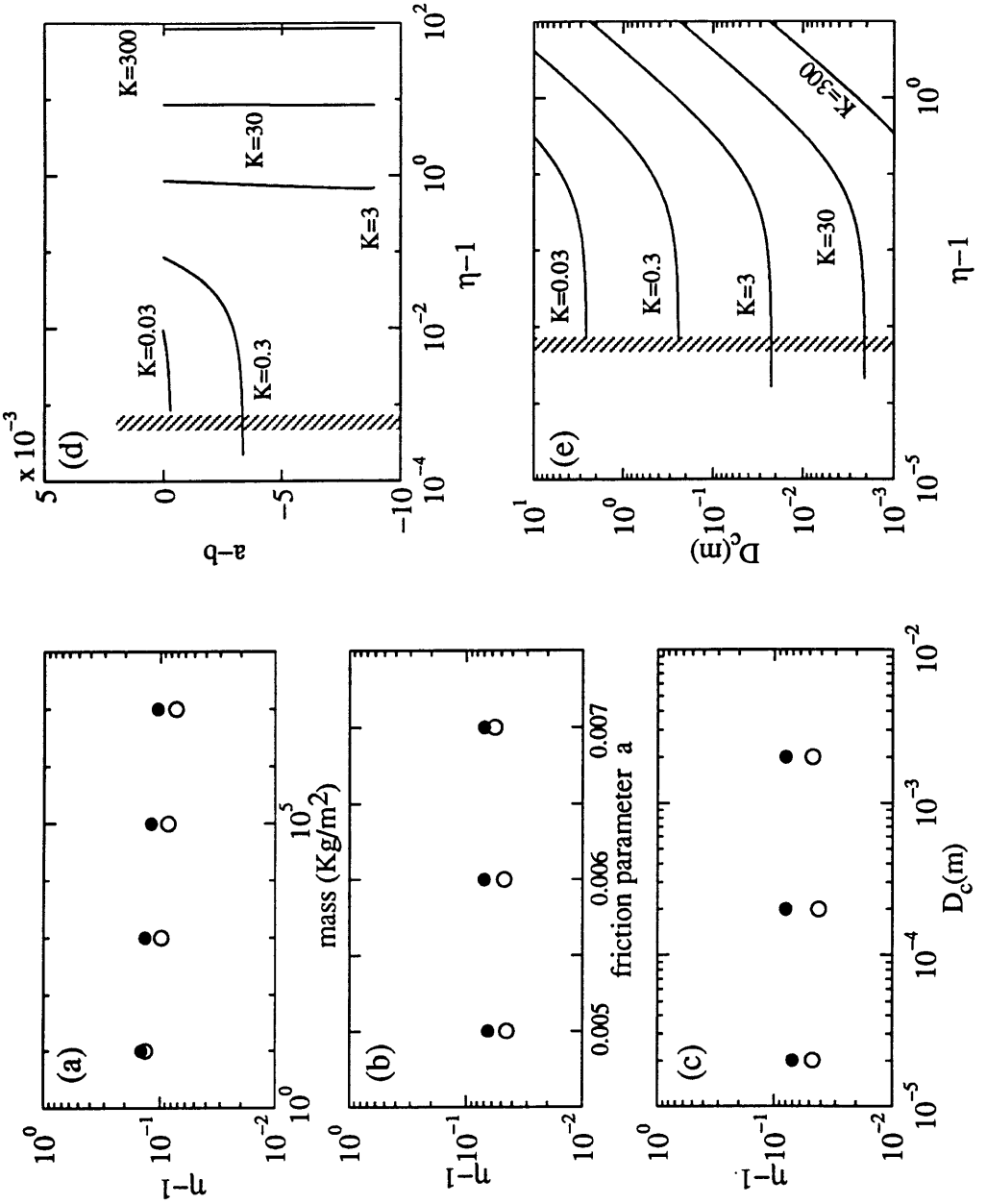
(a)
(b)
(c)
(d)
(e)
η−1
a−b
D_c(m)
mass (10^5 Kg/m^2)
friction parameter a
D_c(m)
x 10^{-3}
K=0.03
K=0.3
K=3
K=30
K=300

Figure 3.13

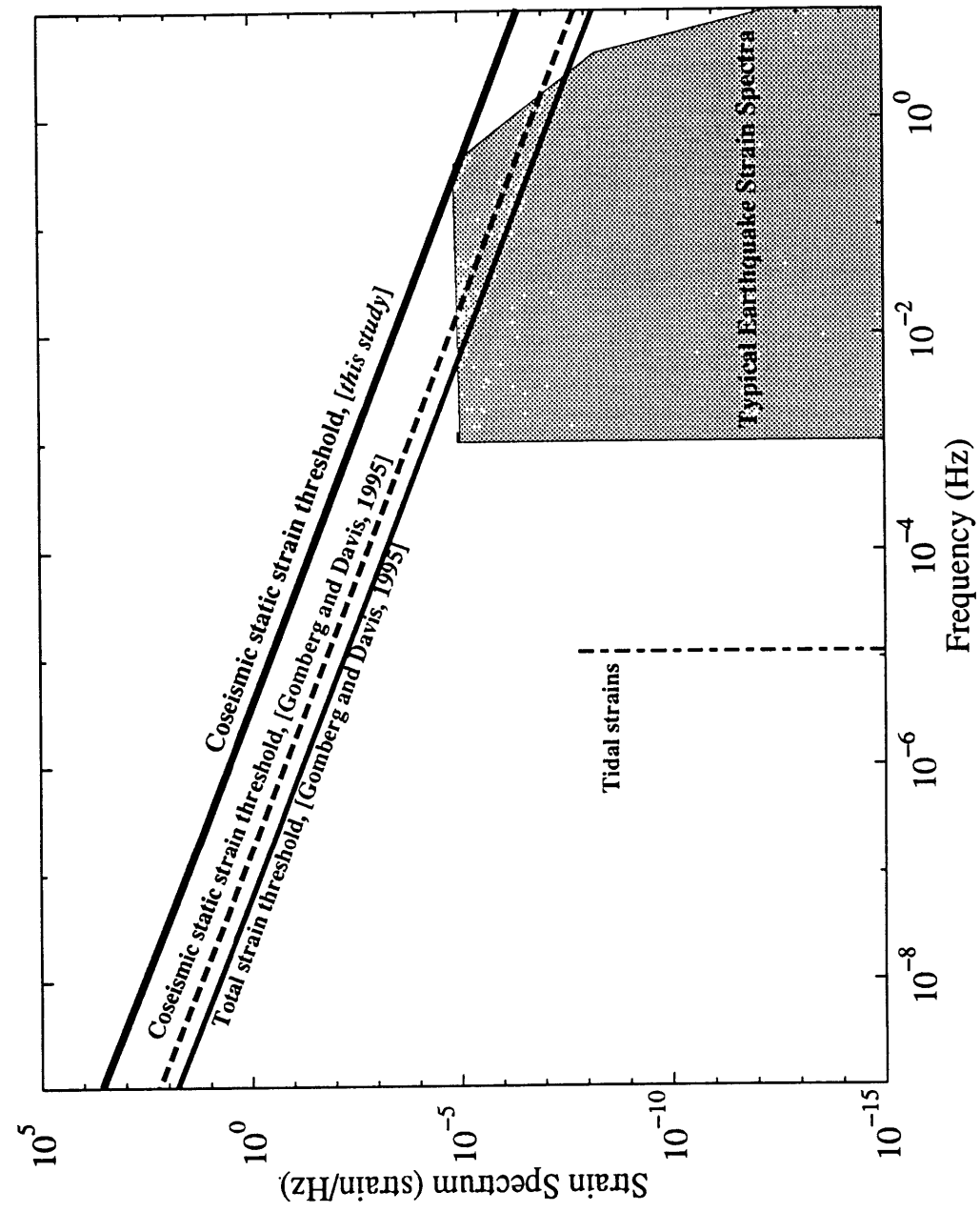
Coseismic static strain threshold, [this study]
Coseismic static strain threshold, [Gomberg and Davis, 1995]
Total strain threshold, [Gomberg and Davis, 1995]
Typical Earthquake Strain Spectra
Tidal strains
Strain Spectrum (strain/Hz)
Frequency (Hz)
10^{5}
10^{0}
10^{-5}
10^{-10}
10^{-15}
10^{0}
10^{-2}
10^{-4}
10^{-6}
10^{-8}

Figure 3.14

Chapter 4

Fault Systems at a Strike-Slip Plate Boundary (1)

ABSTRACT

This is the first of two companion papers investigating the role of continuum crustal rheology in governing deformation at a strike-slip plate boundary. Our main goal is to understand the interaction between continuous deformation and localized brittle failure and how it governs the growth and evolution of large-scale fault networks. We present an analytic model of crustal deformation which consists of a two-layer viscoelastic crust, with uniform shear modulus but depth-varying viscosity, driven by motion of a "plate-like" mantle beneath. Faulting is represented by static elastic dislocations imposed at a critical stress threshold for failure, either fracture of a new fault or sliding on a pre-existing one. Our results suggest that large-scale rheologic stratification within the crust, such as elastic/brittle behavior in the upper crust and viscous flow in the lower crust, places strong controls on the overall morphology of the deformation zone as a function of time and on the growth of fault networks in the upper crust. We show that for a high-viscosity upper crust underlain by a thin, low-viscosity lower crust, the long-term width of the deformation zone scales with a dimensionless parameter which depends on the viscosity contrast and lower crustal thickness. The growth of a large-scale fault network and the width of the region of localized brittle faulting, relative to the total width of the deformation zone, is primarily governed by the strength properties within the upper crust and by the viscosity contrast between the two layers.

INTRODUCTION

Crustal deformation at active plate margins includes localized strain on networks of brittle faults within the upper crust and continuous deformation, both within and across fault-bounded blocks and at lower crustal levels. The interaction between continuous deformation and brittle faulting and its role in governing the evolution and dynamics of networks of large-scale faults is mostly unexplored. However, to understand how surface deformation patterns relate to plate motions, we need to understand this interaction and how it controls stress transmission within the crust.

Previous studies that have modeled deformation around pre-specified fault zones suggest that, over inter-seismic times, strain patterns around faults may be understood as deformation of a continuous elastic or viscoelastic crust (e.g., *Rundle and Jackson*, 1977; *Li and Rice,* 1987; *Lyzenga et al.*, 1991; *Senatorski*, 1995). On the other hand, studies of crustal behavior over geologic times suggest that the long-term behavior of deeper parts of the crust is viscous and may involve large-scale flow in the lower crust (e.g., *Block and Royden*, 1990; *Buck*, 1991). In fact, depending on the time scale of deformation, there is probably a gradual transition from primarily elastic/brittle behavior in the upper crust to viscoelastic and viscous behavior in the lower crust (e.g. *Sibson*, 1984; *Scholz*, 1988).

This study is composed of two companion papers that explore the role of continuum or bulk[1] crustal rheology in the growth, evolution and dynamics of fault networks at a strike-slip plate boundary and the extent to which these processes are a natural outgrowth of crustal rheologic structure. One of our main goals is to understand the complexities of fault dynamics that arise from the interaction of distributed lower crustal flow and upper crustal brittle behavior. For example, could large-scale rheologic stratification of the crust partly govern complex fault dynamics, including basic features such as, growth of

[1] Here "bulk" is used to denote all continuous deformation within unfaulted regions of the crust, rather than just the volumetric strain.

multiple fault networks, aperiodic recurrence times, and stress modulation due to failures on neighboring faults? To what extent does the long-term evolution of a fault network depend on the interaction between upper and lower crustal deformation? We also study the overall morphology of the deformation zone (which includes regions of distributed strain around the plate boundary) and the extent to which it depends on rheologic factors intrinsic to the crust and on length scales of deformation in the mantle.

The first part of our study, the focus of this paper, considers a simple, two-layer viscoelastic (Maxwell) model of the crust for which we analytically solve the equations of motion. By specifying varying viscoelastic properties within the upper and lower crust, we determine the first-order effects of simple strength stratification on deformation at a strike-slip plate boundary. One of the main advantages of the analytic approach is that it allows us to quantify the relationship between the parameters which control crustal rheologic structure and the morphology of the deformation zone. Using the results of the analytic approach as a framework for understanding the basic effects of strength stratification, in the second part (Chapter 5) we set-up a more complex crustal rheologic structure, with a continuous transition from elastic/brittle to viscous behavior, which is solved using a numerical approach.

IDEALIZED BULK RHEOLOGY AND BRITTLE FAILURE

A study of the effects of bulk rheology on the evolution and dynamics of brittle faults requires an idealization of crustal deformation which incorporates continuous behavior at all crustal levels and localized brittle faulting within the upper crust. We choose a viscoelastic rheology for distributed deformation in the crust, which allows simple, linear strain-rate dependence. At time scales that are short compared to the relaxation time (defined as the ratio of viscosity to shear modulus), the crust behaves primarily as an elastic medium and on time scales longer than the relaxation time, behavior is dominantly

viscous. By choosing appropriate values of the viscosity and shear modulus, we allow for dominantly elastic behavior over short (co- and inter-seismic) times and viscous flow over longer (geologic) times. Strength stratification is specified by a depth-dependent relaxation time, for example a long relaxation time in the upper crust and a short one in the lower crust ensures a primarily elastic upper crust and a primarily viscous lower crust.

We model the crust as a two-layer viscoelastic medium overlying a plate-like mantle (Figure 4.1), with uniform shear modulus (μ) and viscosity η_1 in the upper layer of thickness H_1, and viscosity η_2 in the lower layer of thickness H_2 ($H=H_1+H_2$ is the total crustal thickness). The relaxation time in each layer (τ_1 and τ_2) is defined as $\tau_i=\eta_i/\mu$. For simplicity, we assume the plate margin is infinitely long with no variation of properties along strike, thereby reducing the problem to two-dimensions (Figure 4.1). A single, pre-existing strike-slip fault is assumed to coincide with the vertical plane of the plate boundary and the sides of the model region are taken to be far from it, with zero shear stress acting on the edges ($x=\pm L$). Starting from zero initial stresses and strains, we drive crustal deformation by imposing constant velocity at the Moho ($\pm V_0$ on either side of the plate boundary, with a discontinuity at the boundary). (An advantage of choosing a narrow zone of high shear in the mantle is that broadening of the deformation zone within the crust will be due to the rheologic structure of the crust, and will not reflect length scales of deformation in the mantle. This allows us to isolate and focus on the effects of rheologic stratification within the crust.)

Brittle faulting, which occurs over short time scales, is assumed to be a response to stress accumulation within the uppermost crust. We represent discrete faults by static elastic dislocations and incorporate multiple failures assuming that, during faulting, the entire crust away from the fault plane deforms continuously. Individual elastic solutions for multiple faulting events are therefore superposed, so that while one fault fails all others are welded, (i.e. faults rupture independently). (This greatly over-simplifies an

essentially complex problem (see e.g., *Muskhelishvili*, 1954; *Segall and Pollard*, 1980), however, as we are primarily interested in the long-term evolution of fault networks, we ignore short-term complex elastic interactions between faults.) The stress change due to elastic dislocations is added to the pre-failure stresses assuming that faulting does not change the long-term (background) velocity field. Thus, although faulting leads to a sudden stress change and, in a viscoelastic crust, to a decaying perturbation to the stress rate, there are no long-term perturbations to the velocity.

Our idealization of crustal deformation at a strike-slip plate margin is highly simplified and does not consider complexities arising from geometric or compositional heterogeneities and ignores non-linear strain-rate dependent rheology and dynamic rupture propagation. However, it provides sufficient complexity to study the effects of large-scale strength stratification within the crust on the evolution and dynamics of brittle fault networks. In addition to an analytic solution, the simplicity of our model has the advantage of only a few free parameters which determine the rheologic structure of the crust (μ, η_1, η_2, H_1, and H_2), thus restricting the parameter space which needs to be explored. While this model is not specifically applicable to a particular geologic setting, it illuminates the basic controlling factors that determine deformation at strike-slip boundaries in general.

ANALYTIC MODEL OF CRUSTAL DEFORMATION

Continuous Deformation. At an infinite strike-slip plate boundary, non-zero deviatoric shear stresses act on vertical planes parallel to the boundary, σ_{yx}, and on horizontal planes, σ_{yz}, (Figure 4.1b). At equilibrium, these stresses are related to each other by the equation of motion,

$$\frac{d\sigma_{yz}}{dz} + \frac{d\sigma_{yx}}{dx} = 0 \tag{4.1}$$

and to the strain rates through the constitutive equations for a (Maxwell) viscoelastic crust,

$$\mu \frac{dv}{dx} = \dot{\sigma}_{yx} + \frac{\sigma_{yx}}{\tau} \tag{4.2a}$$

$$\mu \frac{dv}{dz} = \dot{\sigma}_{yz} + \frac{\sigma_{yz}}{\tau} \tag{4.2b}$$

where τ is relaxation time and v is velocity parallel to the plate boundary.

Solving the equations of motion of the two-layer viscoelastic crust (equations (4.1) and (4.2)) subject to the boundary conditions described above, we find the velocities and stresses everywhere (see Appendix). The time dependence of the velocities is exponential with an effective relaxation time, $\tau_1 T(k)$, which depends on wavenumber k,

$$T(k) = \frac{\tau_2 \cosh(kH)}{\tau_1 \sinh(kH_1)\sinh(kH_2) + \tau_2 \cosh(kH_1)\cosh(kH_2)}. \tag{4.3}$$

Since μ is fixed ($\tau_1/\tau_2=\eta_1/\eta_2$), $T(k)$ depends only on the viscosity contrast between the two layers and on the thickness of the layers (Figure 4.2). For uniform viscosity $T(k)=1$ so the relaxation time is simply $\tau_1=\tau_2$ and is independent of k, H_1 and H_2. For non-uniform viscosity, the relaxation time is a function of wavelength, $\lambda=2\pi/k$, (Figure4.2). At short wavelengths ($k\rightarrow\infty$), cosh(kx) and sinh(kx) are both $\approx e^{kx}$, so that $T(k)$ approaches the limit $\tau_2/(\tau_1+\tau_2)$, which, for large viscosity reduction between the upper and lower crust, is approximately zero (Figure 4.2). At long wavelengths ($k\rightarrow$ 0), cosh(kx) approaches 1 and sinh(kx) approaches zero, so that $T(k)\rightarrow$ 1 (Figure 4.2).

Width of the deformation zone. The zone of deformation, defined as the region of high strain rates (velocity gradients), is a strong function of the rheologic structure of the crust. As faulting is assumed not to influence the long-term velocity, the growth of the deformation zone as a function of time depends only on the viscosity profile in the crust and on the shear modulus. From the solution for the velocity (equation 4.A3a in Appendix), the steady-state velocity profile at the surface is,

$$\frac{v(x,z,t)}{V_0} = \sum_{n=1,3}^{\infty}\left[\frac{4}{kL}\frac{T(k)}{\cosh(kH)}\right]\sin(kx), \tag{4.4}$$

where the wavenumber, k, is defined as $n\pi/L$.

In a uniform viscosity crust ($T(k)$=1) the surface velocity profile is independent of viscosity and is controlled only by the crustal thickness H and the length scale of deformation in the mantle,

$$v(x) = V_0\left[\frac{4}{\pi}\tan^{-1}\left(e^{\pi x/2H}\right) - 1\right]. \tag{4.5}$$

In fact, for uniform viscosity the initial velocity field at the start of the deformation is also the steady-state velocity (the time-dependent term in equation (4.A3a) is zero when $T(k)$=1). Thus, for a narrow region of high shear in the mantle, the deformation zone at the surface of a uniform viscosity crust is narrow at all times (Figure 4.3a; parameters used here and in following figures are listed in Table 4.1).

In a non-uniform viscosity crust, however, the presence of a weak lower crustal layer (even a very thin one) causes the zone of deformation to widen with time until it reaches steady state (see Figure 4.3b for H_1=H_2=H/2, and Figure 4.3c for H_2<<H_1). When the thickness of the lower crust is small, although the deformation zone still widens with time, the width at any given time is less than that for a thick lower crust (compare Figure 4.3b and 4.3c). This can be understood through the behavior of the effective relaxation time, $\tau_1 T(k)$, in the limit of high viscosity contrast between the upper and lower crust (τ_2<<τ_1). When the two layers are of approximately equal thickness,

$$\frac{T(k)}{\cosh(kH)} \approx \frac{\tau_2/\tau_1}{\sinh^2(kH_1)}, \tag{4.6a}$$

while for a very thin lower crustal layer (H_2<<H_1),

$$\frac{T(k)}{\cosh(kH)} \approx \frac{\tau_2}{\tau_1 H_2} \frac{1}{k \sinh(kH_1)}. \tag{4.6b}$$

Therefore, for fixed viscosity contrast (τ_1/τ_2) and fixed crustal thickness (H), reducing the thickness of the lower crust is equivalent to increasing $T(k)$ and thus increasing the effective relaxation time. The widening of the deformation zone therefore proceeds more slowly (Figure 4.3c). In addition, the long-term velocity profile at the surface is proportional to $T(k)/\cosh(kH)$ (equation 4.4), so reducing the lower crustal thickness increases $T(k)/\cosh(kH)$ and thus the steady-state velocity everywhere. As a result, the steady-state width of the deformation zone decreases as the lower crustal thickness is reduced (Figure 4.4a).

For very thin lower crustal layers, substituting equation (4.6b) in the steady-state velocity (4.4) we see that the velocity scales with $\tau_2/H_2\tau_1$ or, for fixed crustal thickness, with the dimensionless parameter $H\tau_2/H_2\tau_1$. The width of the deformation zone therefore scales inversely with $H\tau_2/H_2\tau_1$, decreasing as this ratio increases (for very thin lower crustal layers this ratio is indicated in parentheses in Figure 4.4a). This scaling relation holds only for very large viscosity contrast and very thin lower crust. For example, for $H\tau_2/H_2\tau_1$=0.03 the scaling relation holds for all values of $H_2 \leq 4$ km ($\eta_1/\eta_2 > 250$), but breaks down for thicker lower crustal layers (Figure 4.4b).

To summarize, the width of the deformation zone in a non-uniform viscosity crust is strongly controlled by the thickness of the lower crustal layer. In addition, as Figure 4.3 shows, the behavior of a non-uniform viscosity crust is fundamentally different than that of a uniform viscosity one, suggesting that there may be a wide spectrum of behavior governed by the amount of viscosity contrast between the upper and lower crust. We investigate this further by studying the long-term surface velocity profile in a crust with varying viscosity contrast, but for simplicity, equal thickness upper and lower layers.

First, consider an elastic upper crust (infinite η_1), underlain by a lower crust which varies from primarily elastic behavior to primarily viscous behavior. When the viscosity of the upper crust is large, $T(k)$ approaches the limit τ_2/τ_1, so that the effective relaxation time is simply $\tau_1 T(k)=\tau_2$ and the steady-state velocity is proportional to τ_2/τ_1 (equation 4.4). Therefore, the relevant rheologic parameter which governs the behavior of an elastic upper crust underlain by a viscoelastic lower crust is τ_2, the ratio of the lower crustal viscosity to the shear modulus. When the lower crust is also elastic (large τ_2) the deformation zone is narrow at all times, as in a uniform viscosity crust (top curve in Figure 4.5a). However, when the lower crustal viscosity is reduced, τ_2/τ_1 decreases so that the steady-state velocity actually approaches zero. This means that at steady-state the velocity profile is flat and the deformation zone is infinitely wide, independent of the lower crustal viscosity. At intermediate times (long compared to τ_2 but short compared to τ_1), the deformation zone width is governed by the viscosity of the lower crust: smaller lower crustal viscosities lead to wider deformation zones (Figure 4.5a).

We now investigate behavior when both the upper and lower crustal layers have intermediate viscosities. In Figure 4.5b, the upper crust has an intermediate relaxation time of 1000 years and the lower crustal behavior varies from primarily viscous (η_1/η_2=1000) to the same as that of the upper crust (η_1/η_2=1). In Figure 4.5c, the lower crustal behavior is primarily viscous, but the upper crust varies from viscous (η_1/η_2=1) to primarily elastic behavior (η_1/η_2=1000). Figures 4.5b and c show that for intermediate viscosities in both the upper and lower crust, the steady-state velocity profile scales simply with the viscosity contrast (curves with the same η_1/η_2 in Figures 4.5b and c are identical).

Brittle Faulting and Co-seismic Slip. We assume that brittle failure is confined to near-surface regions of the crust only and that the depth-extent of faulting, D, is fixed. We

assume that all fault planes intersect the free surface and that stress singularities at the tips of faults can be ignored as long as we are interested in stresses away from the fault plane. To distinguish between fracture of a new fault and sliding on a pre-existing one, we choose a high cohesive strength for fracture (σ_{frac}=50 MPa) and a low value for frictional sliding (σ_{fric}=1 MPa). The frictional shear stress after failure (either fracture of a new fault or sliding on a pre-existing one), is assumed to be a fraction of the shear stress needed to initiate sliding on a pre-existing fault (e.g., we use: $\sigma_{fail}=0.2\sigma_{fric}$ or $0.8\sigma_{fric}$). Therefore, the stress change due to fracture of a new fault is much greater than the stress drop during failure on a pre-existing fault.

At an infinitely long strike-slip boundary the stress orientation ensures that failure near the surface will occur on vertical planes parallel to the boundary, which have the same sense of slip as the plate motions (by symmetry). To solve for the evolution of faulting through time, we superpose the brittle failure criterion on the growth of shear stress on vertical planes (σ_{yx}) near the surface due to tectonic loading (equation 4.A4). Because faulting is confined to depths $0 \le z \le D$, we consider changes in shear stress over these depths in order to determine the occurrence a faulting event. (Note that the symmetry of the plate boundary requires symmetric faulting on either side, $x=\pm x^{dis}$, so we add contributions from both these faults.) The shear stress immediately after a faulting event is a sum of pre-failure stress and the elastic stress change due to faulting (we assume that failure occurs essentially instantaneously, so the medium behaves elastically). A faulting event can therefore be simply incorporated by re-defining the time of failure as t=0, resetting the "initial" stresses (in equation 4.A4) to include the stress change due to faulting (equation 4.A6), and resetting the Fourier coefficient $\tilde{V}_1(k,0)$ in equation (4.A4) to the coefficient just prior to faulting.

Growth of a fault network. Following initial incremental displacements when the velocity boundary conditions are first applied to the base of the crust, stresses at the

surface increase with time (equation 4.A4). Faulting at the main plate boundary occurs when the surface shear stress there exceeds $\sigma_{fric} \approx 1$ MPa (since the depth extent of faulting is taken to be small, the brittle failure criterion is applied to stresses at the surface). After faulting, stresses are relieved around the main plate boundary, but remain high away from it. With continued loading, the stress maximum located off the main fault plane grows (Figure 4.6a) and causes fracture of a new fault parallel to the boundary (provided it grows to reach the fracture criterion, $\sigma_{frac} \approx 50$ MPa, Figure 4.6b). The location of this new fault is primarily governed by the maximum depth of faulting, D (compare Figures 4.6b and 4.6c).

The growth of a fault network clearly depends on stresses within the upper crust reaching high enough values to sustain fracture. With time, the process of fracturing new faults migrates outwards from the plate boundary, until an approximate steady-state is achieved when the rate of stress accumulation due to far-field loading approximately matches the rate of stress reduction via faulting. This places a natural constraint on the upper crustal viscosity. For example, for sufficiently low upper crustal viscosity, even if the viscosity contrast between the upper and lower crust is great (i.e. the steady-state zone of deformation is wide, recall Figure 4.5), faulting may not extend far beyond the plate boundary (Figure 4.7a). In this case, while the region of bulk strain around the plate boundary extends hundreds of kilometers on either side, brittle failure is confined to a narrow zone at the plate boundary.

On the other hand, for very large upper crustal viscosity (primarily elastic behavior in the upper crust) stresses at the surface are greater, and may allow pervasive fracture of new faults away from the plate boundary over a wide zone within the region of high background strain rates (Figure 4.7d). In this case the fracturing process begins by breaking faults successively outwards from the plate boundary at a characteristic spacing (e.g., $\approx 3D$ in Figure 4.8). The stresses on these faults are relieved by repeating failures,

but stresses within the fault-bounded blocks grow with time, until they also reach the fracture criterion at which time the block is sub-divided by a new fault (Figure 4.8d). In a purely elastic upper crust, this process will lead to an indefinite densification of the fault network, limited only by the arbitrary calculation grid spacing. Over long times, the time-averaged behavior of a purely elastic upper crust approaches that of a Coulomb material undergoing failure everywhere. At intermediate values of the upper crustal viscosity, the fracture process competes with a decaying rate of stress growth in the upper crust, leading to a stable, steady-state fault network geometry (Figure 4.7c). Here the zone of brittle faulting is narrower than for an approximately elastic upper crust, but also encompasses many parallel faults.

The failure pattern on faults within the network is governed by a combination of two effects. First, relaxation of the viscoelastic crust leads to a decaying rate of stress growth and thus to a slow, long-term increase in recurrence times. Second, the modulation of stresses on faults due to failures on neighboring fault planes lead to complex temporal variations in recurrence intervals. Stresses on the main fault plane, for example, are modulated by fracture of secondary faults away from the plate boundary and subsequent failures on these faults, which leads to scattered recurrence intervals (Figures 4.7d and 4.9). The primary variable which determines the recurrence intervals in our model is the stress drop during a failure event (compare Figures 4.7a and 4.7b). In our description of brittle failure, we consider events with two kinds of stress drop, large stress drop for fracture and a small one for faulting. This leads to a variable pattern of recurrence times, because stress relief following a large event inhibits faulting around a newly fractured fault (Figure 4.7d and 4.9). At early times during the evolution of the fault network, successive fracture of faults at increasing distances away from the plate boundary lead to long periods of quiescence on the inner faults (Figure 4.9a). The lengths of these periods are proportional to the stress change on the inner faults, which increases with proximity

to the newly fractured fault (Figure 4.9a). At intermediate times during the evolution, the failure pattern is more complicated because of the sub-division of fault-bounded blocks by fracture between two older faults (Figure 4.9b).

Pre-existing faults. An important assumption which influences our results is that the crust around the plate margin is previously unfractured. While this assumption allows a basic understanding of the evolution of stresses in time, it is not likely to be valid in geologic settings where the crust is pervasively fractured, and may contain active faults around the plate margin. To investigate the behavior of our model in this limit, we consider the presence of randomly spaced pre-existing faults within the upper crust. The evolution of the stress profile and migration of stress outward from the plate boundary in this case is determined by the stress drop during faulting, the bulk rheologic structure of the crust, and the spacing of the pre-existing faults themselves.

We study the effect of randomly located pre-existing faults within a relatively high viscosity upper crust underlain by a low viscosity lower crust (η_1/η_2=1000). To investigate how the spacing of pre-existing faults interacts with the "natural" spacing at which the upper crust fractures (e.g. Figure 4.8), we allow neighboring faults to be located at random positions within a range of distances from each other. For example, we first consider a densely pre-fractured crust with randomly located faults with a minimum spacing of D and a maximum spacing of $4D$ (Figure 4.10a). The time evolution of stresses in this case leads to a simple pattern of outward migration of failure initiation, where all faulting is on pre-existing faults and no new faults are fractured (Figure 4.10a and Figure 4.11a). The general pattern of increasing recurrence interval as a function of position away from the plate boundary is due to the decay in background stress rate with distance (Figure 4.11a). If the minimum pre-existing fault spacing is allowed to increase, however, we find that fracture of new faults near the plate boundary occurs when the fault spacing there exceeds $\approx$4 to $6D$ (Figures 4.10b and 4.11b). Far from the plate boundary,

the fault spacing may be much larger without fracturing of new faults because the rate of stress growth decays to zero before stresses within fault-bounded blocks reach the fracture threshold (Figure 4.10b).

DISCUSSION

Time-dependent evolution of the crustal deformation zone at a strike-slip plate boundary is fundamentally controlled by the viscosity contrast between the upper and lower crust. In a uniform viscosity crust, the deformation zone is governed only by the length scale of shear in the mantle and by the crustal thickness. For example, even deformation in a low viscosity crust will be concentrated when strain in the mantle is distributed over a narrow region around the plate boundary. A non-uniform viscosity crust on the other hand, undergoes significant widening of deformation over time scales of 10^5 to 10^6 years depending on the viscosity contrast. (Although the mantle velocity profile we use is highly idealized, these results are qualitatively unchanged for all profiles with concentrated strain rates at the boundary.)

The growth of fault networks within the upper crust is intimately controlled by the viscosity of the upper crust and by the viscosity contrast within the crust, which determines the overall width of the deformation zone. In the presence of a low viscosity lower crust, widening of the deformation zone is accompanied by a widening array of faults in the upper crust. The geometry of the fault network stabilizes as background stress rates decay over time scales governed by the viscosity contrast. In the extreme limit of a purely elastic upper crust, the width of the deformation zone increases indefinitely and fault spacing diminishes without approaching a stable configuration.

Deformation patterns across active fault networks are generally spatially and temporally complex (e.g., *Shen et al.*, 1996), in part due to the inherent complexities of fault structure (e.g., step-overs, jogs and other geometric irregularities) and to material

heterogeneities within the crust (e.g., gouge zones, pore fluids, or differing rock types). Additional complexities arise through the dynamic rupture process, where non-linear, strain-rate dependent rheology may govern both faulting and bulk deformation of regions surrounding faults over co- and post-seismic times. Our results suggest that even in the absence of non-linear rheology, statistical variations in strength and compositional properties, and geometric complexities, simple strength stratification within the crust leads to complex fault evolution and failure histories.

An important limitation of our results is that the evolution of faulting in the model represents only the long-term behavior of the crust and not deformation over short (co- and inter-seismic) times. This is due to the assumption that faulting-related velocity perturbations may be ignored. In a linear viscoelastic crust with faulting confined to the uppermost regions, such perturbations lead to transient variations in stress which decay over time scales comparable to the relaxation time in the upper crust (i.e. over long times). By ignoring these velocity perturbations, we assume that stress transients associated with high strain rates decay over times much shorter than the upper crustal relaxation time, perhaps due to effects not included in our model such as non-linear, strain-rate dependent behavior in the upper crust. While such effects are important when considering post-seismic relaxation following an earthquake, which may occur on time scales as short as 10-100 years (e.g., *Linker and Rice*, 1997, *Turcotte et al.*, 1984), they may not play a large role in the long-term (geologic) evolution of a fault network.

CONCLUSIONS

The results of our analytic model of crustal deformation suggest that continuum rheology places strong controls on the width of the zone of deformation and the long-term evolution of fault networks at a strike slip plate boundary. When the deformation zone within the mantle is narrow, we find that in a crust with uniform strength properties

the surface region of high strain remains narrow throughout the history of the plate boundary. In the presence of a weak lower crustal layer, however, the width grows significantly with time, and is strongly controlled by the strength contrast between the upper and lower crust and the thickness of these layers. The evolution of a network of faults around the main plate boundary is primarily governed by the relaxation time in the upper crust, and also by the strength contrast between the upper and lower crust. Once a system of faults has been fractured, repeating failures over the fault network show complex recurrence patterns due to the modulation of stresses by failures on neighboring faults.

The simplifications in our model allow only very general, broad interpretations of our results, and specific application to a particular plate boundary is necessarily limited. The rheologic signal investigated here is likely to be one part of a complex deformation process, which is strongly influenced by crustal heterogeneities, geometric roughness of faults, non-linear strain rate dependent rheology, time dependent mantle motions, pre-existing weaknesses, etc. The deformation pattern in our model may be made arbitrarily complex, for example by introducing randomly spaced pre-existing faults, random stress drops and frictional or fracture thresholds. While these complexities might influence the failure histories within the fault network, the overall features of the deformation zone, such as its width, time evolution, and growth and development of a fault network would remain strong functions of the bulk rheologic structure.

APPENDIX

Velocities and stresses due to continuous deformation. The equation of motion of the crust at a strike-slip plate boundary (equation 4.1) combined with the constitutive equations for a Maxwell solid (4.2) requires that the velocity satisfies the Laplace equation,

$$\frac{\partial^2 v(x,z,t)}{\partial x^2} + \frac{\partial^2 v(x,z,t)}{\partial z^2} = 0. \tag{4.A1}$$

This equation is solved by assuming that the velocities may be written as Fourier series with time varying coefficients and applying the boundary conditions:

$$\left.\frac{\partial v}{\partial z}\right|_{z=0} = 0 \quad \text{(free surface at } z = 0) \tag{4.A2a}$$

$$\left.\frac{\partial v}{\partial x}\right|_{x=\pm L} = 0 \quad \text{(no strain at edges, } x = \pm \mathrm{L}) \tag{4.A2b}$$

$$v_1 = v_2 \text{ at } z = H_1 \text{ (match velocity at interface)} \tag{4.A2c}$$

$$\sigma_{yz}^{(1)} = \sigma_{yz}^{(2)} \text{ at } z = H_1 \text{ (match stress on interface).} \tag{4.A2d}$$

(Note that the assumption of no strain at the edges of our model is made to simplify the calculations. In the numerical model presented in the second part of this study, Chapter 5, this assumption is relaxed and far-field plate motions are imposed as velocity boundary conditions at the edges.) The velocities are, (a) in the upper layer (for $x \geq 0$)

$$\frac{v(x,z,t)}{V_0} = \sum_{n=1,3}^{\infty} \left[\left(\tilde{V}_1(k,0) - \frac{4}{kL} \frac{T(k)}{\cosh(kH)} \right) e^{-t/\tau_1 T(k)} + \frac{4}{kL} \frac{T(k)}{\cosh(kH)} \right] \cosh(kz)\sin(kx) \tag{4.A3a}$$

(b) in the lower layer, $z' = z - H_1$,

$$\frac{v(x,z,t)}{V_0} = \sum_{n=1,3}^{\infty}\left[\tilde{V}_2(k,t)\frac{\sinh\left(k(z'-H_2)\right)}{\sinh(kH_2)} + \frac{4}{kL}e^{-kz'}\right]e^{kH_2}\sin(kx) \qquad (4.A3b)$$

where

$$\tilde{V}_2(k,t) = \frac{4}{kL} - \frac{\cosh(kH_1)}{e^{kH_2}}\left[\left(\tilde{V}_1(k,0) - \frac{4}{kL}\frac{T(k)}{\cosh(kH)}\right)e^{-\frac{t}{\tau_1 T(k)}} + \frac{4}{kL}\frac{T(k)}{\cosh(kH)}\right], \qquad (4.A3c)$$

where the wavenumber, k, is defined as $n\pi/L$ and $\tilde{V}_1(k,0)$ is the Fourier coefficient of the velocity in the upper layer at time t=0. We assume that when the basal velocities are first applied, the crust undergoes an incremental elastic displacement, which corresponds to $\tilde{V}_1(k,0)=4/kL\cosh(kH)$ (thus at t=0, both velocities and displacements satisfy Laplace's equation). Note that at each faulting or fracture event, we re-define t=0, so the form of $\tilde{V}_1(k,0)$ changes at each failure (as discussed in the text).

Substituting these equations back into the constitutive equations (4.2), we find the stresses within each layer, for example, σ_{yx} in the upper layer as a function of time is,

$$\sigma_{yx}(t) = \sigma_{yx}(0)e^{-t/\tau_1} +$$

$$\mu\sum_{n=1,3}^{\infty}\left[\left(kV_0\tilde{V}_1(k,0) - \frac{4V_0T(k)}{L\cosh(kH)}\right)\left(\frac{\tau_1 T(k)}{T(k)-1}\right)\left(e^{-t/\tau_1 T(k)} - e^{-t/\tau_1}\right)\right]\cosh(kz)\cos(kx) +$$

$$\mu\tau_1\left(1-e^{-t/\tau_1}\right)\sum_{n=1,3}^{\infty}\left[\frac{4V_0T(k)}{L\cosh(kH)}\right]\cosh(kz)\cos(kx). \qquad (4.A4)$$

Elastic dislocations. The analytic expressions for the stresses and displacements within an elastic half-space due to a finite dislocation are derived by *Chinnery*, (1961). Since we ignore deformation in the mantle, we use these expressions with the important restriction that the displacements at the Moho due to faulting should be negligible compared with

displacements due to tectonic loading over one earthquake cycle. For our range of model parameters, this restricts the depth-extent of dislocations to <10 km. The analytic form for the displacements, u^{dis}, and shear stress on planes parallel to the fault, $\sigma_{yx}{}^{dis}$, are (modified from *Chinnery*, 1961, for an infinitely long fault),

$$u^{dis}(x',z)=\frac{U}{2\pi}\left\{\tan^{-1}\left(\frac{x'}{d-z}\right)+\tan^{-1}\left(\frac{x'}{d+z}\right)+\tan^{-1}\left(\frac{x'}{D-z}\right)+\tan^{-1}\left(\frac{x'}{D+z}\right)\right\} \quad (4.A5)$$

and

$$\sigma_{yx}{}^{dis}(x',z)=\frac{\mu U}{2\pi}\left\{\left(\frac{d-z}{(d-z)^2+x'^2}\right)+\left(\frac{d+z}{(d+z)^2+x'^2}\right)-\left(\frac{D-z}{(D-z)^2+x'^2}\right)-\left(\frac{D+z}{(D+z)^2+x'^2}\right)\right\}, \quad (4.A6)$$

where $x'=x-x^{dis}$, x^{dis} is the location of the dislocation, z is depth below the surface, d and D are the burial depth and maximum depth of the fault, respectively, U is the slip on the fault, and μ is the shear modulus. In all calculations we assume that faults intersect the free surface, so d=0.

Table 4.1. Model parameters used in figures[a]

	η_1 (Pa s)	τ_1 (yr)	η_2 (Pa s)	τ_2 (yr)	H_2 (km)	D (km)	$\sigma_{fail}/\sigma_{fric}$
Figures 4.1 to 4.4	*η_1, η_2 etc. listed on the figures*				15	*n/a*	*n/a*
Figure 4.5 (a)[b]	10^{60}	10^{42}	*listed on figure*		15	*n/a*	*n/a*
Figure 4.6	5×10^{23}	5×10^{5}	5×10^{20}	500	15	4 and 8	0.8
Figure 4.7							
(a)	10^{22}	10^{4}	5×10^{19}	50	15	8	0.8
(b)	5×10^{22}	5×10^{4}	5×10^{19}	50	15	8	0.2
(c)	5×10^{22}	5×10^{4}	10^{20}	100	15	8	0.8
(d)	10^{23}	10^{5}	10^{20}	100	15	8	0.2
Figure 4.8	5×10^{22}	5×10^{4}	5×10^{20}	500	15	4	0.8
Figure 4.9	*same as Figure 4.7d*						
Figures 4.10 & 4.11[c]	5×10^{22}	5×10^{4}	10^{20}	100	15	8	0.2

[a] In all calculations: μ=30 GPa (within the range of laboratory-derived values for crustal rocks), V_0=17.5 mm/yr (relative slip rate of 35 mm/yr, consistent with long-term slip rates on the San Andreas fault), and H=30 km.

[b] In Figures 4.5(b) and (c), parameters are listed on figure.

[c] In Figures 4.10 and 4.11, the only difference between (a) and (b) is the range of spacing of pre-existing faults.

REFERENCES

Block L. and L. H. Royden, Core complex geometries and regional scale flow in the lower crust, *Tectonics*, *9*, no. 4, 557-567, 1990.

Buck, R. W., Modes of continental lithospheric extension, *J. Geophys. Res.*, *96*, 20,161-20,178, 1991.

Chinnery, M. A., The deformation of the ground around surface faults, *Bull. Seism. Soc. Am.*, 51, p. 355-372, 1961.

Cohen, S. C., Postseismic viscoelastic surface deformation and stress 1. Theoretical considerations, displacement and strain calculations, *J. Geophys. Res.*, *85*, 3131-3150, 1980.

Donnellan, A., B. H. Hager and R. W. King, Discrepancy between geological and geodetic deformations rates in the Ventura basin, *Nature*, *366*, 333-336, 1993.

Li, V. C. and J. R. Rice, Crustal deformation in great California earthquake cycles, *J. Geophys. Res.*, *92*, 11,533-11,551, 1987.

Linker, M. and J. R. Rice, Models of post-seismic deformation and stress transfer associated with the 1989 Loma Prieta earthquake, *in press*, *U.S. Geol. Surv. Prof. Paper*, *1550-D*, The Loma Prieta, California, Earthquake of October 17, 1989–Postseismic Effects, Aftershocks and Other Phenomena, 1997.

Lyzenga, G. A., A. Raefsky and S. G. Mulligan, Models of recurrent strike-slip earthquake cycles and the state of crustal stress, *J . Geophys. Res.*, *96*, 21,623-21,640, 1991.

Muskhelishvili, N. I., *Some Basic Problems of the Mathematical Theory of Elasticity*, P. Noordhoff Ltd., Groningen, The Netherlands, 1954.

Rundle, J. B. and D. D. Jackson, A three-dimensional viscoelastic model of a strike-slip fault, *Geophys. J. R. Astron. Soc.*, *49*, 575-591, 1977.

Scholz, C. H., The brittle-plastic transition and the depth of seismic faulting, *Geol. Runds.*,77, 319-328, 1988.

Segall, P. and D. D. Pollard, Mechanics of discontinuous faults, *J. Geophys. Res.*, 85, 4337-4350, 1980.

Senatorski, P., Dynamics of a zone of four parallel faults: A deterministic model, *J. Geophys. Res.*, 100, 24,111-24,120, 1995.

Shen, Z. K., D. D. Jackson and B. X. Ge, Crustal deformation across and beyond the Los Angeles basin from geodetic measurements, *J. Geophys. Res.*, 101, 27,957-27,980, 1996.

Sibson, R. H., Roughness at the base of the seismogenic zone: contributing factors, *J. Geophys. Res.*, 89, 5791-5799, 1984.

Thatcher, W., Nonlinear strain buildup and the earthquake cycle on the San Andreas fault, *J. Geophys. Res., 88*, 5893-5902, 1983.

Turcotte, D. L., J. Y. Liu and F. H. Kulhawy, The role of an intra-crustal asthenosphere on the behavior of major strike-slip faults, *J. Geophys. Res., 89*, 5801-5816, 1984.

FIGURE CAPTIONS

Figure 4.1. (a) Schematic geometry of the model dextral strike-slip plate boundary. Imposed mantle velocity boundary conditions at the base of the crust (z=H=30 km) are indicated by the small arrows. The mantle velocity profile is a step function, with V_0=±17 mm/yr on either side of the fault. (Note that in our calculations, the edges of the model, x=±L, are assumed to be much greater than the crustal thickness.) (b) There are only two non-zero shear stresses, σ_{yx} and σ_{yz}, as indicated.

Figure 4.2. The effective relaxation time in the upper crust as a function of wavelength for varying viscosity contrasts between the upper and lower crust (the variable plotted is $T(k)$ in equation (4.3)). For simplicity we have chosen layers of equal thickness, H_1=H_2, but the results are qualitatively unchanged for other geometries. As the viscosity ratio approaches 1 (uniform viscosity crust) $T(k)$ approaches 1, independent of wavelength.

Figure 4.3. Normalized surface velocity profile as a function of position away from the plate boundary (x=0) at various times (indicated) for (a) a uniform viscosity crust, (b) and (c) a low viscosity lower crust. In (b) the upper and lower crustal layers are of the same thickness, whereas in (c) the thickness of the low viscosity lower crust is very small (2 km). The width of the deformation zone for a non-uniform viscosity crust grows with time (b and c), however, the rate of growth is slower for a thinner lower crust (c).

Figure 4.4. (a) Normalized steady-state velocity profile at the surface for fixed upper and lower crustal viscosity (η_1/η_2=1000), but changing lower crustal layer thickness from 1 m to 15 km. For the thinnest lower crustal layers, the value of the dimensionless parameter $H\tau_2/H_2\tau_1$ is indicated by the numbers in parentheses. In (b) we show velocity profiles for varying viscosity contrast (η_1/η_2=10 to 1000)

and lower crustal thickness (H_2=0.1 to 15 km), but keeping the ratio $H\tau_2/H_2\tau_1$ fixed at 0.03. The velocity profiles scale with $H\tau_2/H_2\tau_1$, but only for $H_2 \leq 4$ km, and $\eta_1/\eta_2 \geq 250$.

Figure 4.5. Normalized surface velocity profile as a function of position away from the plate boundary(x=0) at $t=10^4$ years, for a two-layer viscoelastic crust with equal layer thicknesses and: (a) infinite viscosity upper crust η_1 (elastic upper crust) and variable lower crustal viscosity η_2; (b) fixed intermediate value of η_1 and variable η_2; and (c) fixed η_2 and variable η_1. The time at which the profiles are plotted ($t=10^4$ years) is greater than or comparable to the relaxation time in the upper crust in (b) and (c). These two panels thus show steady-state behavior. For the profiles in (a), t is long compared to the lower crustal relaxation time.

Figure 4.6. Time evolution of surface stresses leading to fracture of a secondary fault. While repeated failures occur on the main, plate-bounding fault (x=0), stresses away from the plate boundary grow with time (a) leading to fracture of a new fault (b). In (b), the stress profiles prior to and following faulting are shown, with the dashed vertical line marking the location of the fault. (c) Time evolution of surface stresses leading to fracture of a secondary fault, as in (b), but with a deeper extent of faulting.

Figure 4.7. Evolution of fault networks for varying viscosity structure in the upper crust: (a) and (b) low viscosity, (c) intermediate viscosity, and (d) high viscosity upper crust. In each panel we plot solid circles at points determined by the location (x-axis) and time (y-axis) of faulting events. Overlapping solid circles signify short recurrence intervals and appear as thick lines. Fracture of a new fault is symbolized by open circles. Each panel shows the development of the fault network until approximate steady-state has been achieved (note differences in the time axes, but x-axes are at the same scale). In (a) and (b) the fault network

consists of a single, plate-bounding fault whereas in (c) and (d), the fault network grows to varying steady-state geometries determined by the relaxation time in the upper crust. Panels (a) and (b) show that increasing the stress drop per event increases the recurrence interval of failures. (The brackets to the right of (d) indicate the range of data used in Figure 4.9.)

Figure 4.8. Evolution of surface stresses leading to successive fracture of secondary faults away from the main plate boundary for sufficiently high upper crustal viscosity (a, b, c and d are in temporal order). The solid line in each panel is the stress profile and the dashed vertical lines mark the locations of faults. The characteristic spacing of faults is approximately $3D$. In (a), (b) and (c) the fracture process leads to fracture of new faults successively outwards from the plate boundary, whereas in (d) stress within a fault-bounded block is high enough to fracture a new fault within it (arrow).

Figure 4.9. Detailed failure histories at various stages of evolution of the fault network in Figure 4.7d, for the fault locations indicated to the left of the panels. The thin vertical lines indicate faulting at the normalized time on the x-axis, whereas the thick vertical lines show fracture. In (a) we show the early evolution (t/τ_1=0.2 to 0.5) of the system, with fracture of new faults at successively greater distances from the plate boundary. In (b) (t/τ_1=0.6 to 1.3) the failure histories on inner faults are complicated by fracturing closer in to the plate boundary.

Figure 4.10. Growth of surface shear stress profiles plotted at uniform time intervals ($0.1\tau_1$) for a crust with pre-existing faults at random locations (light dashed lines below the x-axis), but with a specified range of spacings between faults: (a) minimum spacing D and maximum spacing $4D$, (b) minimum spacing $6D$ and maximum spacing $10D$ (D=8 km with grid size $dx=D/2$). Both panels show a decaying rate of stress growth so that initially profiles are spaced far apart

whereas close to steady-state the profiles merge. In (a) all failure occurs on pre-existing faults and the stress minima correspond to the locations of these faults while stress maxima lie roughly mid-way between fault-bounded upper crustal blocks. In (b), however, failure initially occurs only on pre-existing faults, but fracture of two new faults occurs within the first two blocks adjacent to the plate boundary (indicated by heavy arrows and heavy lines below the x-axis).

Figure 4.11. Spatio-temporal failure history for (a) the stress evolution shown in Figure 4.10a and (b) the stress evolution in Figure 4.10b. Solid circles mark faulting events and large open circles (in b) mark fracture at points determined by the location (x-axis) and time (y-axis) of failure.

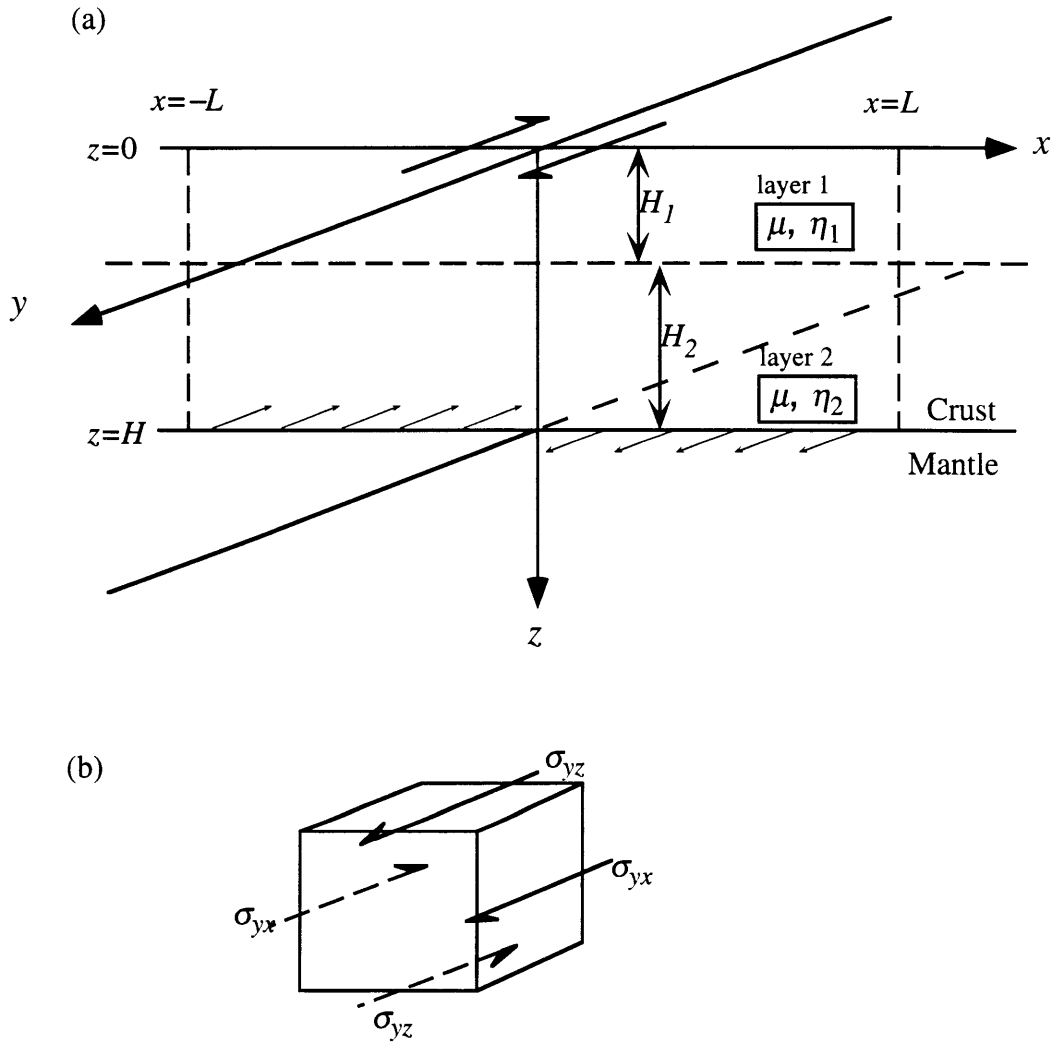
(a)
x=−L
x=L
z=0
x
H1
layer 1
μ, η1
y
H2
layer 2
μ, η2
z=H
Crust
Mantle
z
(b)
σyz
σyx
σyx
σyz

Figure 4.1

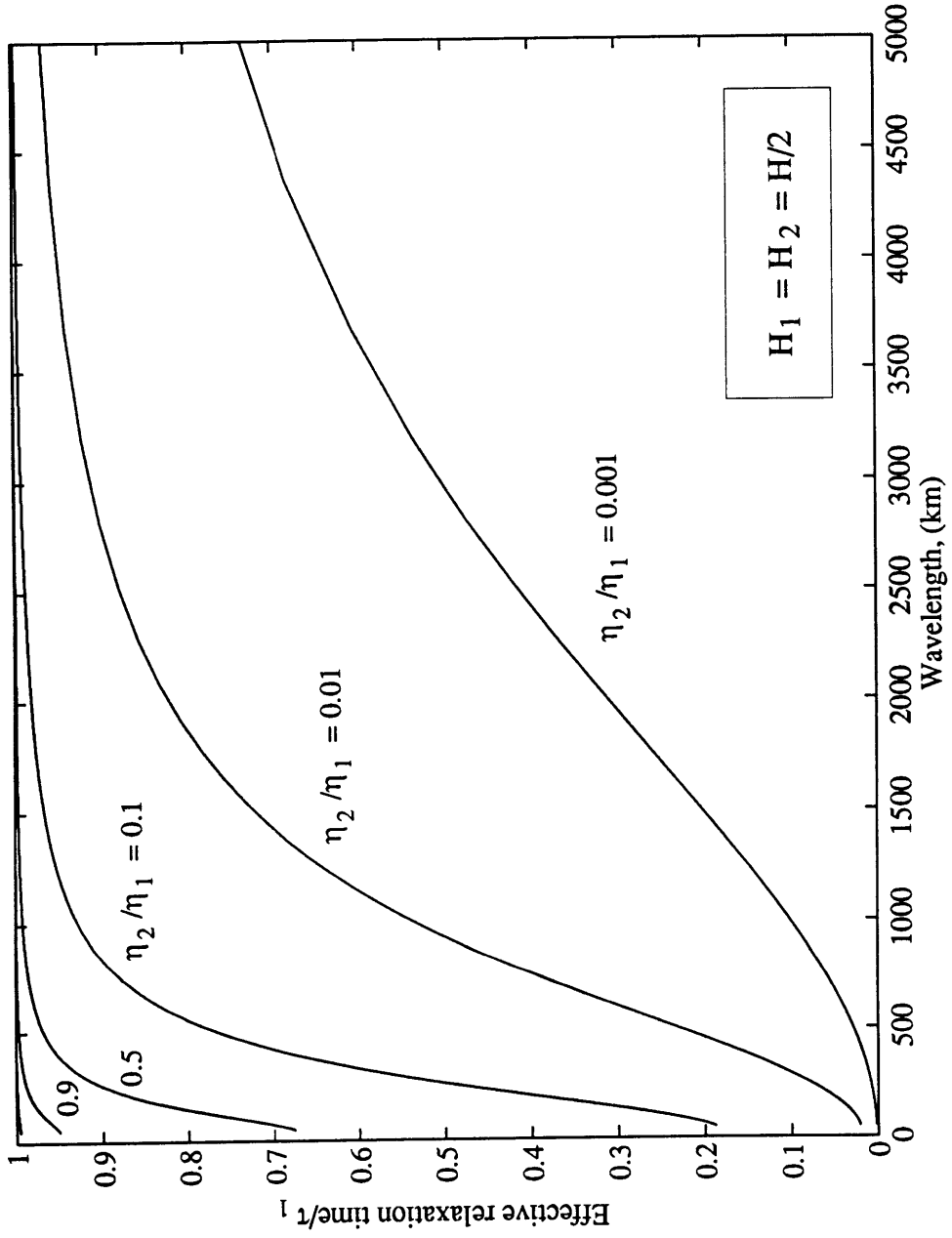
Effective relaxation time/τ 1
Wavelength, (km)
0
500
1000
1500
2000
2500
3000
3500
4000
4500
5000
0.1
0.2
0.3
0.4
0.5
0.6
0.7
0.8
0.9
1
0.9
0.5
η2 /η1 = 0.1
η2 /η1 = 0.01
η2 /η1 = 0.001
H1 = H2 = H/2

Figure 4.2

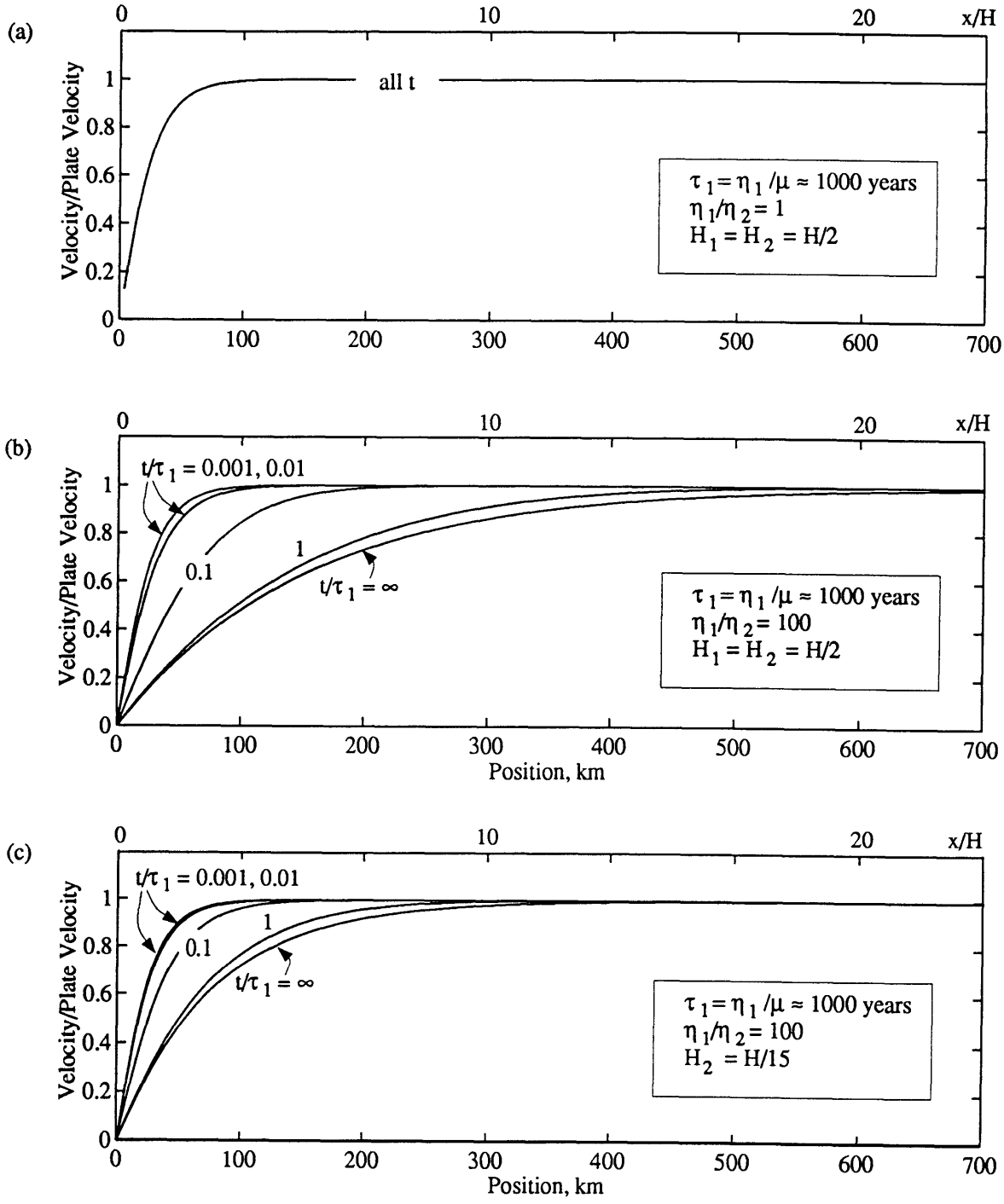
(a)
0
10
20
x/H
Velocity/Plate Velocity
1
0.8
0.6
0.4
0.2
0
all t
$\tau_1 = \eta_1/\mu \approx 1000$ years
$\eta_1/\eta_2 = 1$
$H_1 = H_2 = H/2$
0
100
200
300
400
500
600
700
(b)
$t/\tau_1 = 0.001, 0.01$
0.1
1
$t/\tau_1 = \infty$
$\tau_1 = \eta_1/\mu \approx 1000$ years
$\eta_1/\eta_2 = 100$
$H_1 = H_2 = H/2$
Position, km
(c)
$t/\tau_1 = 0.001, 0.01$
0.1
1
$t/\tau_1 = \infty$
$\tau_1 = \eta_1/\mu \approx 1000$ years
$\eta_1/\eta_2 = 100$
$H_2 = H/15$
Position, km

Figure 4.3

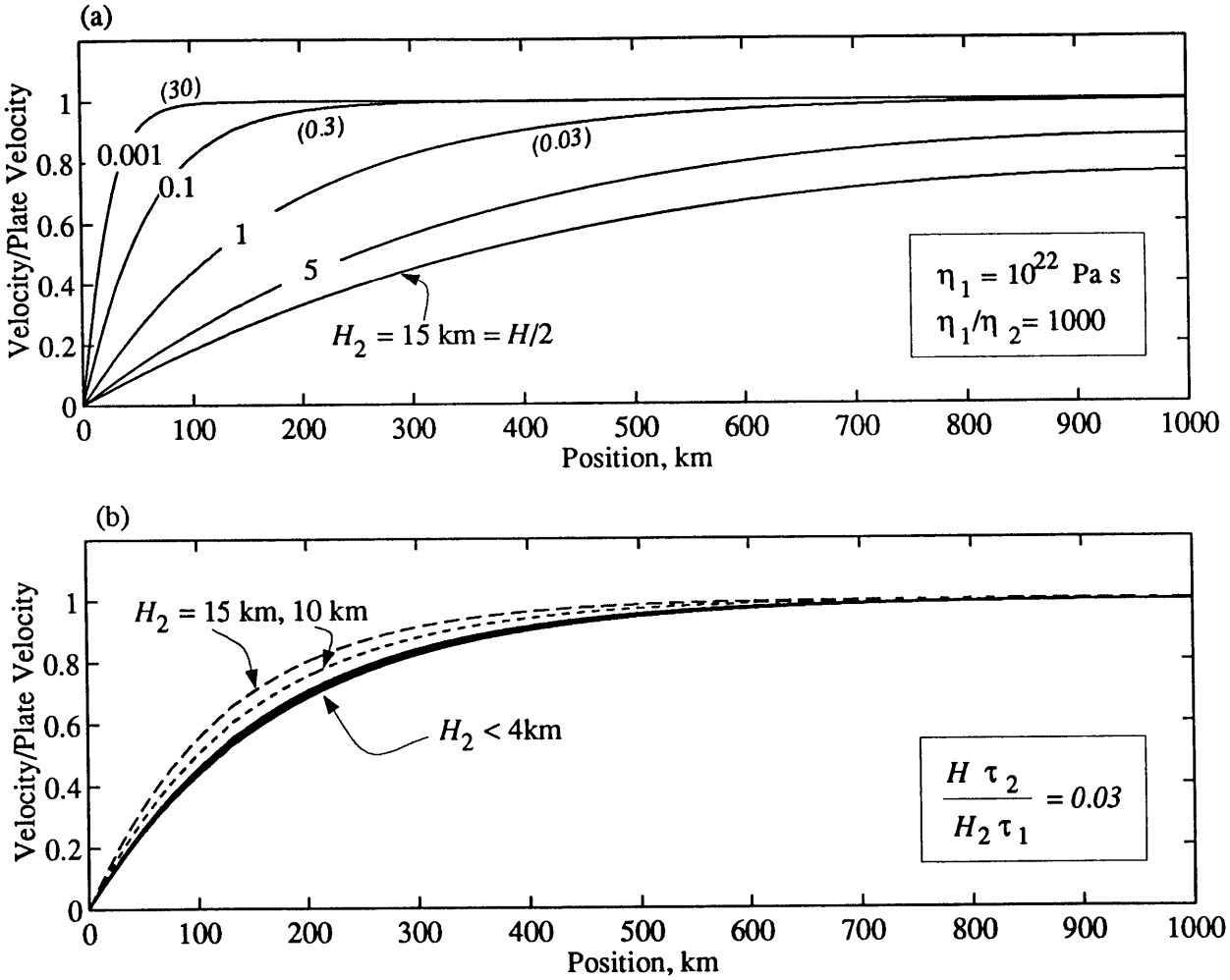
(a)
Velocity/Plate Velocity
Position, km
(30)
(0.3)
(0.03)
0.001
0.1
1
5
H_2 = 15 km = H/2
$\eta_1 = 10^{22}$ Pa s
$\eta_1/\eta_2 = 1000$
(b)
Velocity/Plate Velocity
Position, km
H_2 = 15 km, 10 km
H_2 < 4km
$\frac{H\,\tau_2}{H_2\,\tau_1} = 0.03$

Figure 4.4

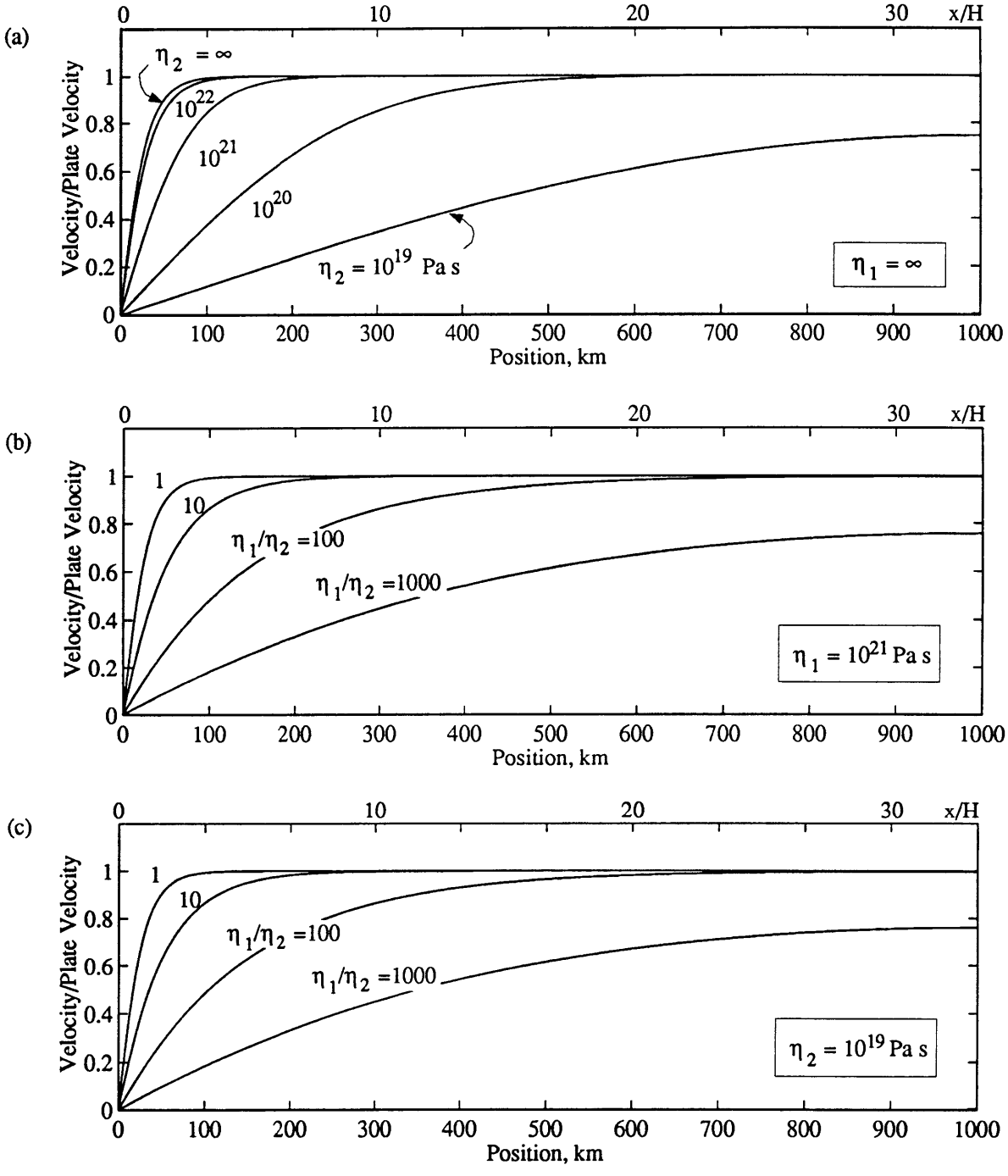
(a)
0
10
20
30
x/H
Velocity/Plate Velocity
$\eta_2 = \infty$
10^{22}
10^{21}
10^{20}
$\eta_2 = 10^{19}$ Pa s
$\eta_1 = \infty$
0
0.2
0.4
0.6
0.8
1
0
100
200
300
400
500
600
700
800
900
1000
Position, km
(b)
1
10
η_1/η_2 =100
η_1/η_2 =1000
$\eta_1 = 10^{21}$ Pa s
(c)
$\eta_2 = 10^{19}$ Pa s

Figure 4.5

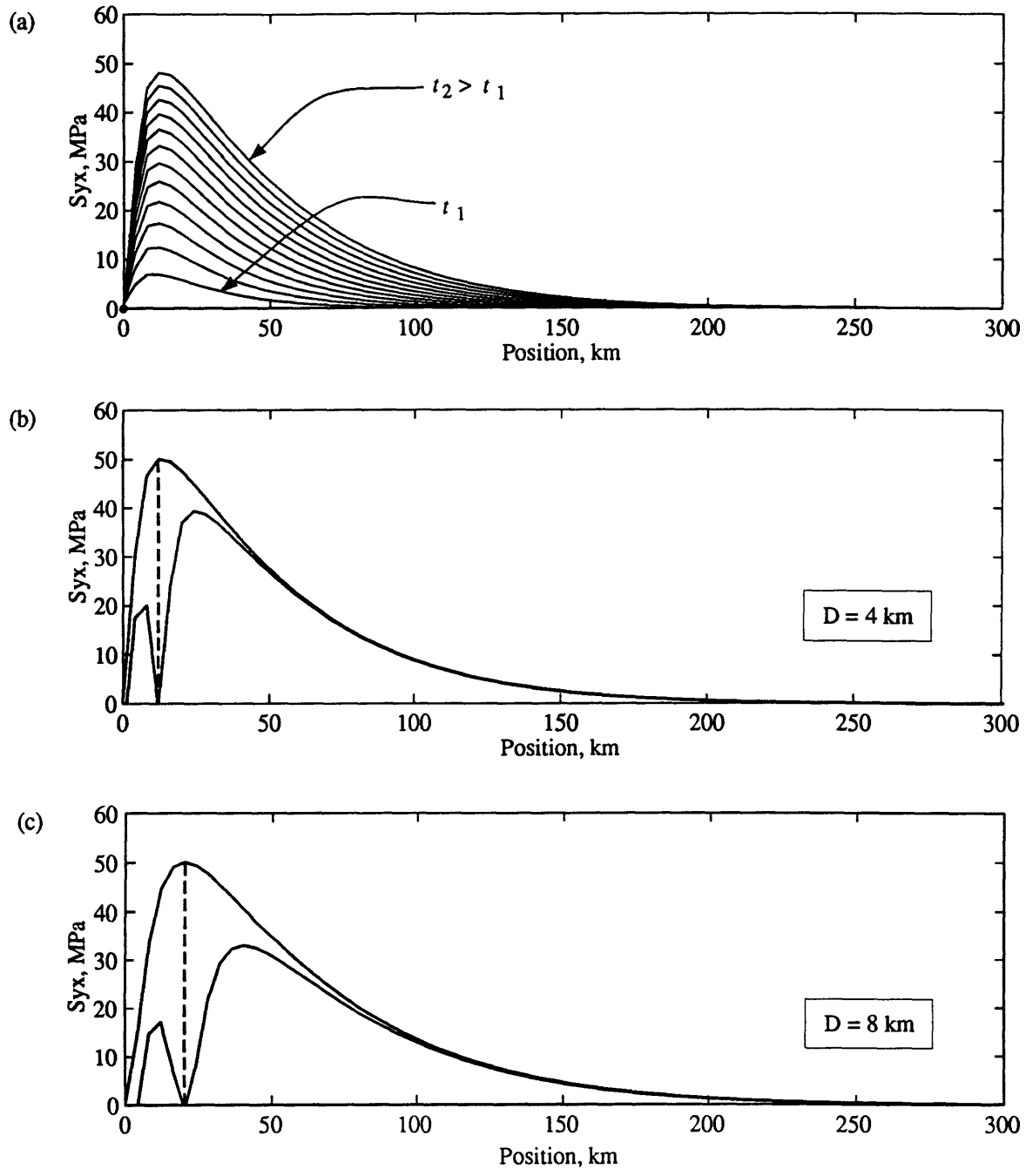
(a)
Syx, MPa
Position, km
$t_2 > t_1$
t_1
(b)
Syx, MPa
Position, km
D = 4 km
(c)
Syx, MPa
Position, km
D = 8 km

Figure 4.6

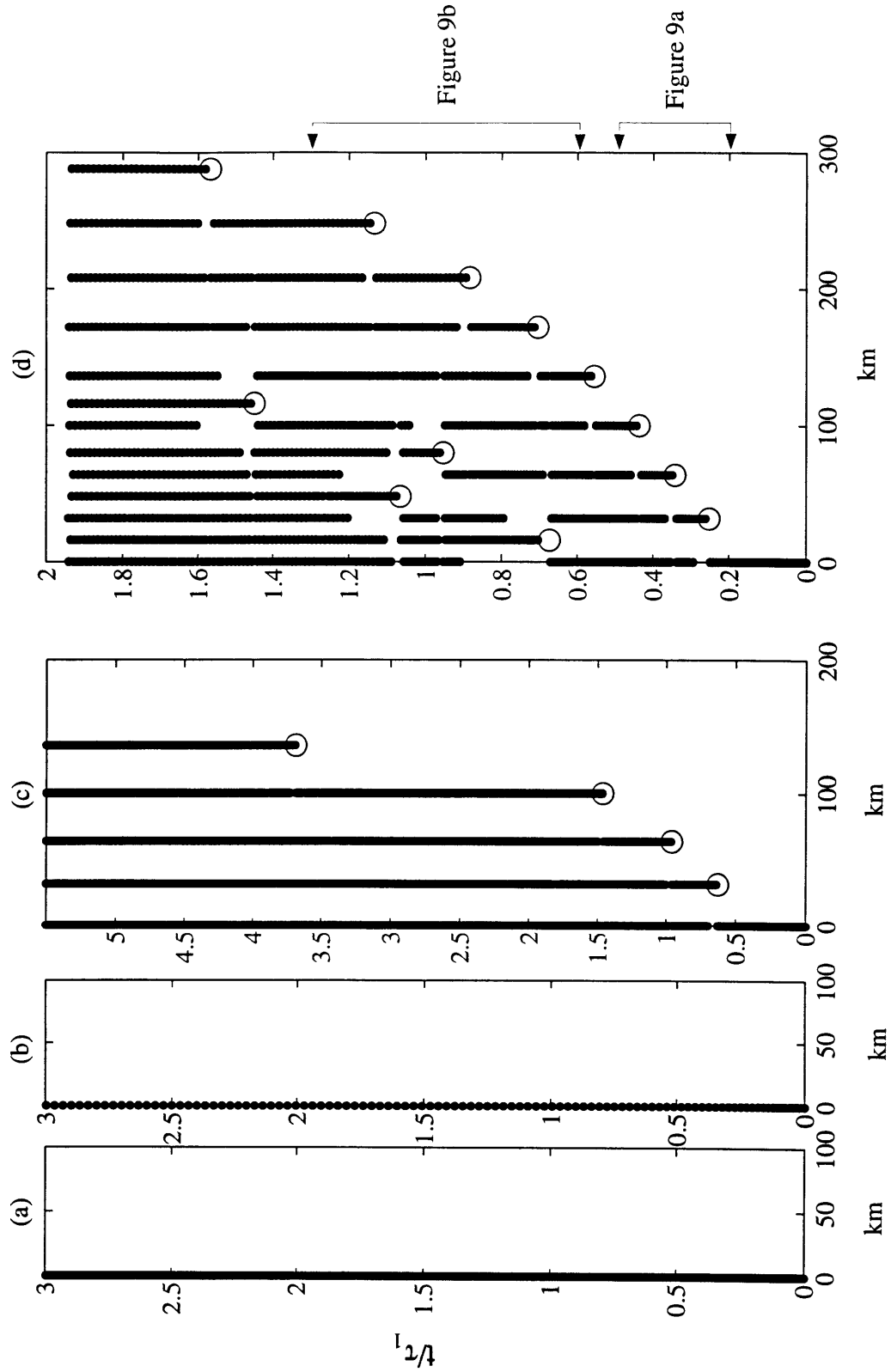

Figure 4.7

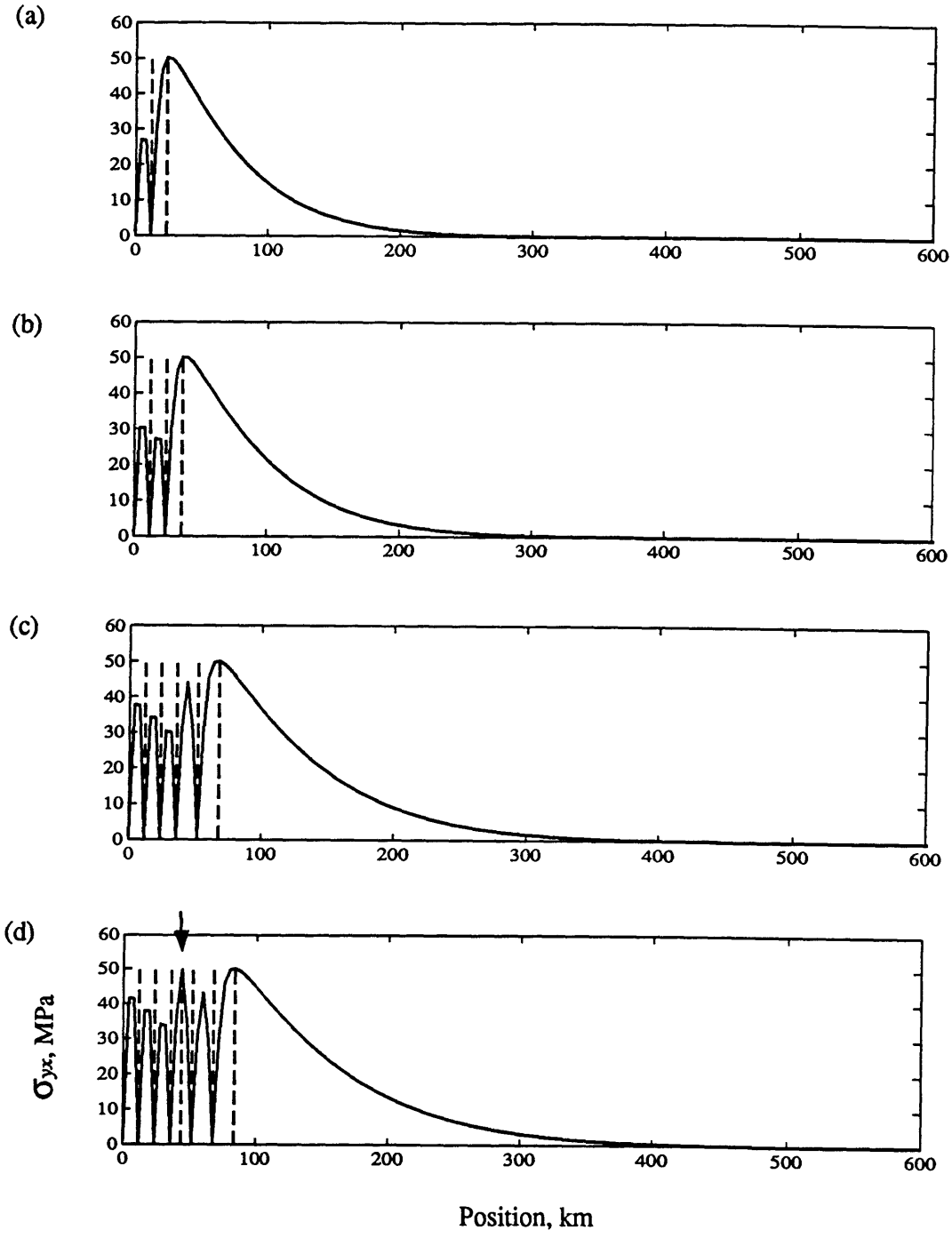
(a)
(b)
(c)
(d)
60
50
40
30
20
10
0
0
100
200
300
400
500
600
σyx, MPa
Position, km

Figure 4.8

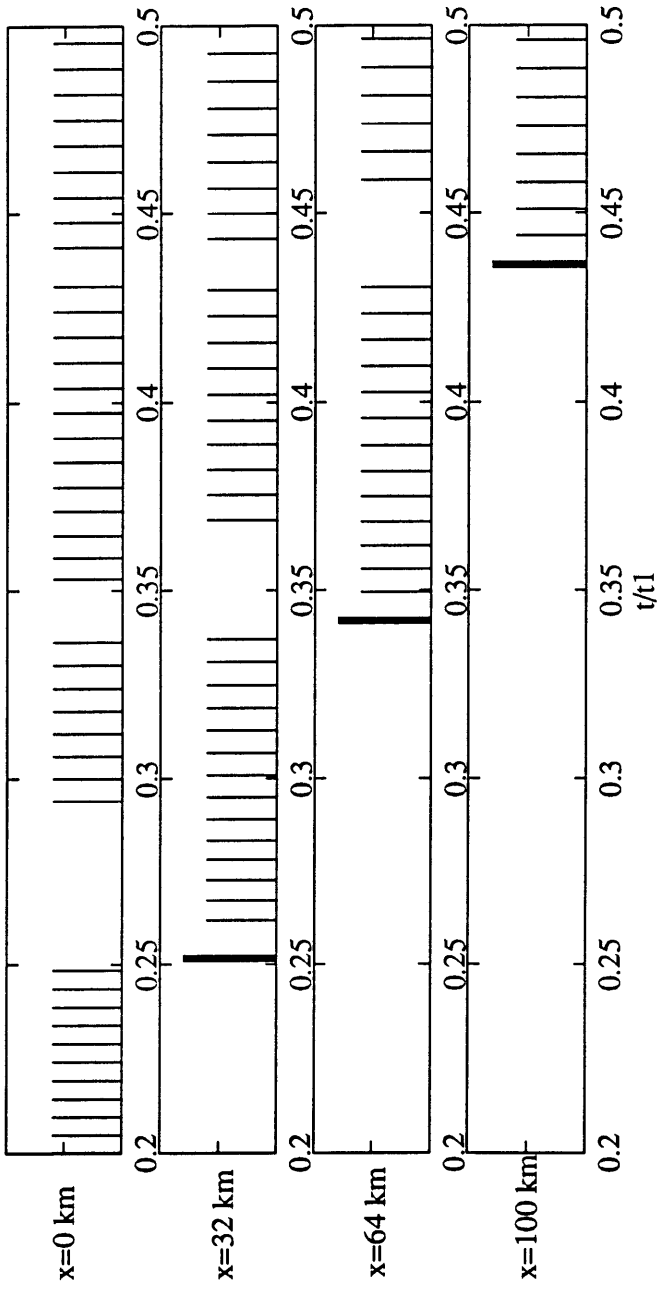

Figure 4.9a

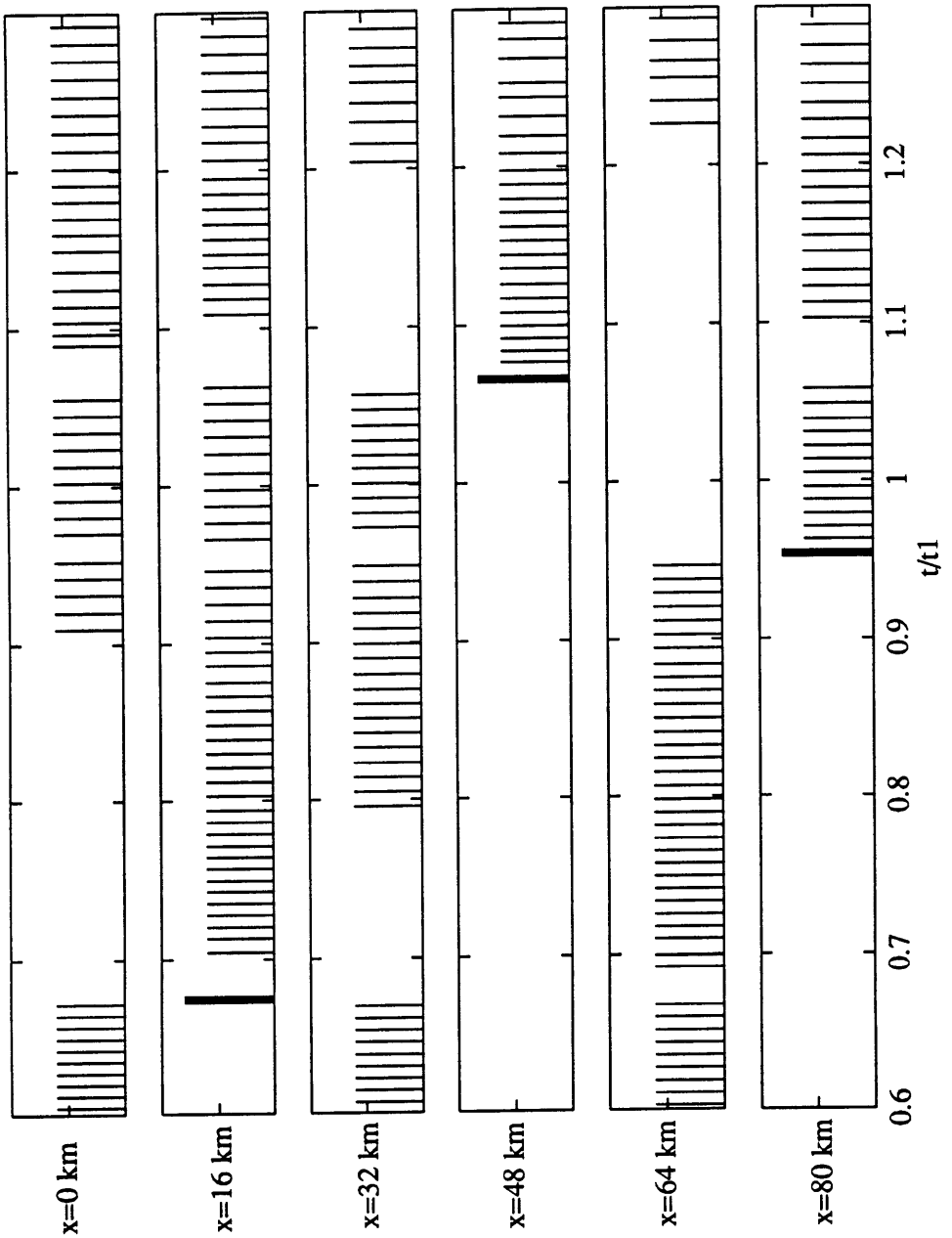

Figure 4.9b

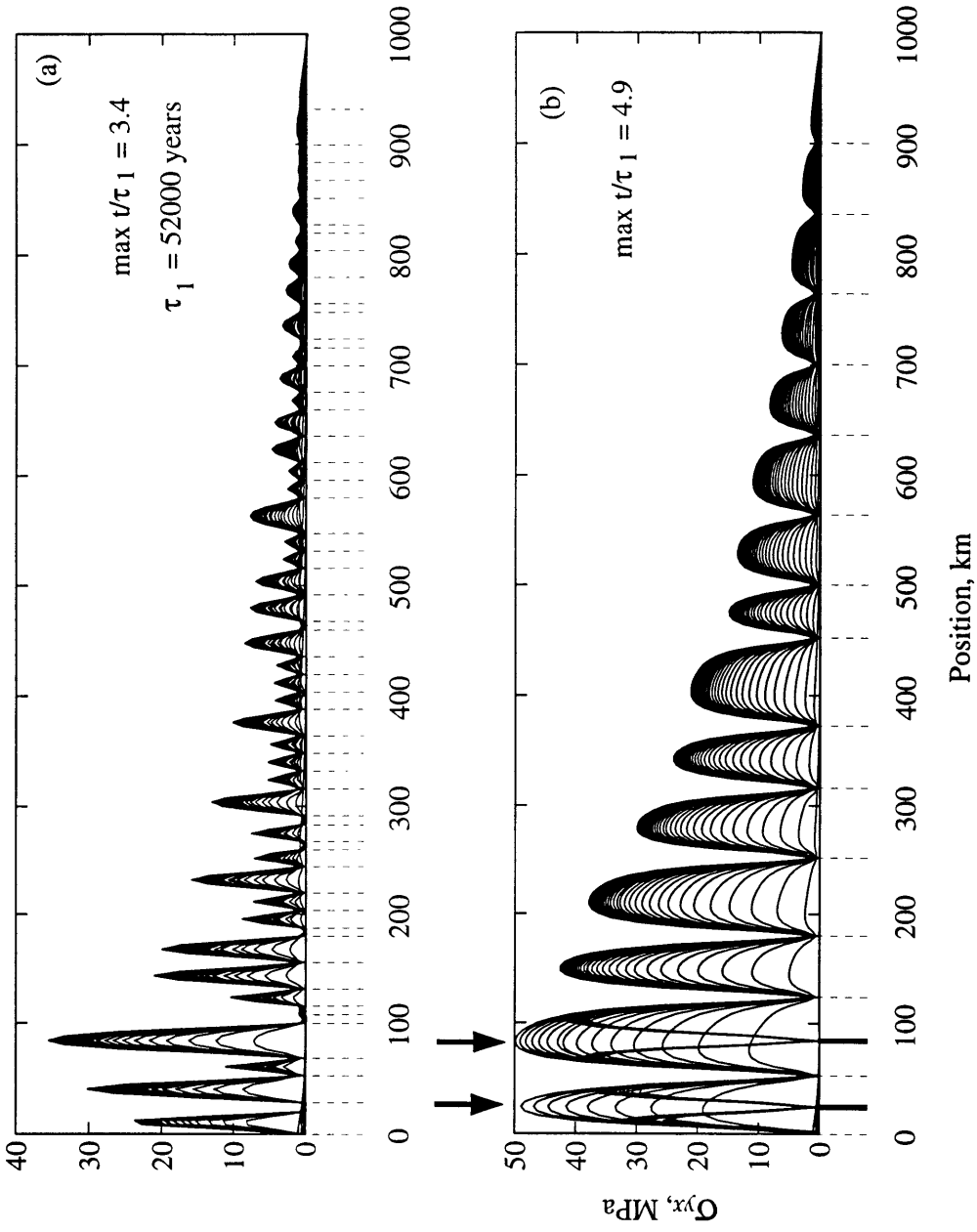
(a)
max t/τ 1 = 3.4
τ 1 = 52000 years
(b)
max t/τ 1 = 4.9
Gyx, MPa
Position, km
0
10
20
30
40
50
100
200
300
400
500
600
700
800
900
1000

Figure 4.10

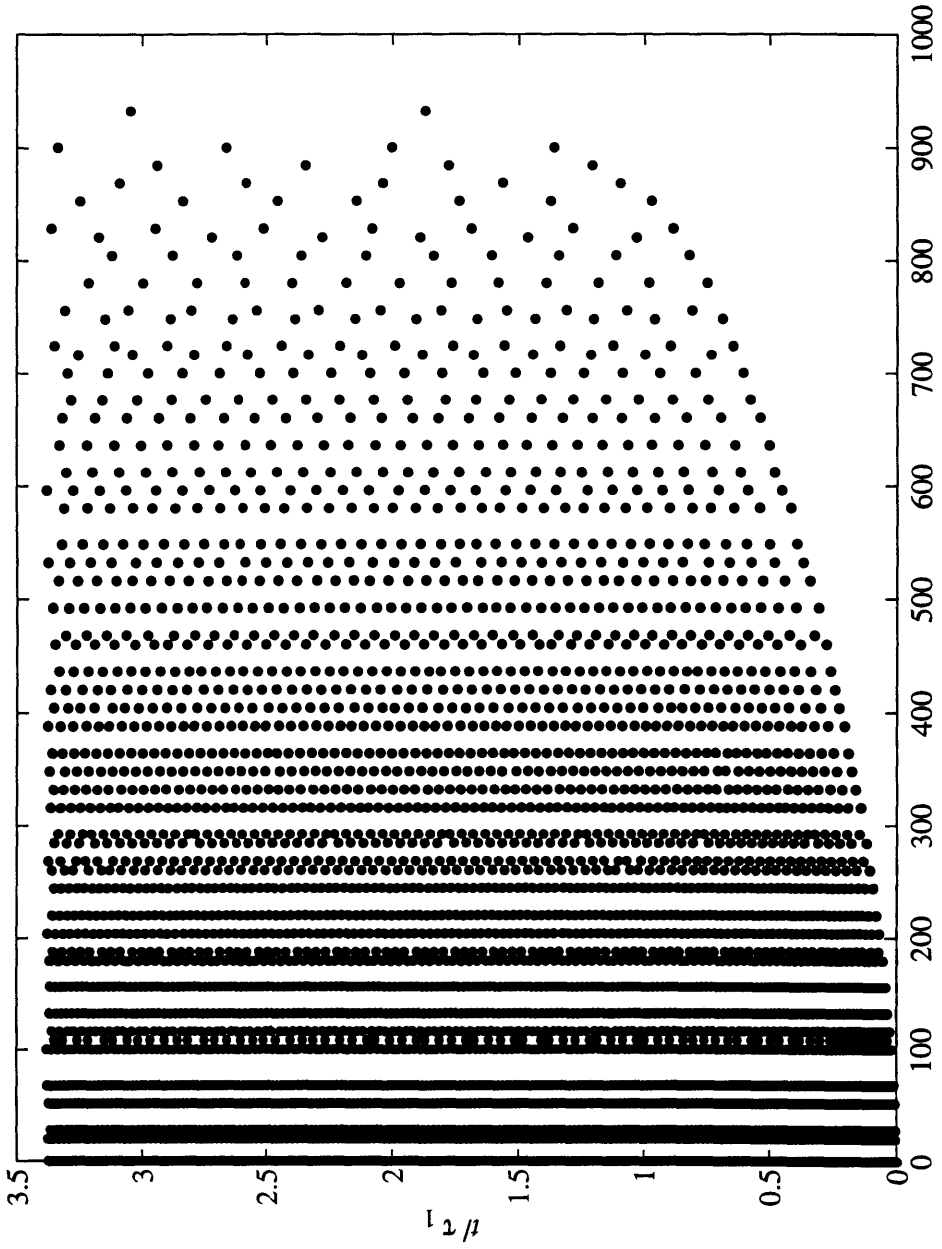
0
100
200
300
400
500
600
700
800
900
1000
0
0.5
1
1.5
2
2.5
3
3.5
I_1 vs μ

Figure 4.11a

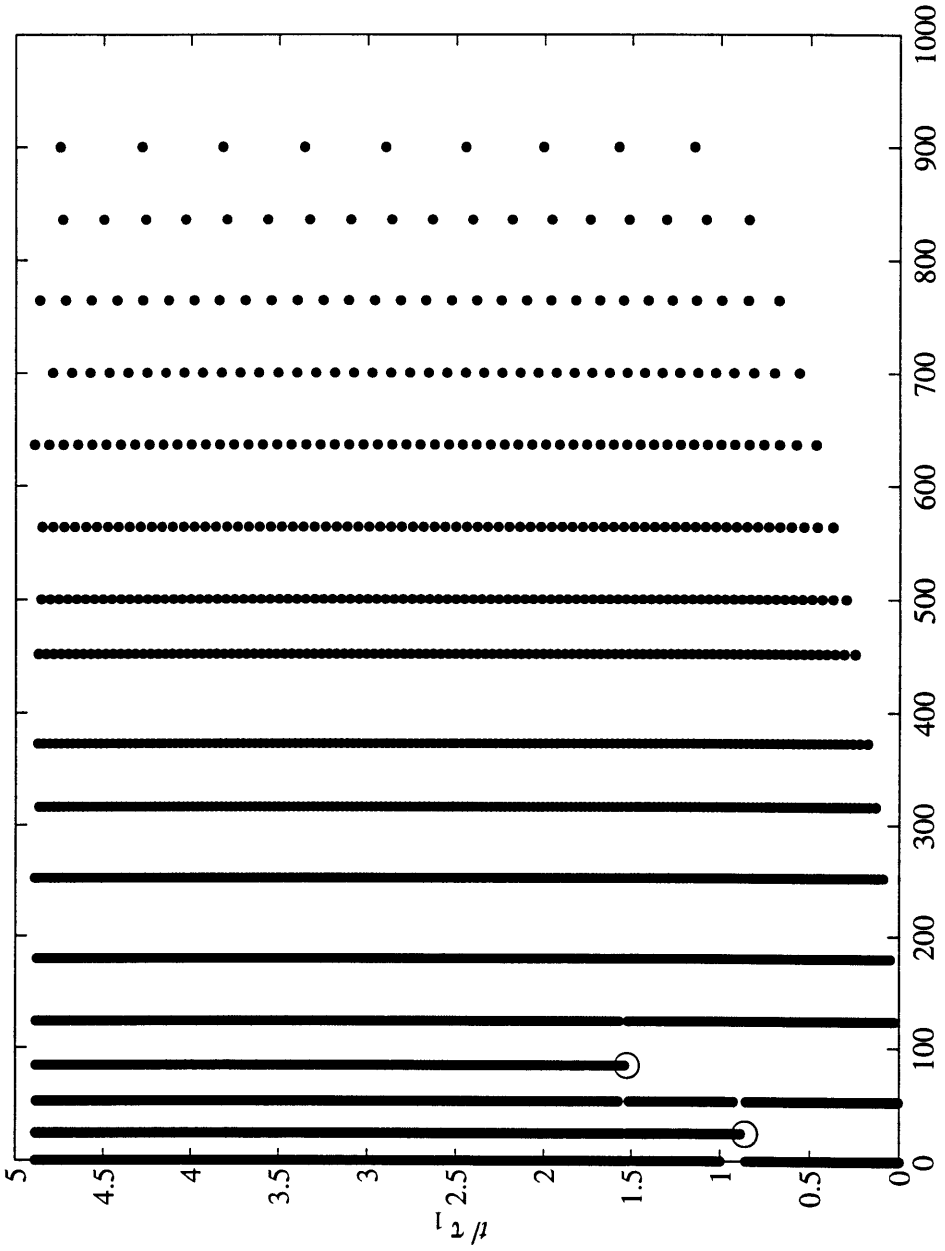
0
100
200
300
400
500
600
700
800
900
1000
0.5
1
1.5
2
2.5
3
3.5
4
4.5
5
μ / τ_1

Figure 4.11b

Chapter 5

Fault Systems at a Strike-Slip Plate Boundary (2)

ABSTRACT

This is the second part of a two-part study which investigates the role of continuum crustal rheology in governing both continuous deformation and the evolution and dynamics of faulting at a strike-slip plate boundary. We present a numerical model of deformation within a (Maxwell) viscoelastic crust with uniform elastic properties, but continuously varying viscosity as a function of depth. Brittle faulting is represented as static elastic dislocations imposed when a critical stress threshold for failure is exceeded. Our purpose is to understand the effects of large scale strength stratification within the crust on the growth and development of upper crustal fault networks and on surface strain rate patterns. The results presented here are in general agreement with the first part of our study and, in addition, provide further detailed insight into factors that control the number, spacing, and geometry of faults and the pattern of surface strain rates within a fault network.

We find that in the presence of a low viscosity lower crustal layer, the deformation zone within the upper crust broadens in time and encompasses a large number of interacting faults. When the lower crust behaves primarily elastically, however, the deformation zone remains narrow and focused on a single, plate-bounding fault. The maximum depth of brittle failure is confined to mid-crustal levels in the presence of a low viscosity lower crust, but extends down to the Moho when the lower and upper crust are of comparable viscosities. Surface strain rate patterns are far more complex in the

presence of a low viscosity lower crust, as faulting-induced strain rate perturbations lead to significant localized strain rate maxima corresponding to failures on a system of interacting faults.

INTRODUCTION

Brittle faults exist within the upper crust at a wide range of length scales, but much of the strain localization at active plate boundaries occurs on systems of large scale faults with widths of order $\approx 10^{1\text{-}3}$ m. In California, for example, strike-slip motion between the Pacific and North America plates is largely accommodated by seismic and aseismic slip on the San Andreas and associated strike-slip faults (e.g. *Wallace*, 1990). The number and spacing of active large scale faults is highly variable along the strike-slip plate boundary as indicated, for example, by the spatial distribution of seismicity in California (e.g., *Hill et al.*, 1990). Although the complexities of fault networks such as the San Andreas fault system must be greatly influenced by local compositional, geometric, and rheologic complexities within the crust, we study the extent to which the regional, bulk[1] rheologic structure of the crust controls the complexity of deformation and faulting at a strike-slip plate boundary.

In the first part of our study (Chapter 4) we have shown that even in the presence of pre-existing zones of weakness, the broad, systematic features of fault networks and the morphology of the deformation zone at a strike-slip plate boundary may be largely controlled by the bulk rheologic structure of the crust. This paper is the second part of this two-part study which investigates how continuum rheologic properties of the crust (such as large scale strength stratification across the upper and lower crust) control basic

---

[1] Here "bulk" is used to denote all continuous deformation within unfaulted regions of the crust, rather than just the volumetric strain. From here on, we use "rheologic structure" to denote properties which govern regional-scale deformational behavior rather than local deformation.

features of fault networks such as: the maximum depth-extent of faulting and its spatial variability, the number and spacing of faults, their geometries at depth, and their long-term evolution. The results of this study allow us to understand what implications, if any, the broad, large-scale geometry of a fault network at a strike-slip plate boundary has on the rheology of the crust.

MODEL OF CRUSTAL DEFORMATION

In this paper, as in Chapter 4, we study crustal deformation using an idealized linear viscoelastic model for the rheology of the crust, which allows simple strain rate dependence: elastic behavior on short time scales and viscous flow at long time scales. However, there are several important differences between the numerical model presented here and the analytic model in Chapter 4. First, instead of a two-layer rheologic structure to describe the upper and lower crust, we specify a continuous transition between a "strong" upper crust and a "weaker" lower crust. In addition, although we represent brittle failure by static elastic dislocations as in Chapter 4, we do not specify the maximum depth of faulting here but, instead, allow brittle failure to occur at all crustal levels. The bulk rheologic structure of the crust, which governs the magnitude of deviatoric stresses at any depth, will naturally restrict brittle behavior to the upper, "seismogenic" part of the crust. We also assume that fault planes may occur anywhere within the seismogenic crust and need not intersect the surface, therefore allowing the possibility of active, buried faults. Using the simple analytic model in Chapter 4 as a framework for understanding the basic rheologic factors that govern deformation at a strike-slip plate boundary, we study the evolution of stresses and faulting in detail, focusing on the variability of the maximum depth of faulting and the geometries of faults at depth. The effect of large-scale strength stratification within the crust is illustrated by

considering deformation with and without the presence of a weak lower crustal layer underlying a strong upper crust.

The crust is assumed to have a uniform shear modulus but exponentially decaying viscosity as a function of depth (Figure 5.1a), based on the viscosity profile used in *Royden*, (1996). This viscosity structure leads to an exponentially decaying relaxation time (defined as the ratio of viscosity to shear modulus) as a function of depth, determined by three free parameters: the viscosity at the surface, η_0, the viscosity decay length, α, and the shear modulus, μ. At time scales that are short compared to the relaxation time, the crust behaves primarily as an elastic medium and on time scales longer than the relaxation time, behavior is dominantly viscous. By choosing appropriate values of the viscosity and shear modulus, we allow for dominantly elastic behavior over short (co- and inter-seismic) times and viscous flow over longer (geologic) times. Strength stratification is specified by the depth-dependent relaxation time, for example a long relaxation time in the upper crust and a short viscosity decay length specifies a primarily elastic upper crust and a primarily viscous lower crust. Conversely, for the same relaxation time at the surface, a long viscosity decay length specifies approximately uniform strength properties within the crust, with primarily elastic behavior at all crustal levels.

For simplicity, we assume that the plate margin is infinitely long, with no variation of properties along strike, thereby reducing the problem to two-dimensions (Figure 5.1b). Starting from zero initial stresses and strains, we drive crustal deformation by imposing constant velocity of a "plate-like" mantle beneath and by far-field plate motions at the edges, $x=\pm L$ (Figure 5.1b). The imposed velocities have a highly idealized profile: $\pm V_0$ on either side of the plate boundary and zero at the boundary (x=0). (An advantage of choosing a narrow zone of high shear in the mantle is that broadening of the deformation zone within the crust will be due to the rheologic structure of the crust, and will not

reflect length scales of deformation in the mantle. This allows us to isolate and focus on the effects of rheologic stratification within the crust.) A single, pre-existing strike-slip fault is assumed to coincide with the vertical plane of the plate boundary and the sides of the model region are taken to be far from it, so that negligible shear stress acts on the edges ($x=\pm L$).

At an infinite strike-slip plate boundary, non-zero deviatoric shear stresses act on vertical planes parallel to the boundary, σ_{yx}, and on horizontal planes, σ_{yz}, (Figure 5.1c). At equilibrium, these stresses are related to each other by the equation of motion,

$$\frac{d\sigma_{yz}}{dz}+\frac{d\sigma_{yx}}{dx}=0 \tag{5.1}$$

and to the strain rates through the constitutive equations for a (Maxwell) viscoelastic crust,

$$\mu\frac{dv}{dx}=\dot{\sigma}_{yx}+\frac{\sigma_{yx}}{\tau} \tag{5.2a}$$

$$\mu\frac{dv}{dz}=\dot{\sigma}_{yz}+\frac{\sigma_{yz}}{\tau} \tag{5.2b}$$

where v is velocity parallel to the plate boundary and τ is relaxation time, $\tau=\tau_0 e^{-z/\alpha}$ (where τ_0 is the relaxation time at the surface, $\tau_0=\eta_0/\mu$). Combining equations (5.1) and (5.2) leads to the following equation for the velocity (see Appendix),

$$\tau(z)\left(\frac{\partial^2\dot{v}}{\partial x^2}+\frac{\partial^2\dot{v}}{\partial z^2}\right)=\frac{1}{\alpha}\frac{\partial v}{\partial z}-\left(\frac{\partial^2 v}{\partial x^2}+\frac{\partial^2 v}{\partial z^2}\right), \tag{5.3}$$

which is solved numerically by finite difference techniques over the calculation grid (the crust is discretized into 4 km by 4 km cells, from $0\le z\le H$=28 km and $0\le x\le L>>$H). At each time step we calculate displacements by integrating velocity (assuming zero initial displacements) and stresses by using equation (5.2) (assuming zero initial stresses). Note that in an elastic crust the left-hand side of equation (5.3) is zero, whereas in a fully (Newtonian) viscous crust, the right-hand side of equation (5.3) is zero.

Brittle failure, which occurs over short time scales, is assumed to be an elastic response to stress accumulation within the crust. Faults are represented by static elastic dislocations with uniform slip discontinuity (Appendix), imposed at locations determined by whether the shear stress on vertical planes parallel to the plate boundary, σ_{yx}, exceeds the faulting or fracture thresholds (Figure 5.2; parameters used here and in following figures are listed in Table 5.1). (Note that we focus on σ_{yx} because, in the results presented below, the orientation of optimal brittle failure planes at all fault locations are nearly vertical and parallel to the boundary. Thus we do not include inclined dislocations in our analysis although, in principle, these may be incorporated in a similar way.)

As in Chapter 4, we incorporate multiple failures assuming that while one fault fails all others are welded, so that individual elastic solutions for multiple faulting events are superposed (i.e. faults are independent, but see *Segall and Pollard*, 1980). To distinguish between failure on a pre-existing fault and fracture of a new fault, we choose a high cohesion (50 MPa) for fracture and a low value for frictional sliding (1 MPa). The brittle failure threshold increases as a function of depth (overburden) at a rate determined by the coefficient of friction, assumed constant (0.6) throughout the crust (Figure 5.2). In this model, brittle failure is allowed to occur at all crustal levels, provided that shear stresses are high enough. The maximum depth of brittle failure, therefore, is governed directly by the bulk rheologic structure of the crust and is a function of time and distance away from the plate boundary.

When the shear stress σ_{yx} exceeds the failure criterion at a particular discrete "cell" within the crust, a static elastic dislocation is imposed there and the stresses and displacements due to faulting are added to the pre-failure values (faulting is assumed to be instantaneous, so that the crust behaves elastically). The new stress field is tested again for breach of the brittle failure envelope and the procedure is repeated until there are no parts of the crust undergoing faulting or fracture. As a result of the finite grid

(cell) size in the calculation, there are no stress singularities at the location of the plate boundary at the Moho and, since stresses are calculated only at the center point of each cell, stress singularities at the tips of dislocations may be ignored. We assume for simplicity that the post-failure stress at the center of each dislocation is a fixed fraction (1/3) of the stress required to initiate sliding on a pre-existing fault (Figure 5.2). As a result, the stress drop during fracture is much larger than that during slip on a pre-existing fault.

The exponentially decaying relaxation time as a function of depth, together with the possibility of fracture at deep levels in this model, means that the relaxation time at the lower tips of faults is significantly shorter here than in the analytic model of Chapter 4 (where relaxation times at the lowest parts of the faults were the same as that at the surface). As a result, the faulting-related perturbations to the rate of stress change and to the background velocity field (strain rates) decay significantly faster in this model than in Chapter 4 (see Chapter 4 for a discussion). Transient variations in stress rate which, at any location within the crust, are proportional to the instantaneous stress change there due to faulting, decay much faster in this model. As a result, we relax an assumption made in part I: that faulting does not influence the long-term background velocity field, and instead, study the variations in strain rates during evolution of the fault network.

DEFORMATION OF A HIGH VISCOSITY CRUST

To study deformation within a high viscosity crust which exhibits primarily elastic behavior at all depths, we choose a high viscosity at the surface (which corresponds to a long relaxation time, $\approx 10^5$ years) and a long viscosity decay length, α=15 km$\approx H/2$ (Figure 5.3). This value of α specifies slow variation of the relaxation time with depth and the surface viscosity (10^{23} Pa s) is chosen so that behavior of the entire crust is

mostly elastic until the onset of viscous behavior at the Moho at times greater than $\approx 10^4$ years (Figure 5.3). When mantle displacements are first imposed at the base of the crust, deformation is initially greatest at the location of the plate boundary at the Moho. At this time, at any depth within the crust the shear stress σ_{yx} is greatest on the plane of the plate boundary, but varies with depth from a minimum at the surface to a maximum at the Moho. The rate at which σ_{yx} increases with depth on the plate-boundary is less than the rate of growth of the brittle stress threshold with depth, so that the brittle failure threshold is first exceeded at the surface rather than at depth. Near-surface faulting at the plate boundary causes two local stress maxima: first, a stress maximum at the surface laterally displaced from the plate boundary (see Chapter 4, Figure 4.6); and second, a local shear stress maximum at the plate boundary at depth below the fault plane. These stress maxima grow in time and cause further faulting at depth and on new fault planes away from the plate boundary.

The growth of the stress maximum at the surface away from the plate boundary is governed by the bulk rheology of the crust, which controls background (tectonic) rates of stress growth and the inherent width of the zone of deformation. From the analytic model presented in Chapter 4 we expect that time evolution of deformation within an approximately uniform viscosity crust should not lead to significant widening of the deformation zone, so that high strain rates should remain concentrated in a narrow region around the plate boundary. This is indeed observed in the numerical model as most of the deformation is focused in a narrow region surrounding the main plate-bounding fault, which develops a large slip discontinuity because of repeated failures (Figure 5.4a).

Once failure initiates at the surface within this narrow deformation zone, tectonic loading causes growth of the deep-seated local stress maximum at the base of the fault. If this maximum eventually breaches the local brittle failure envelope, faulting occurs and the process is repeated at successively deeper levels with time. Within a high viscosity

crust, the rate of stress growth is high enough that, during 10^4 years of evolution, the nodes at which brittle failure occurs lie along the plate boundary and extend from the surface down to the Moho (Figure 5.5a). The fact that stresses are high enough at deep crustal levels to allow deep-seated brittle failure violates the restriction that time-averaged displacements at the Moho due to faulting must be small compared to those due to tectonic loading (see section on elastic dislocations in Appendix). Thus, although the location and depth-extent of faulting in Figure 5.5a is correct, the detailed displacement field (Figure 5.4a) should strictly be modeled using dislocations in a confined elastic layer rather than in a half-space. The overall features of the deformation, however, such as the fact that it is concentrated on a single, plate-bounding fault, are robust.

As a result of the simple, narrow deformation zone, strain rates at the surface are highest at the plate boundary and decrease monotonically with distance away from it (Figure 5.6a). Long-term viscoelastic relaxation of the crust causes surface strain rates at any fixed position to decay with time, although the overall strain rate pattern is unchanging (Figure 5.6a). Local orientations of the principal stress axes within the crust, together with the brittle failure criterion, are used to determine the orientations of the optimal failure planes (Figure 5.7a). By symmetry, the infinite plate-margin constrains these planes to have the same sense of slip as the plate motions (dextral) and, at the surface or near the plate boundary at depth, to be oriented vertically parallel to the plate boundary (Figure 5.7a). At deep crustal levels and away from the plate boundary these planes undergo a slight rotation because of the onset of viscous behavior at depth over times longer than the lower crustal relaxation time, 10^4 years (t=1.06×10^4 years in Figure 5.7a). From the optimal failure plane orientations, we see that at the locations of brittle failure the fault planes are nearly vertical and parallel to the plate boundary (compare Figures 5.7a and 5.5a). Therefore, the zone of failure encompasses a vertical fault plane extending from the surface to the Moho, coincident with the plate boundary.

DEFORMATION IN THE PRESENCE OF A LOW VISCOSITY LOWER CRUST

Keeping the viscosity at the surface fixed, we now choose a short viscosity decay scale (α=3 km, $\approx H/10$), and thus a short lower crustal relaxation time compared to geologic times (Figure 5.3). Deformation within the lower crust is therefore primarily viscous (onset of viscous behavior occurs after ≈10 to 100 years) but behavior in the upper crust remains dominantly elastic. The analytic model in Chapter 4 suggests that deformation in the presence of a low viscosity lower crust is highly time-dependent, marked by a widening region of high strain at the surface. At the base of the crust, however, the imposed mantle velocities are time-independent, and thus the zone of high shear at the Moho is narrow at all times. We therefore expect the deformation zone to widen with time at upper crustal levels, but remain narrow in the lower crust as observed in Figure 5.4b.

The region of brittle failure is initially at near-surface regions of the plate boundary, as in a high viscosity crust (panels i and ii in Figure 5.5a and b). Repeated faulting here gives rise to local stress maxima at depth and at the surface away from the plate margin, which grow in time and eventually breach the local brittle failure envelope. Since the plane of the plate boundary is assumed to be a pre-existing fault, failure proceeds to deeper levels at the plate margin first before fracturing new faults away from it (panel ii in Figure 5.5b). Therefore, the zone of brittle faulting grows deeper and wider with time and, over long times, encompasses a broad network of interacting brittle faults (Figures 5.4b and 5.5b). An important difference between these results and behavior in the presence of a high viscosity lower crust (Figures 4a and 5a) is that the zone of brittle failure is confined to shallow to mid-crustal levels only (≤10 km) and the depth-extent of faulting decreases away from the plate margin (Figure 5.5b). The confinement of brittle behavior to shallow crustal levels arises because of viscous flow in the low viscosity

lower crust and relaxation of stresses at mid-crustal levels, which prevent stresses on vertical planes from growing to very large values there (discussed below), thus inhibiting brittle failure at depth. The decrease in the maximum depth of faulting as a function of distance from the plate boundary occurs because shear stresses and stress rates generally decrease away from the plate margin.

The characteristic spacing of faults (e.g., Figure 5.5b) is primarily governed by the depth-extent of initial, near-surface faulting within the crust (see Chapter 4) and by the brittle failure criterion. When the values of cohesion for fracture and for faulting are comparable to each other (only their difference is important, not their absolute magnitudes), the stress thresholds for fracture of a new fault and sliding on a pre-existing one are almost equal at all depths. In this case, stresses adjacent to a pre-existing fault need not be significantly greater than the frictional stress on the fault itself in order to fracture the adjacent region. Thus with tectonic loading, as stresses adjacent to faults grow in time they quickly breach the fracture criterion, leading to new faults at a much finer spacing (e.g. Figure 5.5c, where the spacing is limited by the calculation grid size).

Surface strain rates in the presence of a low-viscosity lower crust are dramatically different and reflect a complicated pattern of time evolution (Figure 5.6b). Initially, while the deformation zone is still narrow (width$<H$, $t \leq 3000$ years), maximum strain rates occur at the plate margin. With time however, the widening network of brittle faults gives rise to significant localized strain-rate maxima at zones of brittle failure away from the plate margin. Although strain rates remain generally highest at the plate boundary, fracture of new faults produces occasional periods where the maximum strain rates are not on the main plate-bounding fault (see Figure 5.6b and Long-term Evolution below).

The local orientations of principal stress directions are determined by the relative magnitudes of the deviatoric shear stresses, σ_{yx} and σ_{yz}, which in turn are determined by the deformation through the constitutive equations (5.2). When the shear stress on

horizontal planes, σ_{yz}, is much smaller than that on vertical planes, σ_{yx}, the principal stress orientations (combined with the brittle failure criterion) lead to a nearly vertical orientation of the optimal failure planes. However, when $\sigma_{yz}>>\sigma_{yx}$, the optimal failure planes are nearly horizontal. In a low viscosity lower crustal layer which has undergone relaxation of stresses related to elastic strains and is therefore flowing viscously, strain rates (velocity gradients) are directly proportional to residual stresses. Thus if vertical velocity gradients exceed horizontal ones ($\partial v/\partial z>>\partial v/\partial x$), as will be the case when the lower crust achieves steady state, optimal failure planes will be sub-horizontal. As a result, at times which are long compared to the lower crustal relaxation time (10 to 100 years) but short compared to the upper crustal one (10^5 years), optimal failure planes will be oriented vertically at the surface (by symmetry) and within the upper crust, but will rotate into sub-horizontal positions within the low viscosity lower crust (Figure 5.7b).

Over geologic times, the distribution of shear stresses within the crust is dramatically different with and without the presence of a low viscosity lower crust. In a high viscosity crust, the maximum shear stress σ_{yx} is located at the plate boundary at the Moho, although a small local stress maximum develops off the main fault plane due to near-surface brittle failure (Figures 5.5a and 5.8a). In the presence of a low viscosity lower crust however, the maximum σ_{yx} is at mid-crustal levels on the main fault plane and significant local stress maxima develop away from the plate margin because of new faults (Figures 5.5b and 5.8b). As the deformation zone widens, these fault-related stress maxima appear at increasing distances from the plate margin but at decreasing depths (due to the smaller depth-extent of faulting away from the plate boundary, Figures 5.5b and 5.9).

Long-term evolution. The results discussed thus far are based on the early and intermediate-term evolution of the crust (t=0 to 1.06×10^4 years≈1/10th the relaxation

time at the surface). We now consider how the brittle fault system and the overall region of distributed deformation evolve over time scales approaching the relaxation time of the upper crust (10^5 years). From the analytic model in Chapter 4 we expect that, over long times, deformation at the plate margin will reflect a competition between long-term viscoelastic relaxation, which leads to decaying rates of stress growth, and perturbations to the stress rate due to faulting. At time scales which are significantly longer than the upper crustal relaxation time, the system evolves to an approximate steady-state where the stresses relieved by faulting are approximately balanced by stresses due to tectonic loading.

Time evolution of shear stress σ_{yx} (Figure 5.9) demonstrates the widening region of brittle failure which grows to encompass many parallel faults and gives rise to the complex strain rate pattern observed at the surface (Figures 5.6b and 5.10). Fracture, which in our model causes a much greater stress drop than failure on a pre-existing fault, significantly reduces σ_{yx} around the newly fractured fault plane. This inhibits failure on all nearby faults, giving rise to complicated recurrence patterns (Figure 5.10). Figure 5.10 illustrates how faulting and fracture determine the time-varying strain rate patterns observed at the surface. Fracture events, in particular, cause pronounced local strain rate maxima centered on the new fault plane and reduce strain rates around the newly fractured fault. For example, in Figure 5.10(a) the overlapping circles at 12 km and ≈3500 years represent near-surface fracture (see caption). This fault plane then continues to slip in very small events until ≈5000 years when fracture of a new near-surface fault at x=24 km shuts off activity. When activity resumes at ≈6000 years, the fault plane deepens and fractures at 6 km depth (overlapping triangles). The fault plane deepens again by fracturing at 10 km depth at ≈20500 years (Figure 5.10c).

At long times, a system of faults is established at a characteristic spacing, with repeating failures on each fault (Figure 5.10b and c). Once the fault network is

established and the upper crust is divided into fault-bounded blocks, there is no significant fracturing of new faults within these blocks. In Figure 5.10 there are isolated failures which occur within crustal blocks, but these faults have little activity and long periods of quiescence (e.g., at x=8 km, $t\approx$19000 years and x=32 km, $t\approx$14000 years in 5.10b and x=44 km, $t\approx$21000 years in 5.10c). They fracture at depth (related to deep-seated stress maxima) adjacent to an existing fault, but failures at these locations do not fracture near-surface regions. These isolated, deep fault planes remain inactive for long times on the order of 10^4 years and thus they do not constitute a zone of active strain localization. This is an important difference between time evolution in this model and the simple analytic model in Chapter 4 (where fault-bounded upper crustal blocks were subdivided in time, see Figure 4.7c of Chapter 4), which arises because of the variable depth of faulting and the fact that buried dislocations are allowed here. The local stress maxima at depth within fault-bounded blocks in this model are relieved by deep-seated faulting events on the adjacent faults (the stress drop during faulting in this model increases linearly with depth). As a result, stress maxima within fault-bounded blocks grow at a very slow rate, explaining the rarity of fracture within fault-bounded blocks and the long recurrence times on these fracture planes (Figure 5.10).

The complex evolution of the fault system observed in surface strain rate patterns is also reflected in the failure histories on the faults themselves. Recurrence intervals at early times ($t\leq10^4$ years) during the evolution are widely scattered because of the influence of large-stress drop events such as fracture on nearby faults as the deformation zone widens (Figure 5.11b). At long times however, once a fault network has been established, the range of recurrence intervals is much narrower on each fault although they remain disordered. The amount of scatter in the recurrence intervals is a strong function of distance away from the plate boundary (i.e. the age of the fault), with more regular failure histories on inner faults and more scattered recurrence intervals (from 10

to ≈200 years) away from the boundary (Figure 5.11b). By comparison, failure histories on the main plate-bounding fault in a high viscosity crust are uniform (Figure 5.11a; note that the single isolated point in Figure 5.11a is due to a long period of quiescence on the main fault plane when a near-surface fracture event occurs 12 km away; see also Figure 5.5a).

DISCUSSION

The choice of a viscoelastic description for continuous deformation within the crust allows us to incorporate very high strain rate elastic responses to stress accumulation (e.g., faulting may thus be represented by static elastic dislocations) into a consistent picture of the long-term (viscous) rheology of the crust. While there is widespread evidence in some areas for viscous flow in the lower crust over geologic times (e.g., *Block and Royden*, 1990), the long-term behavior of the upper crust is less well constrained. Over co-, post-, and inter-seismic times, previous theoretical studies suggest that deformation in the upper crust may be modeled using either elastic or viscoelastic rheology (e.g., *Cohen*, 1980; *Li and Rice*, 1987; *Lyzenga et al.*, 1991; *Linker and Rice*, 1997). However, over geologic times, evidence for unrecoverable large-scale strain within the upper crust may be indicated by the presence of upper crustal folds (such as over blind thrust faults, or at large strike-slip faults, e.g. the Garlock fault in southern California). We suggest here that by choosing a very long relaxation time within the upper crust, we allow permanent deformation over long times and at low strain rates and also provide a natural transition from primarily elastic behavior in the uppermost crust to (possibly) viscous flow in the lower crust.

The results above suggest that the relaxation time within the lower crust places strong controls on the nature and development of fault systems within the upper crust and may partly control complex failure histories across fault networks. As discussed in Chapter 4,

the primary effect of a weak lower crustal layer is to broaden the deformation zone in time, and thus lead to the formation of a network of interacting faults in the upper crust. In a low viscosity lower crust, stresses at depth are relieved by viscous flow so that maximum stresses within the crust occur at mid-crustal levels, associated with faulting-induced stress changes. The maximum depth of brittle failure is restricted to upper- to mid-crustal levels only ($\leq$10 km in this model), controlled by the prescribed short relaxation time of the lower crust.

In addition, although brittle failure in our model occurred on planes oriented vertically parallel to the strike-slip plate boundary, the presence of a low viscosity lower crust rotates these optimal failure planes at depth into sub-horizontal orientations. This suggests that vertical faults in the near-surface and mid-crustal regions may extend into inclined zones of high shear within the weak lower crust. At long times during the evolution of the model, the concentration of horizontal shear strain ($\partial u/\partial x$) into vertical zones in the upper crust which join up with curved ones in the lower crust is consistent with this interpretation (Figure 5.12).

Surface strain rate patterns are strongly influenced by the rheology of the lower crust. For example, the presence of a low viscosity lower crustal layer enhances and engenders complex surface strain rate patterns, whereas a high viscosity lower crustal layer leads to a simple deformation pattern (Figures 5.6 and 5.10). The modulation of shear stress acting on a fault by failures on neighboring faults plays a large role in determining failure histories and scattered recurrence intervals as the fault network evolves. In our model, where we prescribe two classes of failure sizes, small stress drops for faulting and large ones for fracture, the complexity in the surface strain rate pattern is primarily influenced by fracture of new faults (Figure 5.10). In a more general case however, where each faulting event may itself have some statistical variation in possible stress drops, the strain rate pattern might be far more complex.

These results suggest that even in the absence of inherent complexities within the crust (such as compositional heterogeneities, geometric irregularities of faults, the presence of weak gouge zones, fluids, etc.), deformation at a pure strike-slip plate boundary may be complicated simply because of large-scale strength stratification between the upper and lower crust. As we are mainly interested in the role of crustal rheology, we have not modeled the effects of complex mantle motions (e.g., distributed shear) which may further complicate surface deformation patterns. Our results suggest that, provided mantle motions are simple and reasonably time-independent, a change of a factor of 10^3 in lower crustal viscosity can dramatically change the character of deformation at a strike-slip boundary and determine the distribution and geometry of large-scale faults within the upper crust.

What implications do these results have on continuum crustal rheology at a strike-slip plate boundary such as the Pacific-North America boundary in California? Strain rate and seismicity patterns on the San Andreas fault system suggest that deformation at the northern and southern regions of the fault system occurs on networks of sub-parallel, large-scale faults (*Hill et al.*, 1990). In northern California for example, the fault system consists of the San Andreas, Hayward, Calaveras, and Green Valley faults and in southern California the fault system includes the Elsinore, San Jacinto, and San Andreas faults (Figure 5.4 in *Hill et al.*, 1990). In central California, however, seismicity clusters primarily on the trace of the San Andreas fault (Figure 5.4 in *Hill et al.*, 1990).

The many simplifications and assumptions in our model make it difficult to directly interpret our results in the context of these observations. For example, complex deformation in the mantle near the Transverse Ranges severely limits interpreting large-scale fault network geometries there in terms of a simple, pure strike slip system (e.g. *Weldon and Humphreys*, 1986; *Humphreys and Hager*, 1990). Further to the south however, and in northern California, provided that the nature of plate motions in the

mantle is simple, our results suggest that the presence of a system of active, sub-parallel faults within the network may be consistent with large scale mechanical coupling between the San Andreas and other associated faults at depth. This is consistent, for example, with seismic images obtained in the San Francisco Bay Area which suggest the presence of a large-scale detachment at mid-crustal levels (*Brocher et al.*, 1994). Such a detachment may serve to effectively transmit stresses at depth between the faults within the San Andreas system, rather than through the primarily elastic upper crust alone (*Brocher et al.*, 1994).

Constraints on lower crustal rheology are difficult to obtain from the idealized model presented here but, it is interesting to note that in the San Francisco Bay area models of post-seismic relaxation are consistent with relatively short lower crustal relaxation times (on the order of 10^{1-2} years) and therefore small lower crustal viscosities (e.g., *Linker and Rice*, 1997; *Rundle and Jackson*, 1977). These findings are consistent with predictions of our model, which suggests that large-scale motion must occur in the lower crust to facilitate interaction between widely separated faults within the deformation zone.

CONCLUSIONS

The results presented here suggest that the nature of deformation at a strike-slip plate boundary is strongly controlled by the rheology of the lower crust. For example, in the presence of a (weak) low viscosity lower crustal layer the width of the zone of deformation within the upper crust broadens significantly over the history of the plate margin. Brittle failure occurs on a system of widely spaced faults which interact to form networks with complicated surface strain rate patterns and failure histories (recurrence intervals). Faulting-related strain rate perturbations are localized in both space and time around each failure event, and therefore lead to complex strain rates during the evolution of the fault system. The fault planes correspond to regions of strain localization within

the upper crust, which extend into inclined, sub-horizontal zones of high shear in the lower crust. Maximum shear stresses are confined to shallow to mid-crustal levels because of viscous flow within the lower crust, which therefore confines brittle failure to the upper "seismogenic" part of the crust. In contrast, when the lower crust behaves primarily elastically, deformation in the upper crust is confined to a narrow region around the plate margin. Brittle failure occurs primarily on the single, plate bounding fault, which extends from the surface to the Moho. Surface patterns of strain rates in this case are simple, with maximum strain rates at the plate margin, decreasing monotonically away from it.

APPENDIX

Continuous deformation. Equations 5.2a and 5.2b, the constitutive relations for a Maxwell solid, are differentiated with respect to x and z, respectively, and combined with the equation of motion (5.1) to obtain an equation for velocity within the crust (equation 5.3). Equation (5.3) is resolved into a system of two coupled equations,

$$w(x,z,t) = \left(\frac{\partial^2 v}{\partial x^2} + \frac{\partial^2 v}{\partial z^2} \right) \tag{5.A1}$$

and

$$\tau(z) \frac{\partial w(x,z,t)}{\partial t} = \frac{1}{\alpha} \frac{\partial v}{\partial z} - w(x,z,t) \tag{5.A2}$$

which are solved using finite difference techniques, subject to the boundary and initial conditions:

$$\left. \frac{\partial v}{\partial z} \right|_{z=0} = 0 \quad \text{(shear stress free surface at } z = 0) \tag{5.A3a}$$

$$v(x = L,z,t) = V_0 \quad \text{(match plate velocity at edges, } x = \pm \text{L)} \tag{5.A3b}$$

$$v = \pm V_0 \text{ at } z = H \text{ (match velocity at Moho)} \tag{5.A3c}$$

$$\sigma_{yx}(x,z,0) = \sigma_{yz}(x,z,0) = u(x,z,0) = 0 \text{ (zero initial stresses and displacements).} \tag{5.A3d}$$

Elastic dislocations. The analytic expressions for the stresses and displacements within an elastic half-space due to a finite dislocation are derived by *Chinnery*, (1961). Since we ignore deformation in the mantle, we use these expressions with the important restriction that the displacements at the Moho due to faulting should be negligible compared with displacements due to tectonic loading over one earthquake cycle. For our range of model parameters, this restricts the depth-extent of dislocations to <10 km (at ≈10 km depth of faulting, the Moho displacements due to faulting are less than 1-2% of the displacements due to tectonic loads). The analytic form for the displacements, u^{dis}, and shear stress on

planes parallel to the fault, σ_{yx}^{dis}, are (modified from *Chinnery*, 1961, for an infinitely long fault),

$$u^{dis}(x',z)=\frac{U}{2\pi}\left\{\tan^{-1}\left(\frac{x'}{d-z}\right)+\tan^{-1}\left(\frac{x'}{d+z}\right)+\tan^{-1}\left(\frac{x'}{D-z}\right)+\tan^{-1}\left(\frac{x'}{D+z}\right)\right\} \quad (5.A4)$$

and

$$\sigma_{yx}^{dis}(x',z)=\frac{\mu U}{2\pi}\left\{\left(\frac{d-z}{(d-z)^2+x'^2}\right)+\left(\frac{d+z}{(d+z)^2+x'^2}\right)-\left(\frac{D-z}{(D-z)^2+x'^2}\right)-\left(\frac{D+z}{(D+z)^2+x'^2}\right)\right\}, \quad (5.A5)$$

where $x'=x-x^{dis}$, x^{dis} is the location of the dislocation, z is depth below the surface, d and D are the burial depth and maximum depth of the fault, respectively, U is the slip on the fault, and μ is the shear modulus.

Table 5.1. Parameters used in figures[a]

Figure 5.2	Cohesion for fracture and faulting: 50 MPa and 1 MPa, respectively; ρ=2800 kg/m^3, coefficient of friction=0.6, g=9.8 m/s^2.
Figure 5.3	α=15 km for high viscosity crust and α=3 km for a low viscosity lower crust
Figure 5.4	L=360 km, σ_{frac}=50 MPa + 0.6σ_n, σ_{fric}=1 MPa + 0.6σ_n, (a) α=15 km, (b) α=3 km, (i) t=528 years, (ii) t=5813 years, (iii) t=8456 years, and (iv) t=10570 years.
Figure 5.5	L=360 km, σ_{frac}=50 MPa + 0.6σ_n, σ_{fric}=1 MPa + 0.6σ_n, (a) α=15 km, (b) α=3 km. In (c) all parameters as in (b), but: σ_{fric}=48 MPa + 0.6σ_n.
Figure 5.6	L=360 km, σ_{frac}=50 MPa + 0.6σ_n, σ_{fric}=1 MPa + 0.6σ_n, (a) α=15 km, (b) α=3 km.
Figure 5.7	L=360 km, σ_{frac}=50 MPa + 0.6σ_n, σ_{fric}=1 MPa + 0.6σ_n, t=1.06×10^4 years, (a) α=15 km, (b) α=3 km.
Figure 5.8	L=360 km, σ_{frac}=50 MPa + 0.6σ_n, σ_{fric}=1 MPa + 0.6σ_n, t=1.06×10^4 years, (a) α=15 km, (b) α=3 km.
Figure 5.9	L=360 km, σ_{frac}=50 MPa + 0.6σ_n, σ_{fric}=1 MPa + 0.6σ_n, α=3 km.
Figure 5.10	L=360 km, σ_{frac}=50 MPa + 0.6σ_n, σ_{fric}=1 MPa + 0.6σ_n, α=3 km.
Figure 5.11	L=360 km, σ_{frac}=50 MPa + 0.6σ_n, σ_{fric}=1 MPa + 0.6σ_n, α=3 km.
Figure 5.12	L=360 km, σ_{frac}=50 MPa + 0.6σ_n, σ_{fric}=1 MPa + 0.6σ_n, α=3 km, t=7.399×10^4 years.

[a] In all calculations: μ=30 GPa, V_0=35 mm/yr (relative slip rate of 70 mm/yr), η_0=10^{23} Pa s, dx=dz=4 km and H=28 km.

REFERENCES

Block L. and L. H. Royden, Core complex geometries and regional scale flow in the lower crust, *Tectonics*, *9*, no. 4, 557-567, 1990.

Brocher, T. M., J. McCarthy, P.E. Hart, S.W. Holbrook, K.P. Furlong, T.V. McEvilly, J.A. Hole, and S.L. Klemperer, Seismic evidence for a lower-crustal detachment beneath the San Francisco Bay, California, *Science*, *265*, 1436-1439, 1994.

Chinnery, M. A., The deformation of the ground around surface faults, *Bull. Seism. Soc. Am.*, 51, 355-372, 1961.

Cohen, S. C., Postseismic viscoelastic surface deformation and stress 1. Theoretical considerations, displacement and strain calculations, *J. Geophys. Res.*, *85*, 3131-3150, 1980.

Donnellan, A., B. H. Hager and R. W. King, Discrepancy between geological and geodetic deformations rates in the Ventura basin, *Nature*, *366*, 333-336, 1993.

Hill, D. P., J. P. Eaton and L. M. Jones, Seismicity, 1980-86, in The San Andreas fault system, California, *U.S. Geol. Surv. Prof. Paper*, *1515*, 115-151, 1990.

Humphreys, E.D. and B.H. Hager, A kinematic model for the late Cenozoic development of southern California crust and upper mantle, *J. Geophys. Res.*, *95*, 19747-19762, 1990.

Li, V. C. and J. R. Rice, Crustal deformation in great California earthquake cycles, *J. Geophys. Res.*, *92*, 11,533-11,551, 1987.

Linker, M. and J. R. Rice, Models of post-seismic deformation and stress transfer associated with the 1989 Loma Prieta earthquake, *in press*, 1997.

Lyzenga, G. A., A. Raefsky and S. G. Mulligan, Models of recurrent strike-slip earthquake cycles and the state of crustal stress, *J . Geophys. Res.*, *96*, 21,623-21,640, 1991.

Royden, L. H., Coupling and decoupling of crust and mantle in convergent orogens: Implications or strain partitioning in the crust ,*J . Geophys. Res.*, *101*, 17,679-17,705, 1996.

Rundle, J.B. and D.D. Jackson, A kinematic viscoelastic model of the San Francisco earthquake of 1906, *Geophys. J. R. astr. Soc.*, *50*, 441-458, 1977.

Segall, P. and D. D. Pollard, Mechanics of discontinuous faults, *J. Geophys. Res.*, 85, 4337-4350, 1980.

Weldon, R.J., and Humphreys, E.D., A kinematic model of southern California, *Tectonics*, *5*, 33-48, 1986.

FIGURE CAPTIONS

Figure 5.1. (a) Schematic diagram of (i) the viscosity structure and (ii) elastic properties used to specify continuum crustal rheology in our model. The maximum viscosity is at the surface, η_0, and decreases exponentially as a function of depth to a minimum value at the Moho, $z=H=28$ km. The shear modulus is assumed constant throughout the crust, $\mu=30$ GPa. (b) Geometry of the dextral strike-slip plate boundary, with imposed mantle and far-field plate velocities indicated by the small arrows. The plane of the main, plate-bounding fault is the y-z plane and L is taken to be $>>H$. (c) The only non-zero shear stresses act on vertical planes parallel to the plate boundary (σ_{yx}) and on horizontal planes (σ_{yz}).

Figure 5.2. Brittle failure threshold as a function of depth. Failure on a pre-existing fault plane is determined by $\sigma_{fric}=1$ MPa$+0.6\sigma_n$ (σ_n=overburden pressure$=\rho gz$) and fracture of a new fault plane is determined by $\sigma_{frac}=50$ MPa$+0.6\sigma_n$. During any failure even the post-failure shear stress on the fault plane, σ_{fail}, is assumed to be 1/3 of σ_{fric} at that depth (dashed line).

Figure 5.3. Relaxation time vs. depth in the two cases studied: a high viscosity crust and a low viscosity lower crust. For a high viscosity crust, $\alpha=15$ km so that the relaxation time at the Moho ($z=28$ km) is within the same order of magnitude as that at the surface ($\tau_0=10^5$ years). For a low viscosity lower crust, $\alpha=3$ km so that the relaxation time at the Moho is almost four orders of magnitude smaller than that at the surface.

Figure 5.4. (a) Displacement as a function of depth and position (for $x>0$) in a high viscosity crust, at various times during the deformation history (t increases from (i) to (iv); see Table 5.1). The main fault plane ($x=0$) is characterized by a sharp slip discontinuity, with most of the deformation concentrated on this plane. (b) (i)-(iv) Displacement as a function of depth and position in the presence of a low

viscosity lower crust, at various times (Table 5.1). The zone of deformation is narrow at deep crustal levels at all times but broadens with time in the upper crust to encompass a region of width ≈60 km. Slip discontinuities (which appear as kinks in the mesh at near surface regions) develop in the upper crust at faults laterally displaced from the strike-slip plate boundary, with a maximum depth of brittle failure ≤10 km.

Figure 5.5. Growth of the brittle failure region over t=0 to 10000 years for (a) a high viscosity crust and (b) a low viscosity lower crust. Failure initiates at near surface regions of the plate boundary (x=0) in panel (i) of (a) and (b), but deepens with time (panel ii). In (a) brittle failure in a high viscosity crust is primarily focused along the plane of the plate boundary and extends from the surface to the Moho. In (b) however, the failure region does not extend beyond 10 km depth at the plate margin, but widens significantly to positions laterally away from the plate boundary. The maximum depth of faulting decreases with distance from the main plate-bounding fault and the characteristic spacing or faults is 12 km. In (c) the failure region for a crust with comparable fracture and failure criteria is shown. In this case, the spacing of fault planes is much smaller (4 km =dx).

Figure 5.6. Contour plot of surface strain rates (s^{-1}) as a function of time and distance from the main fault plane in (a) a high viscosity crust and (b) in the presence of a low viscosity lower crust. The simulation was carried out to 10^4 years, ≈1/10th of the relaxation time at the surface. Surface strain rates in (a) are maximum on the main fault plane (x=0) and decay with distance away from the fault. Initially surface strain rates in (b) are maximum on the main fault plane (x=0) and decay with distance away from the plate boundary, as in a high viscosity crust (a). However, strain rates become significantly more complicated in time with persistent maxima centered in time and space over secondary faulting events away

from the main fault plane. (Note that the high frequency variations in strain rates are due to failures. Contour interval is 10^{-15} s^{-1}.)

Figure 5.7. Orientation of predicted failure planes within the crust at t=1.06×10^4 years (a) in an approximately uniform viscosity crust with α=15 km and (b) in the presence of a low viscosity lower crust. These orientations are obtained by combining the brittle failure criteria with the local orientations of the principal stress axes at each node in the model. In (a) the optimal (dextral) failure planes are nearly vertical throughout the crust. In (b) although the failure planes are oriented vertically near the surface, local rotations of the principal stress axes induced by viscous flow in the lower crust cause them to rotate into sub-horizontal orientations at depth.

Figure 5.8. Shear stress on vertical planes, σ_{yx}, at t=1.06×10^4 years for (a) a high viscosity crust and (b) in the presence of a low viscosity lower crust. In (a) the largest stresses are in the lowermost crust at the plate boundary, although a small secondary maximum at about 5 km depth is formed due to near-surface faulting away from the plate margin. At the surface, both the main fault plane and the secondary maxima are characterized by local shear stress minima. In (b), the stress maximum on the plate bounding fault is at ≈10 km depth, with development of significant off-axis maxima due to fracture of new faults.

Figure 5.9. Long-term evolution of σ_{yx} in the presence of a low viscosity lower crust, showing the development of widening zone of parallel faults at (a) t≈4×10^4 years and (b) t≈7×10^4 years. Compare with Figure 5.8b which shows the shear stresses at t≈1.06×10^4 years.

Figure 5.10. Long-term evolution of surface strain rates in the presence of a low viscosity lower crust. Each panel shows a gray-shaded contour plot of surface

strain rates (contour intervals as in Figure 5.6), on which we superpose the locations and times of failure at various depths within the crust: 2 km (circles), 6 km (triangles), and 10 km (squares). Symbol sizes are proportional to the amount of slip in each event (1 inch=10 m). Note that events with very small slip near the surface are open circles which are too small to resolve and thus appear as dots. Fracture at a particular depth is distinguished from failure on a pre-existing fault plane by plotting several symbols of decreasing size on top of each other. Compound failure events, which involve simultaneous slip at various depths appear as overlapping circles, triangles and/or squares, e.g. at x=0 km and t≈4000 years.

Figure 5.11. Failure histories on (a) the main plate-bounding fault (x=0 km) in a high viscosity crust and (b) the plate bounding fault (i) and two secondary faults (ii and iii) in the presence of a low viscosity lower crust. The minimum recurrence interval is dt=10 years in all cases.

Figure 5.12. Horizontal shear strain ($\partial u/\partial x$) in the presence of a weak lower crust, at $t\approx 7\times 10^4$ years. The dark shading indicates high strain areas, which are seen to extend vertically downwards from the surface and bend in towards the plate boundary (x=0) at depth.

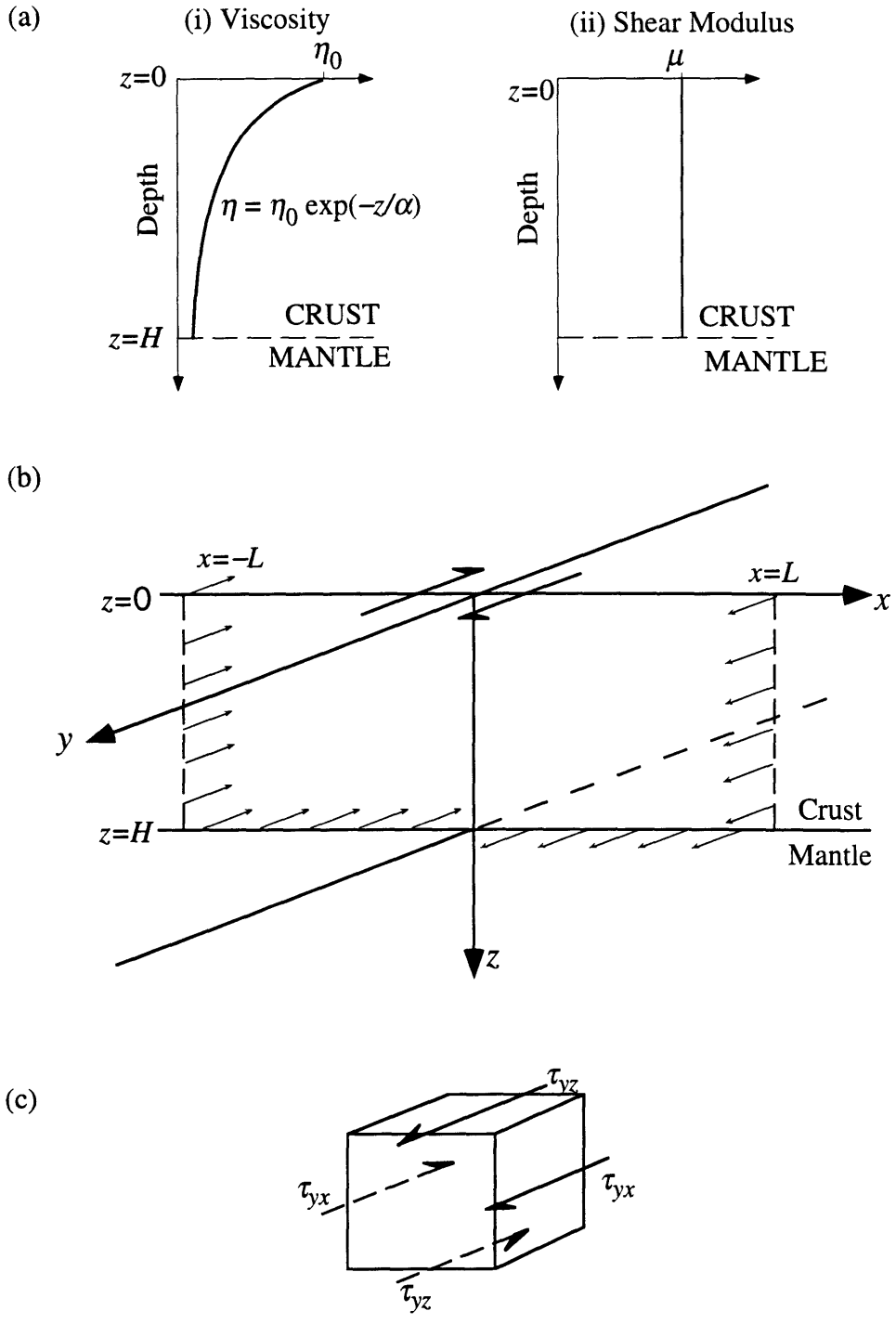
(a)
(i) Viscosity
η_0
z=0
Depth
$\eta = \eta_0 \exp(-z/\alpha)$
z=H
CRUST
MANTLE
(ii) Shear Modulus
μ
z=0
Depth
CRUST
MANTLE
(b)
x=−L
x=L
z=0
x
y
z=H
Crust
Mantle
z
(c)
τ_{yz}
τ_{yx}
τ_{yx}
τ_{yz}

Figure 5.1

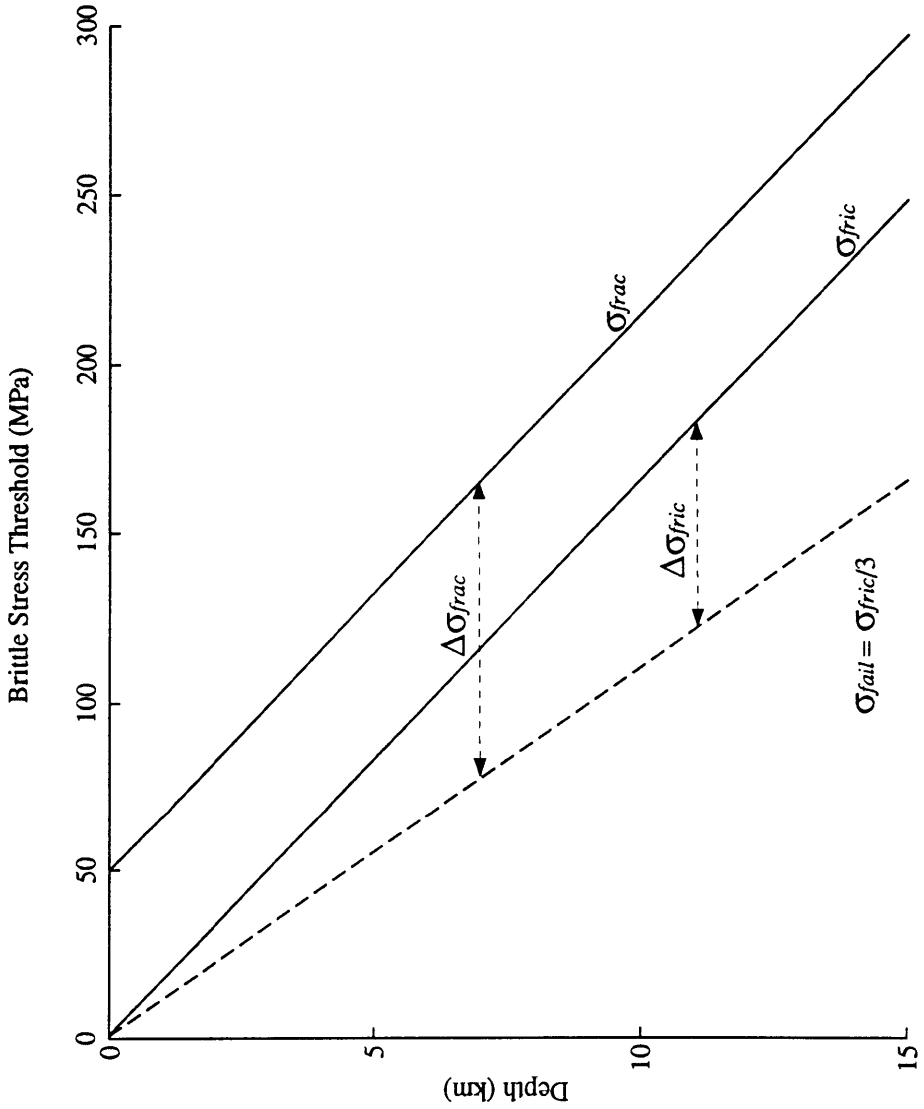
Brittle Stress Threshold (MPa)
0
50
100
150
200
250
300
Depth (km)
0
5
10
15
σfrac
σfric
Δσfrac
Δσfric
σfail = σfric/3

Figure 5.2

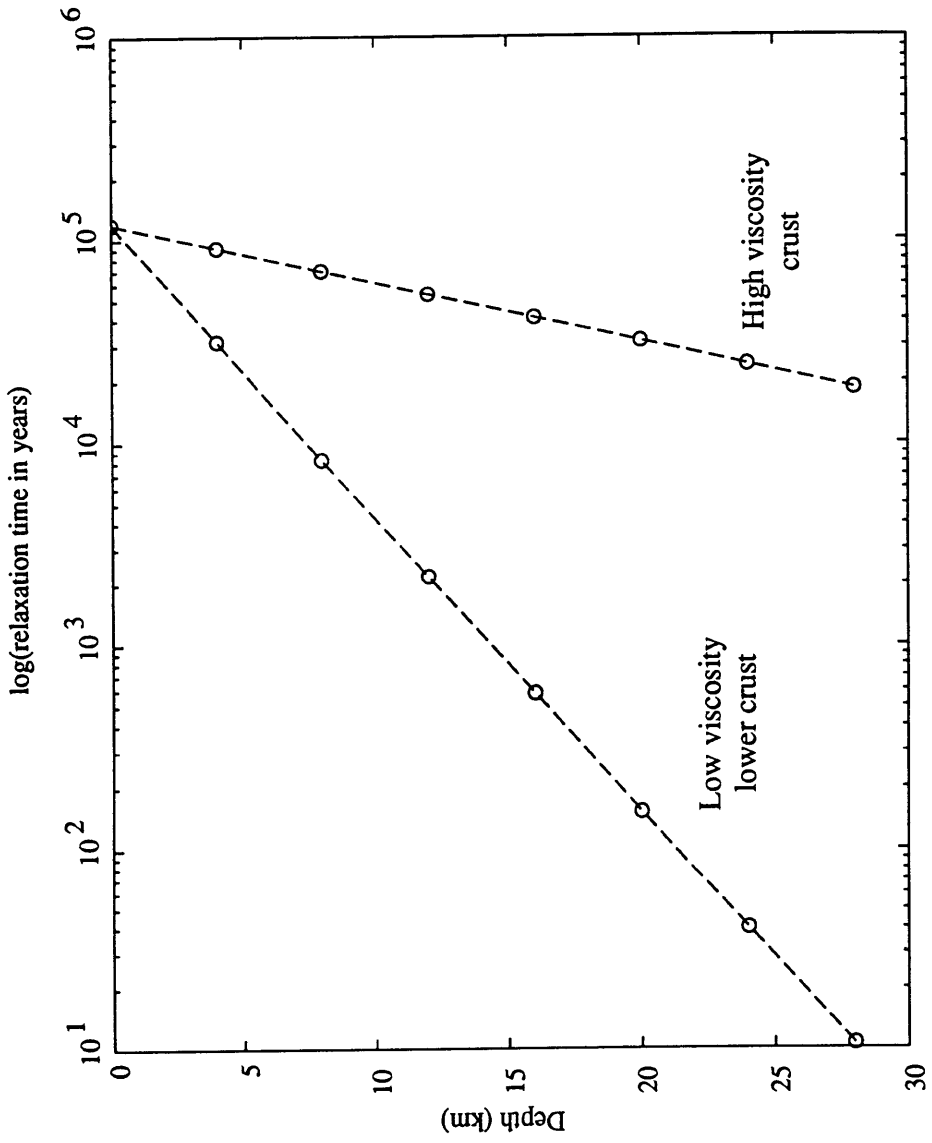
log(relaxation time in years)
10^1
10^2
10^3
10^4
10^5
10^6
0
5
10
15
20
25
30
Depth (km)
High viscosity
crust
Low viscosity
lower crust

Figure 5.3

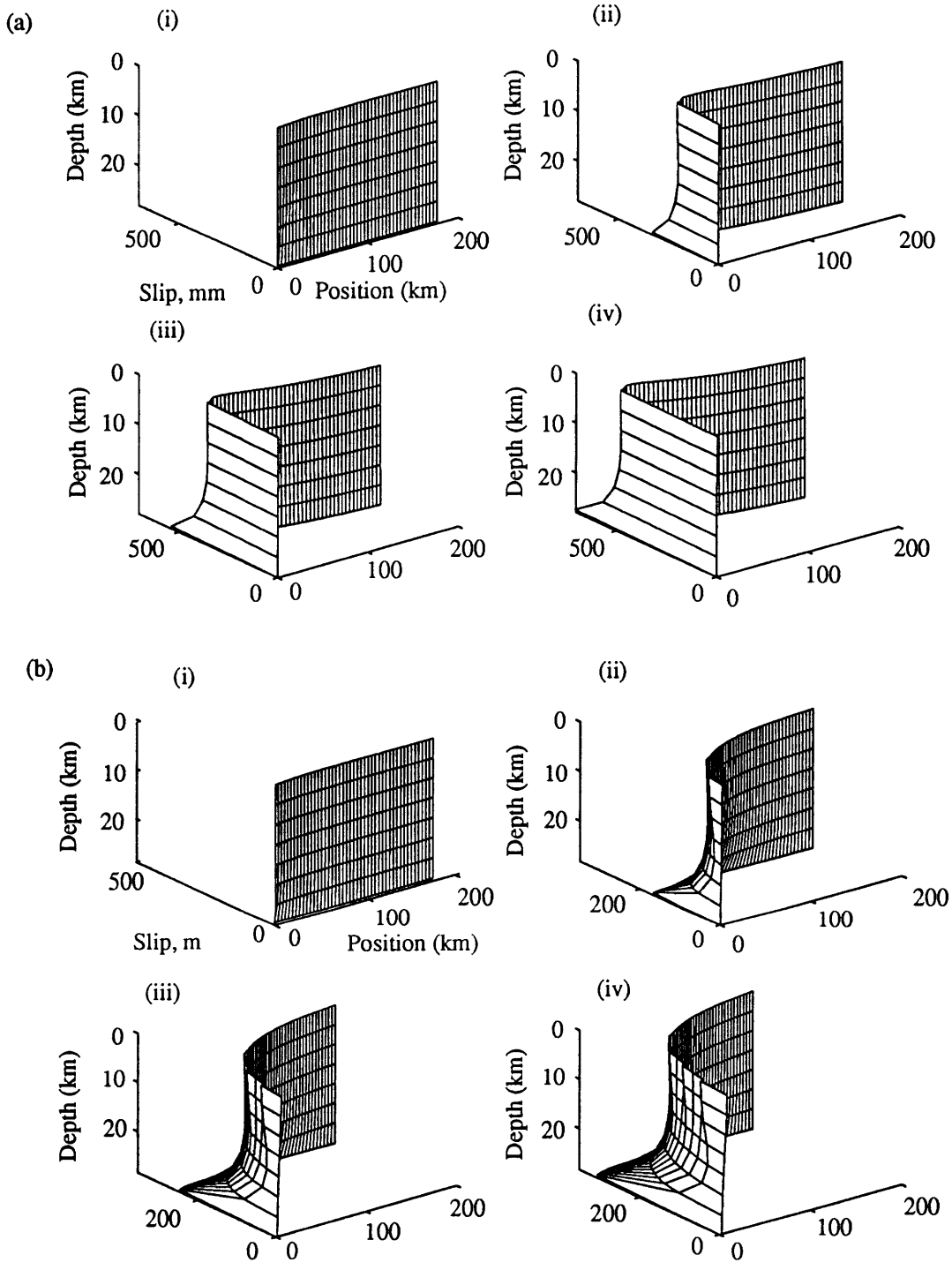
(a)
(i)
(ii)
(iii)
(iv)
Depth (km)
0
10
20
500
0
Slip, mm
0
100
200
Position (km)
(b)
(i)
(ii)
(iii)
(iv)
Depth (km)
Slip, m
Position (km)

Figure 5.4

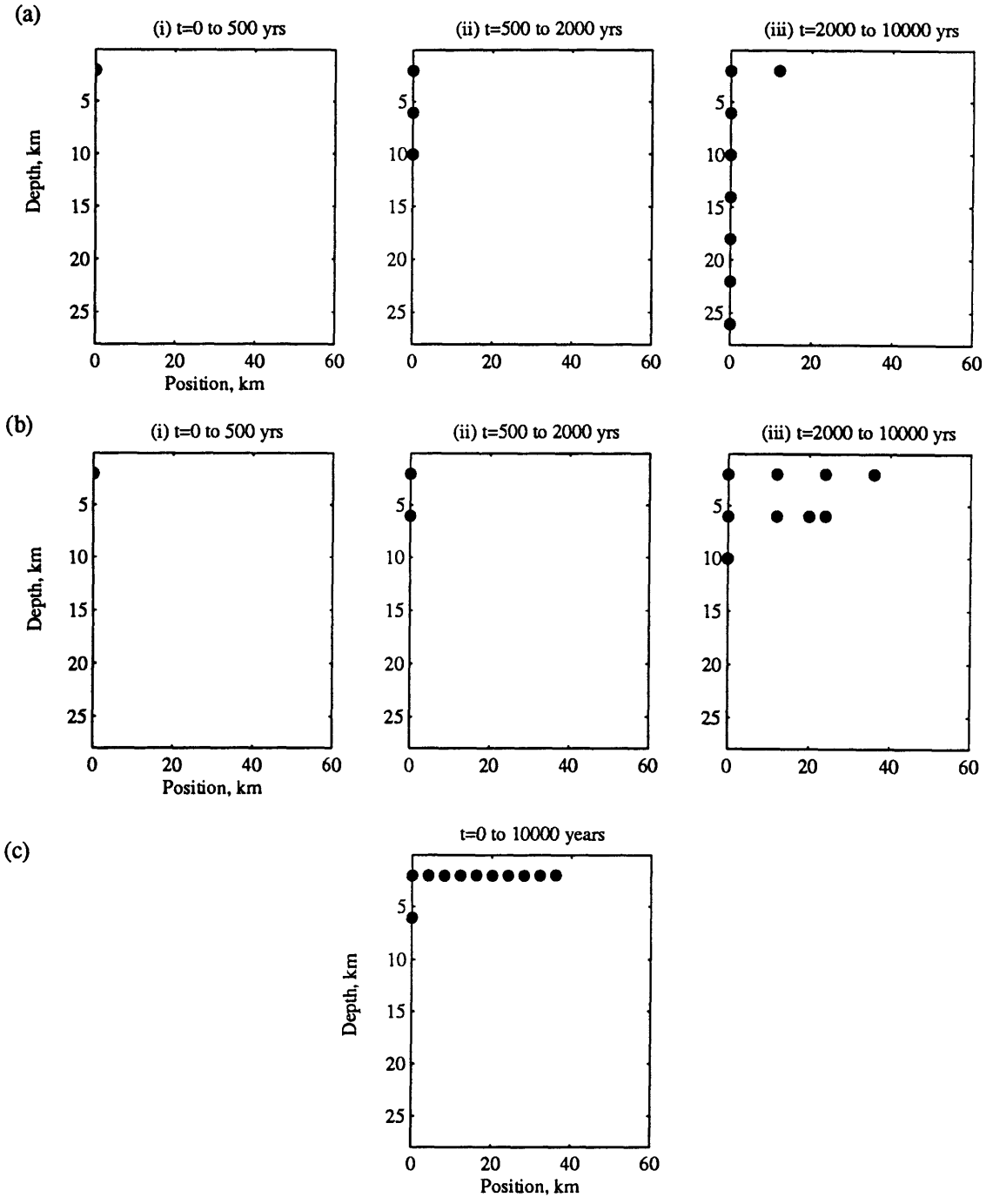
(a)
(i) t=0 to 500 yrs
(ii) t=500 to 2000 yrs
(iii) t=2000 to 10000 yrs
Depth, km
Position, km
(b)
(i) t=0 to 500 yrs
(ii) t=500 to 2000 yrs
(iii) t=2000 to 10000 yrs
Depth, km
Position, km
(c)
t=0 to 10000 years
Depth, km
Position, km

Figure 5.5

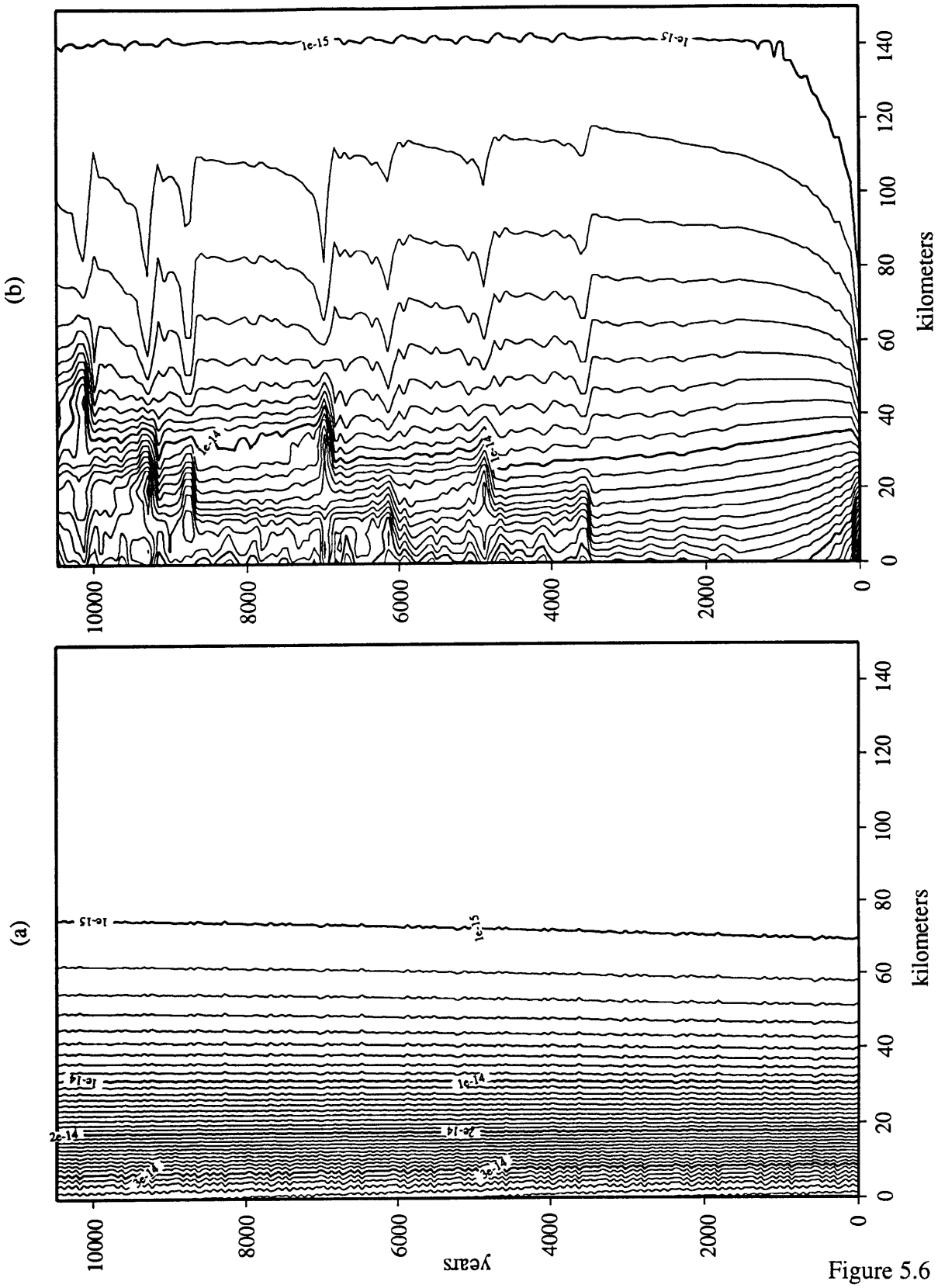
(a)
(b)
years
kilometers
kilometers
0
2000
4000
6000
8000
10000
0
20
40
60
80
100
120
140
1e-15
1e-14
2e-14

Figure 5.6

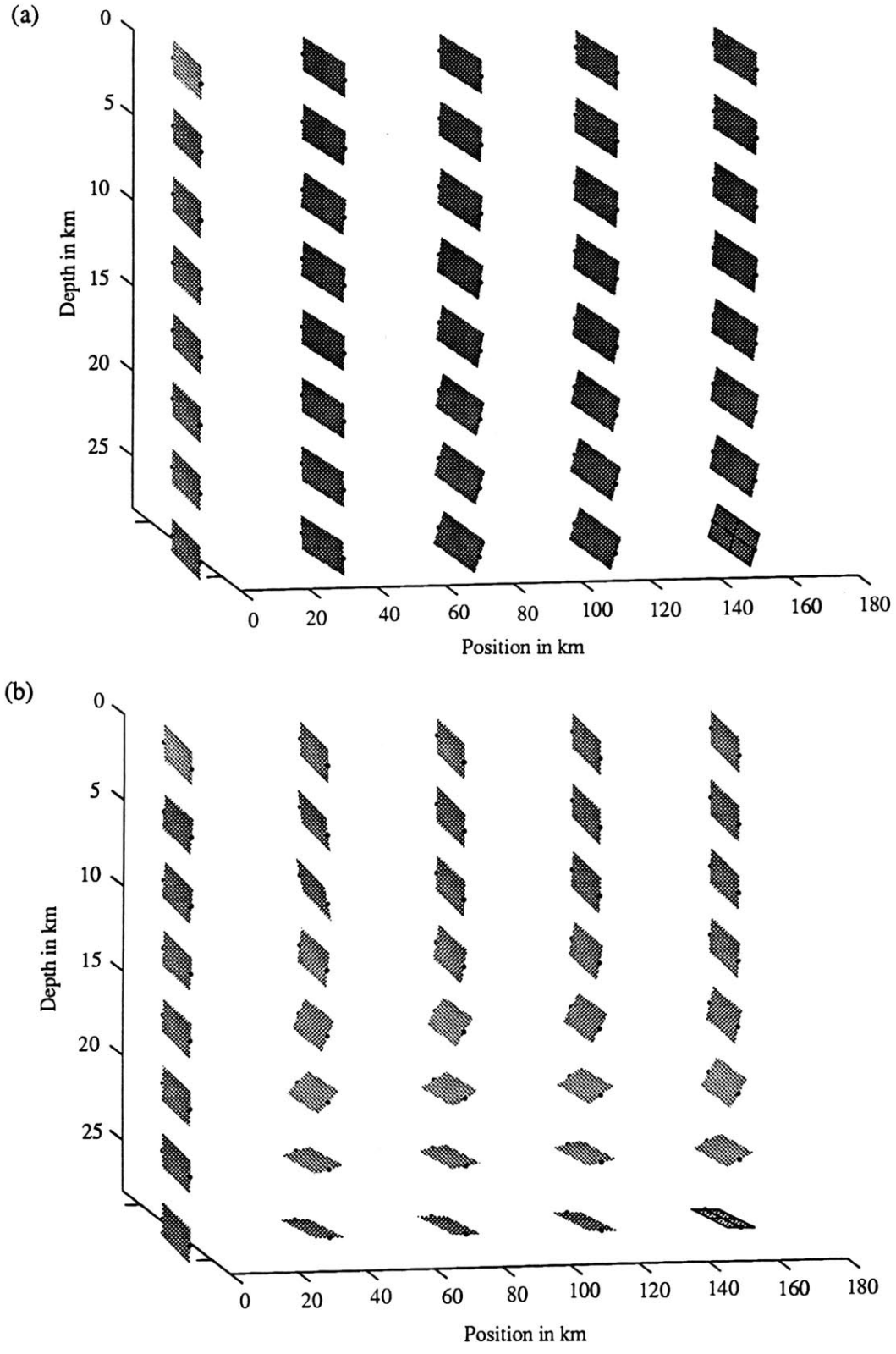
(a)
Depth in km
0
5
10
15
20
25
0
20
40
60
80
100
120
140
160
180
Position in km
(b)
Depth in km
0
5
10
15
20
25
0
20
40
60
80
100
120
140
160
180
Position in km

Figure 5.7

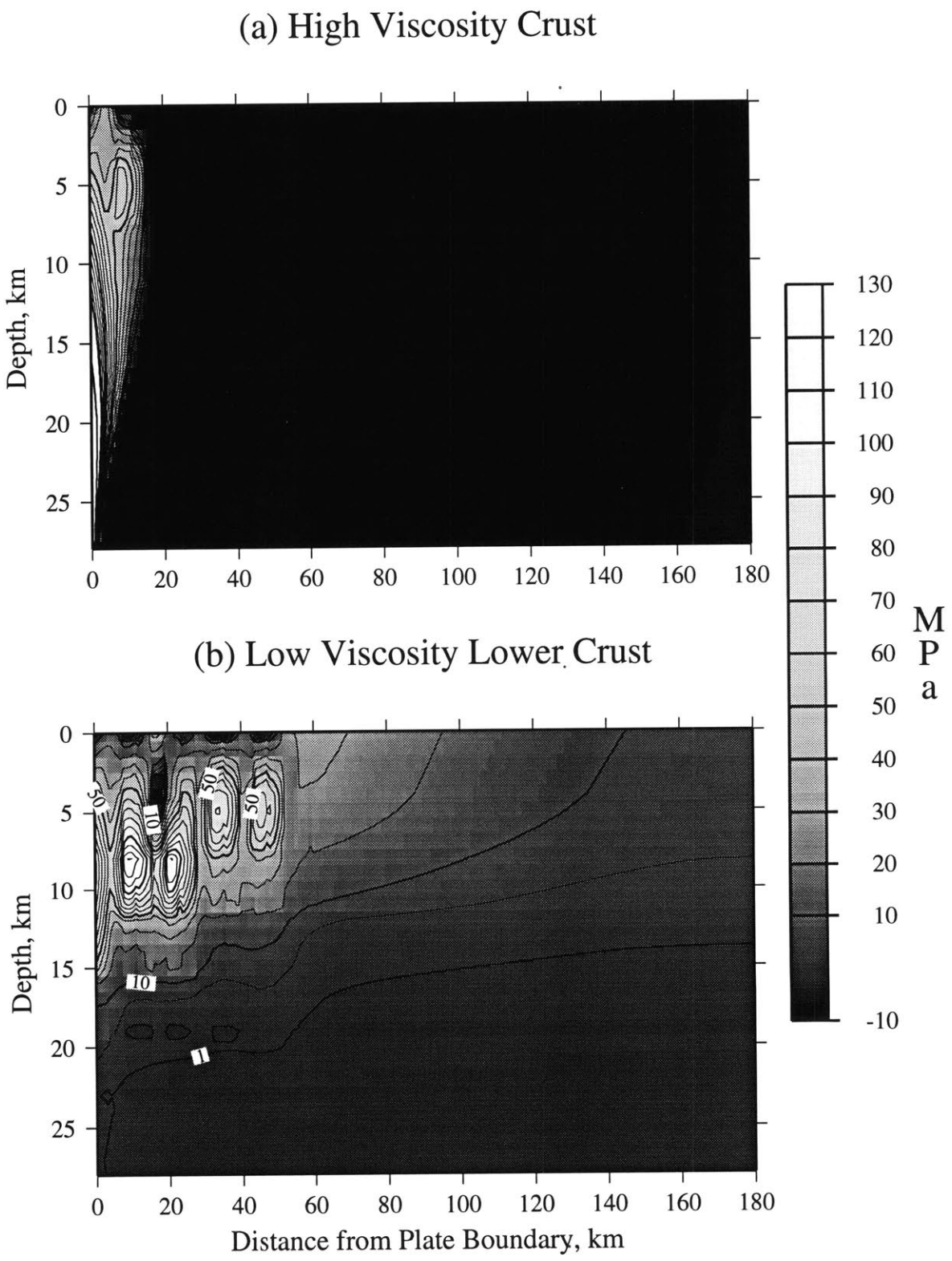
(a) High Viscosity Crust
Depth, km
0
5
10
15
20
25
0
20
40
60
80
100
120
140
160
180
130
120
110
100
90
80
70
60
50
40
30
20
10
-10
MPa
(b) Low Viscosity Lower Crust
Depth, km
50
10
50
50
10
1
Distance from Plate Boundary, km

Figure 5.8

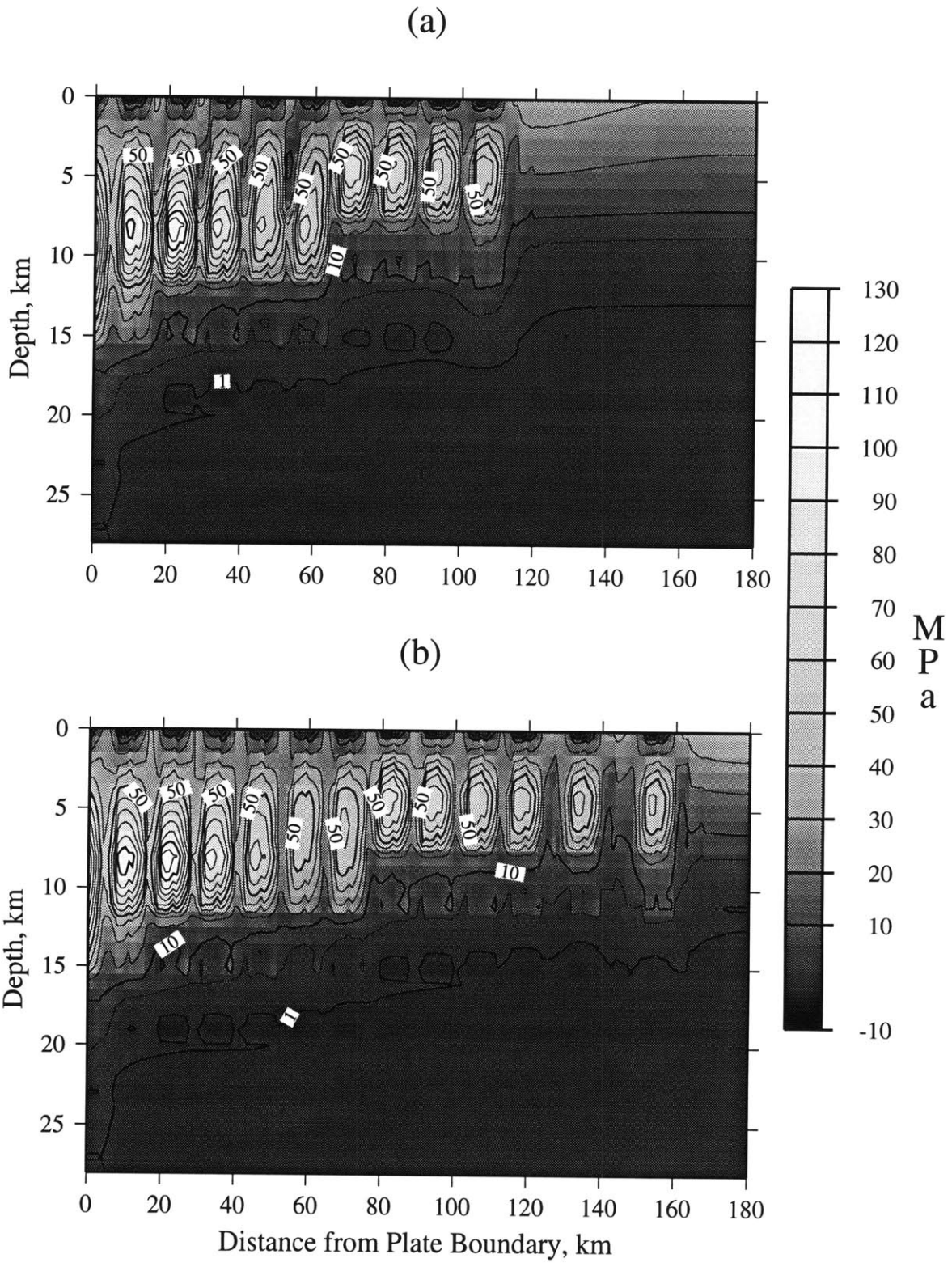
(a)
(b)
Depth, km
Distance from Plate Boundary, km
0
5
10
15
20
25
0
20
40
60
80
100
120
140
160
180
50
10
1
130
120
110
100
90
80
70
60
50
40
30
20
10
-10
MPa

Figure 5.9

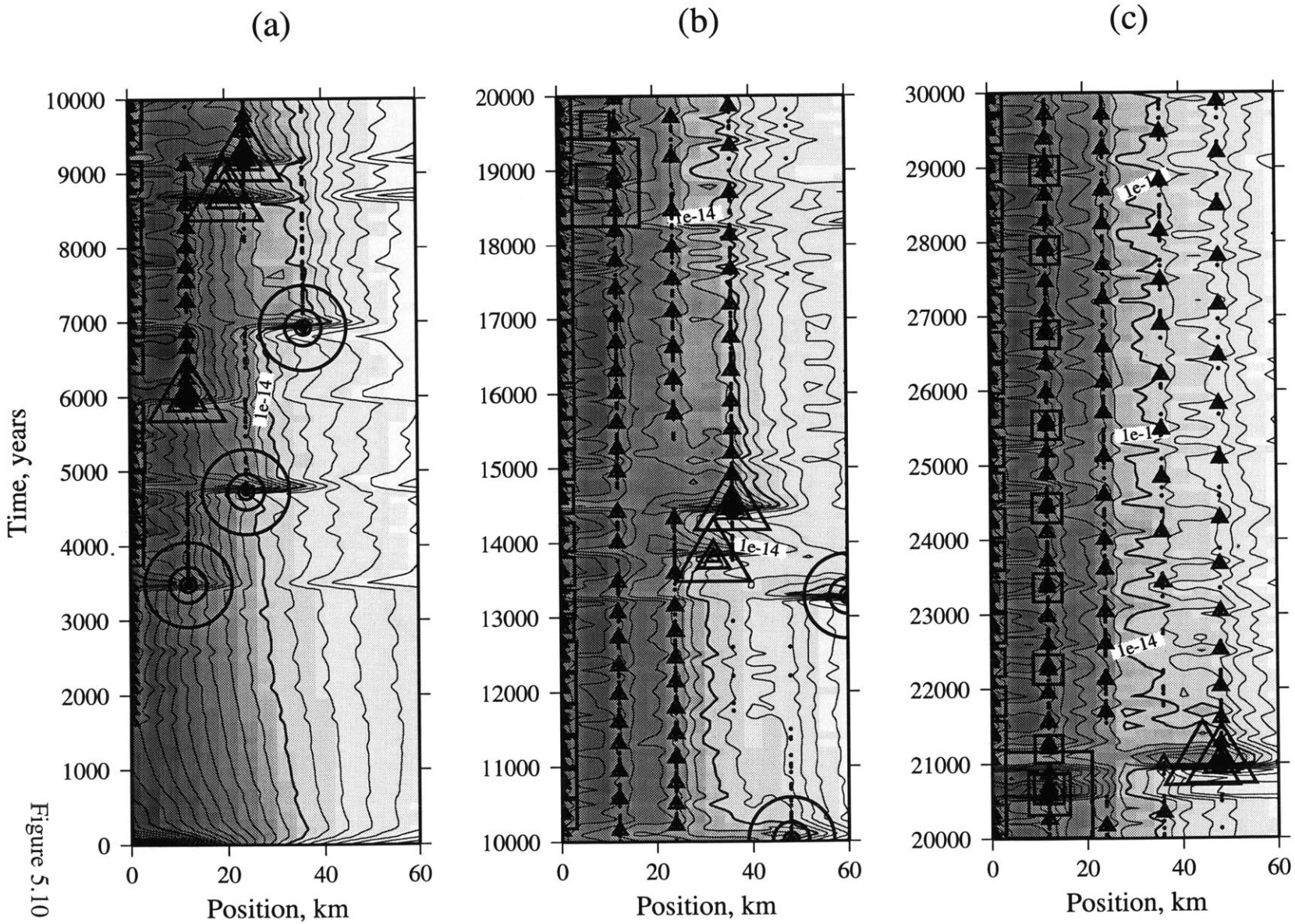
(a)
(b)
(c)
Time, years
Position, km
Position, km
Position, km
1e-14
1e-14
1e-14
1e-14

Figure 5.10

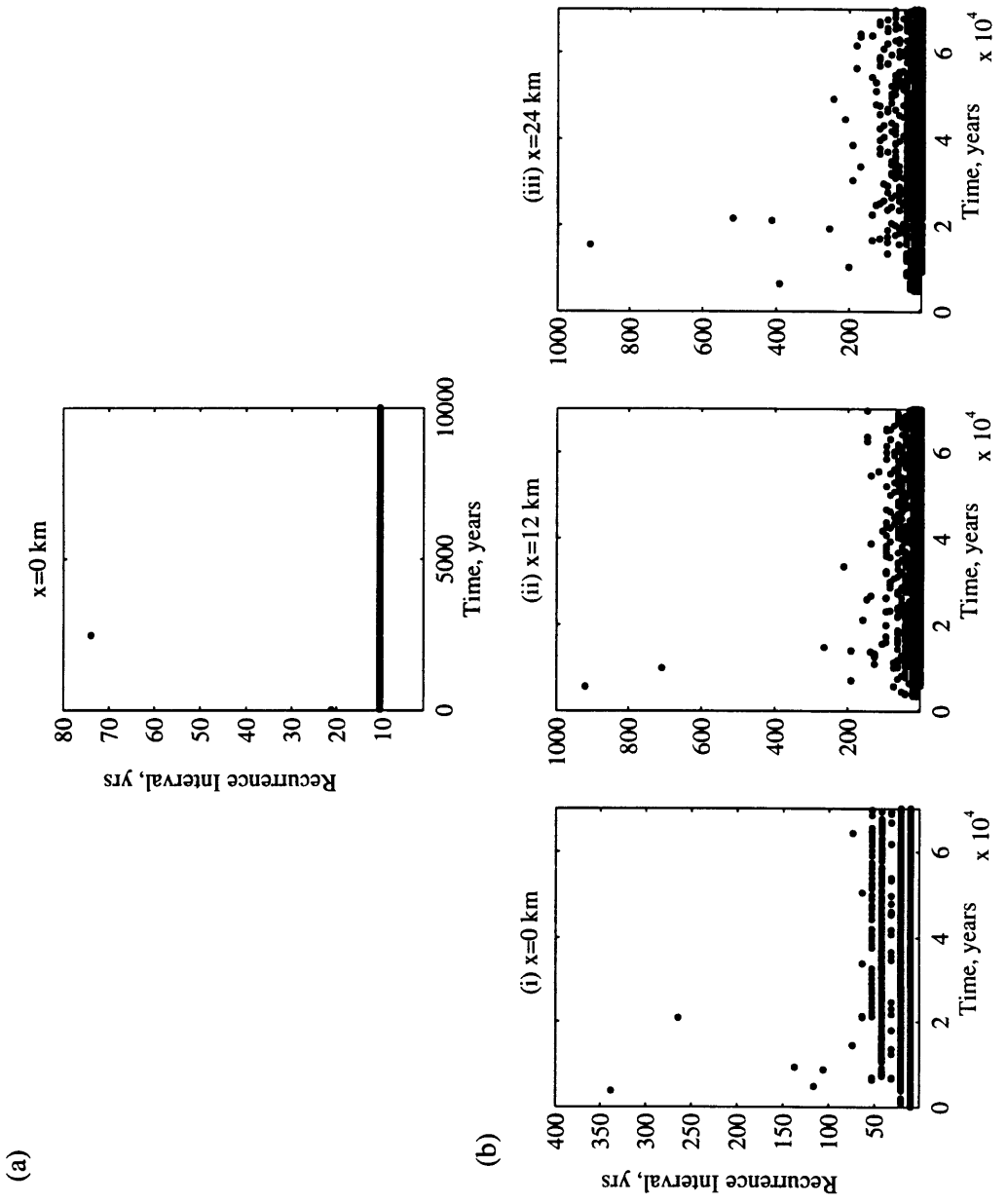
(a)
x=0 km
Recurrence Interval, yrs
Time, years
(b)
(i) x=0 km
(ii) x=12 km
(iii) x=24 km
Recurrence Interval, yrs
Time, years
x 10^4

Figure 5.11

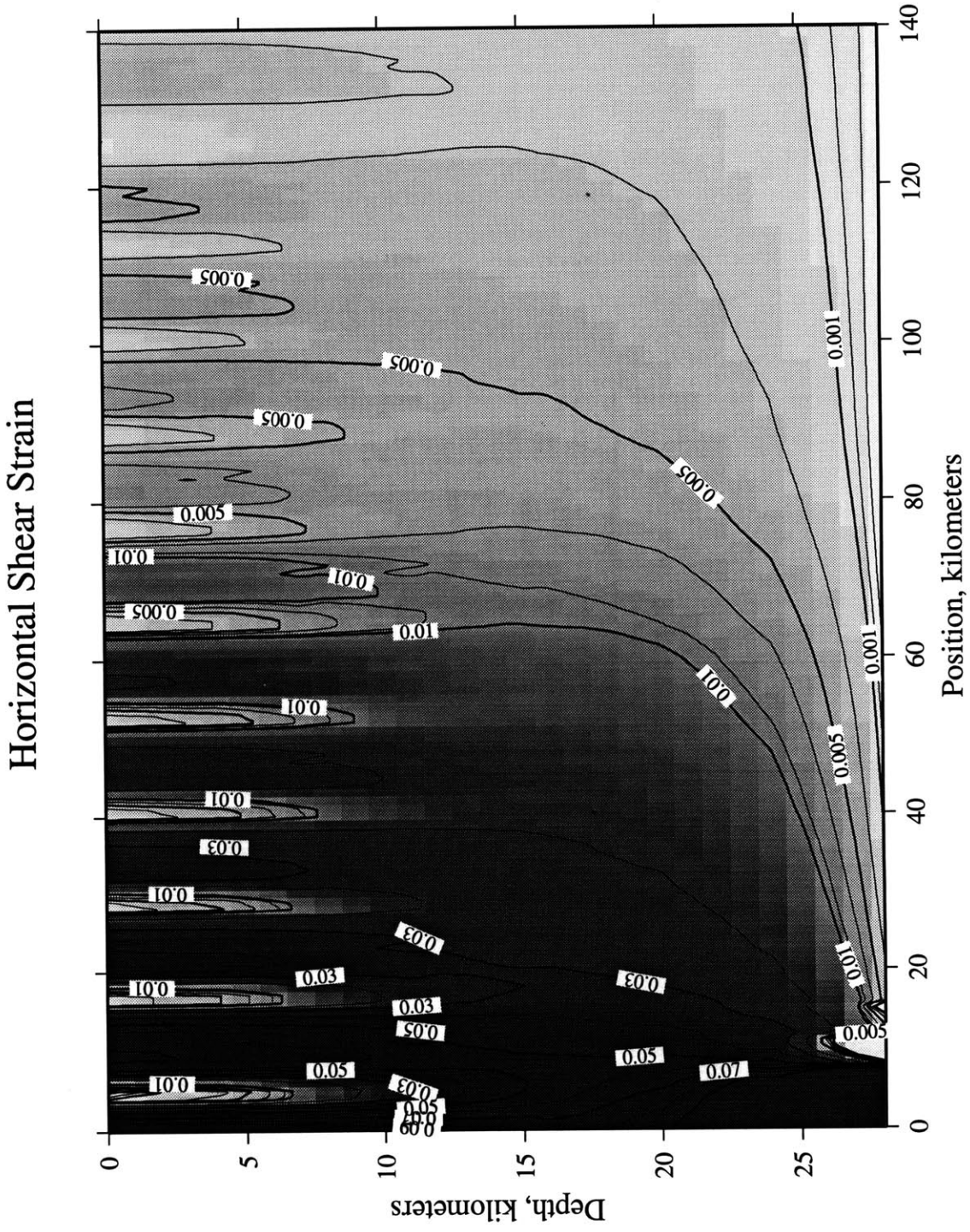

6243 - 50

Figure 5.12